

Ludwig-Maximilians-Universität
Fakultät für Physik



Master Thesis

Development of a Position Sensitive Scintillating
Muon Detector with Silicon Photo-Multiplier
Readout

Entwicklung eines szintillierenden Myon Detektors
mit SiPM-Auslese zur Positionsbestimmung
kosmischer Myonen

submitted by: submitted on: Supervisor:
Ralph Müller (#8068305) 27. September 2013 Prof. Dr. Otmar Biebel

Betreuer: Dr. Ralf Hertenberger

Gutachter: Prof. Dr. Otmar Biebel

Abstract

The Cosmic Ray Facility in Garching (CRF) is used to calibrate large area tracking detectors with cosmic muons. Currently large area Micromegas detectors, foreseen for the New Small Wheel upgrade of the ATLAS muon spectrometer, are investigated at the CRF.

To enhance the performance of the CRF, the energy selector will be improved. In this thesis a scintillating plastic detector with light detection via Silicon Photo-Multiplieres (SiPMs) is investigated for providing a two dimensional spatial resolution with trigger capability.

The detector is modularized and each module consists of two optically separated trapezoids. Scintillation light, created by cosmic muons, is collected by wavelength shifting fibers (WLSFs) and guided to SiPMs. The position resolution in one direction is achieved by measuring the propagation time of light from the point of creation to the SiPM. For the second coordinate one compares the light yield of the two detector halves of one module. The light yield is proportional to the path length of the muon and therefore correlated to the point where the muon passes the trapezoid.

A prototype detector is tested in a beam time at CERN. The results of the prototype, which prove the basic concept of the detector, are presented in this thesis. To further enhance the light yield, new light reflecting materials for an optical separation of trapezoids are tested experimentally. Furthermore a self developed simulation for studying geometries and fiber position is presented.

The total light yield is enhanced by a factor of two in measurement and simulation, by using diffuse reflective cover material. Moreover the simulation shows, that a smaller trapezoidal structure, compared to the first prototype, indicates promising position resolving properties, which have to be further investigated in future. Investigating simulations with new fiber positions reveals, that the position resolution of the first prototype can be improved by fibers at the edge of the scintillator rod.

The presented results of the experiments and simulations will be part of new prototypes.

Kurzfassung

Der Kosmische Höhenstrahl Messstand in Garching dient der Kalibration großflächiger Spurdetektoren mit kosmischen Myonen. Zur Zeit werden Microegas Detektoren im Messstand untersucht, die als Verbesserung des New Small Wheels im ATLAS Myon Spektrometer vorgesehen sind.

Um die Fähigkeit des Messstandes zu erhöhen, einen Schnitt auf hoch energetische Myonen zu setzen, wird ein Detektor entwickelt, mit dem die Kleinwinkelstreuung von Myonen an Eisen gemessen wird. Der Detektor besteht aus einem Plasiksoszintillator mit zwei dimensionaler Ortsauflösung und Triggerfähigkeit. Die Auslese des Detektors wird mit wellenlängenschiebenden Fasern, die an Silizium Photomultiplier (SiPMs) gekoppelt werden, realisiert.

Ferner handelt es sich um einen modularisierten Szintillator, dessen einzelne Module aus je zwei Trapezoiden bestehen, welche optisch von einander getrennt sind. Durch Messung der Zeit, die das Licht benötigt, um von seinem Entstehungsort zum SiPM zu gelangen, lässt sich die Position des Myon-Durchgangs in einer Raumrichtung bestimmen. Für die andere Richtung vergleicht man die Lichtmenge in beiden Hälften eines Moduls, welche von der Wegstrecke der Myonen im Szintillator abhängt und damit von der Position bezüglich des Trapezes.

Diese Arbeit präsentiert die Ergebnisse einer Strahlzeit am CERN mit einem Prototyp. Anhand dieser kann das grundsätzliche Funktionsprinzip des Detektors nachgewiesen werden. In dieser Arbeit werden Messungen vorgestellt, die zur Verbesserung des Detektors dienen. Hierzu werden lichtreflektierende neue Materialien zur optischen Trennung der Trapezoide untersucht. Ebenfalls werden in einer selbst entwickelten Simulation neue Detektorgeometrien und Faserpositionen untersucht.

Anhand der Messungen und Simulationen lässt sich zeigen, dass diffus reflektierende Trennmaterialien die detektierte Lichtmenge verdoppeln. Zusätzlich werden schmalere Geometrien als beim Prototypen simuliert, die zur einer Verbesserung der Ortsauflösung beitragen. Ebenfalls wird gezeigt, dass eine Faserposition an einer Kante des Szintillators sich positiv auf die Ortsbestimmung auswirkt.

Die gefundenen Ergebnisse aus Messung und Simulation fließen in den Bau neuer Prototypdetektoren ein.

Contents

1	Introduction	1
2	Overview of Scintillation Detectors	5
2.1	General Characteristics	5
2.2	Plastic Scintillators	7
2.3	Wavelength Shifter and Franck-Condon-Principle	10
2.4	Energy Loss of Particles in Matter	13
3	Photon Detectors	15
3.1	Classical Photomultiplier Tubes	15
3.2	Silicon Photomultiplier	16
3.3	Comparison of both Detector Types	23
4	Description of General Setup	29
4.1	Photon Detection with SiPMs	29
4.2	Photon Detection with PMTs	32
4.3	Flash-ADC Readout	33
4.4	QDC Readout	36
5	Basic Idea of the Detector	39
5.1	Position Resolution in x -Coordinate	41
5.2	Position Resolution in y -Coordinate	43
5.3	Multiple Coulomb Scattering	45
6	Test of a Prototype Detector at CERN	47
6.1	Timing Information: The x -Direction	49
6.2	Pulseheight Information: The y -Direction	59
7	Light Output Studies	63
7.1	Measurement with Different Reflective Cover	63
7.2	Monte Carlo Simulation of Light Propagation	73
7.2.1	Comparison of the Simulation to the Measurement	77
7.2.2	Fiber Position	87
7.2.3	Detector Geometry	92

8	Position Determination Techniques	101
9	Conclusion and Outlook	105
	List of Abbreviations	I
	List of Figures	III
	List of Tables	VII
	Bibliography	IX
	Appendix A Instruction Sheet for the Simulation	XIII
	Appendix B Comparison of Measurement and Simulation	XIX

1 Introduction

The Cosmic Ray Facility ([CRF](#)) in Garching has the potential to reconstruct individual tracks of cosmic muons with a position accuracy below $50\ \mu\text{m}$. It was used to calibrate 98 [BOS MDT](#)¹ chambers. These large area tracking detectors are contributed to the ATLAS experiment at [CERN](#) by the LMU Munich and the Max Planck Institute for Physics.

Presently the [CRF](#) is used to investigate large area *Micromegas* detectors foreseen for the New Small Wheel upgrade of the ATLAS muon spectrometer at high luminosity [LHC](#). Figure 1 shows a large area *Micromegas* in between two layers of reference chambers.

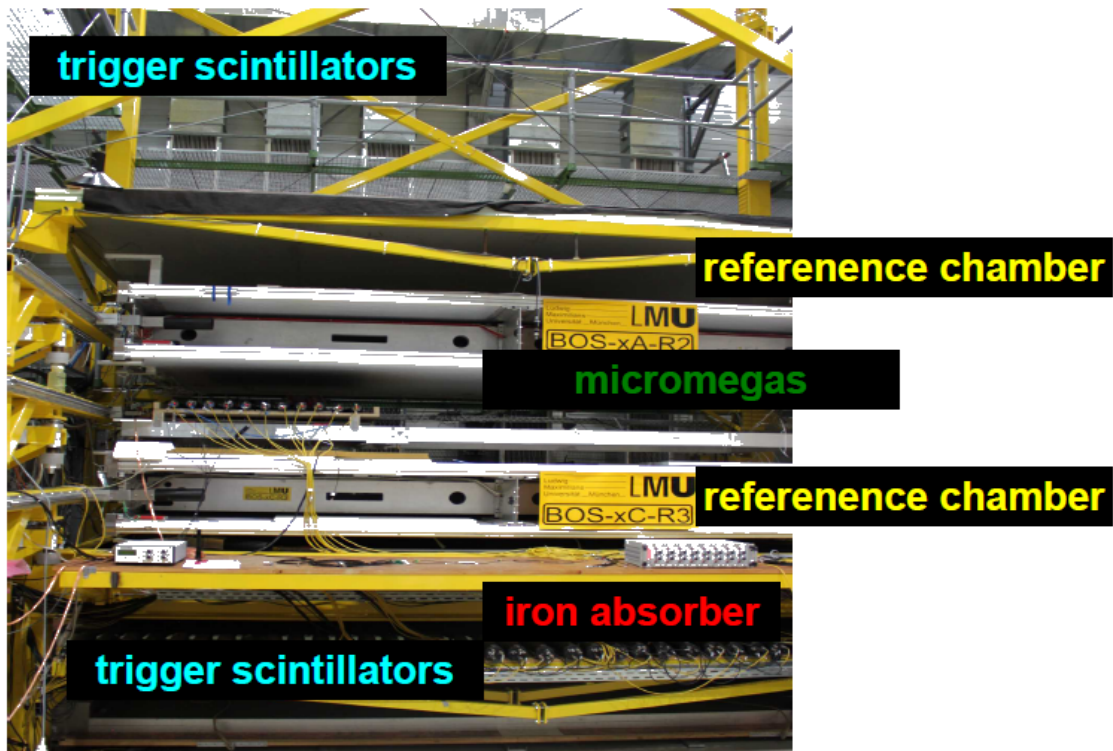


Figure 1: Photograph of [CRF](#). The device under test in this case is a *Micromegas* detector [[Ruschke, 2014](#)].

¹monitored drift tubes ([MDT](#)) are currently built in the barrel outer small ([BOS](#)) position of the ATLAS detector as muon detector

Two precision BOS drift-chambers provide for this propose a tracking information which is compared to the track information measured by the *Micromegas* detector. To enhance the performance of the CRF, a new energy selector, based on multiple scattering of muons in an iron absorber, will be installed. The goal is to include only muons with energies above 600 MeV in the analysis to minimize multiple scattering in the active detector parts. A two dimensional spatially resolving muon detector with trigger capability is presently developed based on plastic scintillators with silicon photomultiplier (SiPM) readout. The position resolution of this detector will be achieved due to the geometrical shape of an array of scintillators. A sketch of the CRF with an integrated energy selector is shown in figure 2.

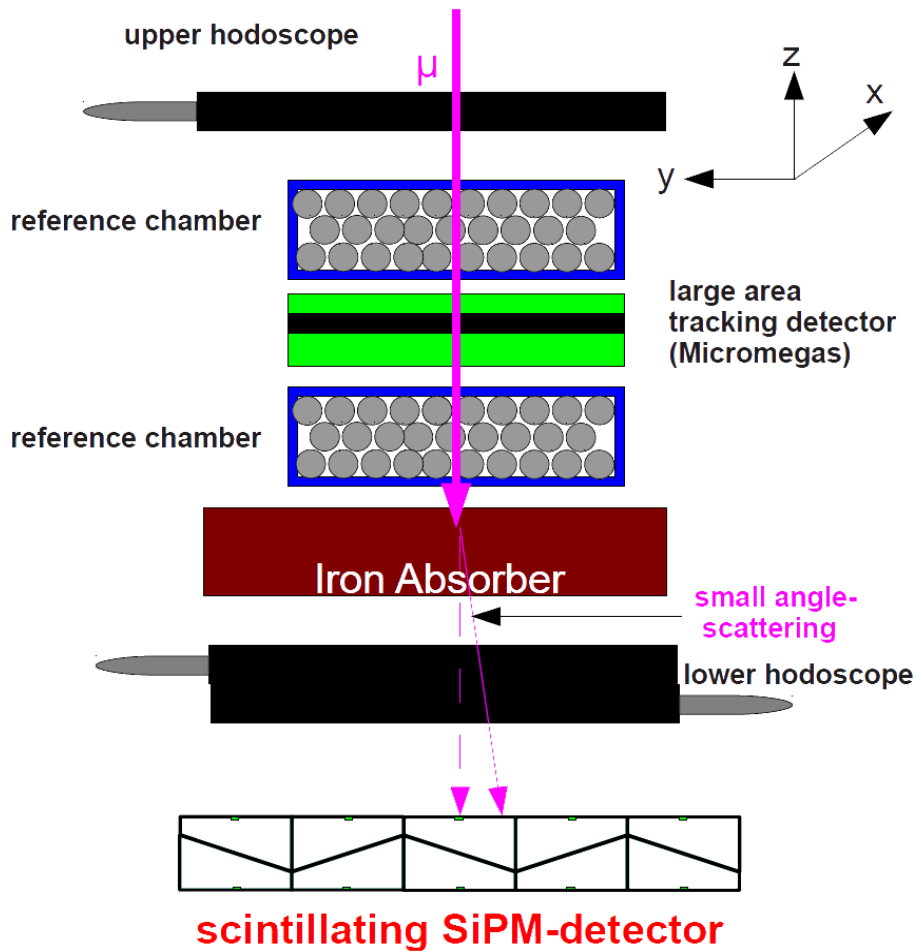


Figure 2: Scheme of the CRF with the new energy selecting unit, comprising trapezoidal shaped scintillators with SiPM readout.[Ruschke, 2014].

Due to the iron absorber underneath the second reference chamber, all muons are scattered from their original track. The scattering angle will increase as the energy of the muon decreases. If one compares the predicted track of the muon from the reference chambers to the position in the scintillating tracking detectors, one can set a cut on the average angle of multiple scattering and thus on the energy of the muon.

In this thesis we will present the results of a first prototype detector and measurements to enhance its light output. The light output is a crucial figure of merit of the detector, since it is correlated to the position resolution.

2 Overview of Scintillation Detectors

Scintillators are one of the most common detector types for particle or radiation detection. The scintillator consists of materials, that convert energy from penetrating radiation to visible light. A photomultiplier, described in chapter 3, then converts the scintillation light to a measurable electrical signal. The photomultiplier can be either directly connected to the scintillator, or to an intermediate wave guide, for details see chapter 4. The following chapters will describe the properties of scintillators, especially the one used for this tracking detector.[Leo, 1994]

2.1 General Characteristics

A complete scintillation detector consists out of three basic components: the scintillator, a photomultiplier and the readout electronic.

There are three main features of scintillation detectors, making them attractive for the use as particle detectors:

1. **Sensitivity to Energy:** In most cases scintillators show a direct proportionality between their light yield and the deposited energy by a passing particle. The photomultiplier, if operated properly, shows the same proportionality. This results in a linear behavior of the pulseheight compared to the energy loss of the penetrating radiation.
2. **Fast Time Response:** Compared to other detector types, like drift chambers, scintillation detectors are very fast. This means, that their response and recovery times are short². The fast response time makes them ideal for a use as trigger detectors and the fast recovery time allows to count particles at high rates due to a small dead time.
3. **Pulse Shape Discrimination (PSD):** For some scintillators the shape of the signal varies for different particles passing the detector. With PSD it is then possible to distinguish between different particles.

The first two points are crucial for the operation principle of this tracking detector. The process in which energy is converted to visible light is called luminescence. If

²For plastic scintillators a signal lasts roughly $\approx 5 ns$, [Leo, 1994], see chapter 2.2.

the emission occurs in the first 100 ns , the luminescence is called fluorescence³. In case of a longer relaxation the process is called phosphorescence. An explanation of both types can be found in section 2.2.

For the number of emitted photons during a scintillation process one can, in a first approximation, neglect the response time and describe the emission process as an exponential decay.

$$N(t) = N_0 \cdot \exp\left(-\frac{t}{\tau}\right) \quad (2.1.1)$$

With the number of emitted photons N , the total number of photons N_0 and the decay constant τ . A shape of such a decay can be seen in figure 3.

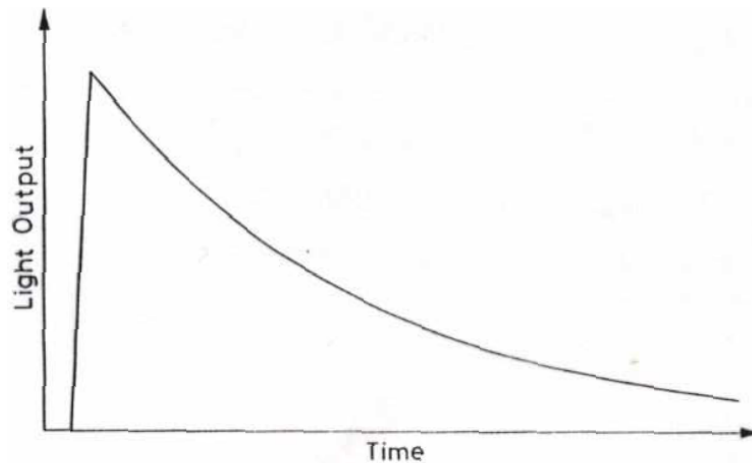


Figure 3: Light emission of a scintillator described by an exponential decay [Leo, 1994].

Having a closer look on the decay processes it turns out, that a function containing two exponentials describe the emission process better than equation 2.1.1.

$$N(t) = A \cdot \exp\left(-\frac{t}{\tau_f}\right) + B \cdot \exp\left(-\frac{t}{\tau_s}\right) \quad (2.1.2)$$

This means, that one has two separate decays: one, which happens fast ($\Rightarrow \tau_f$), and one, which is rather slow ($\Rightarrow \tau_s$), as drawn in figure 4. The magnitudes of the two exponentials, A and B , are material dependent, but A is in general larger [Leo, 1994].

³This is roughly the time scale of atomic transitions [Leo, 1994]

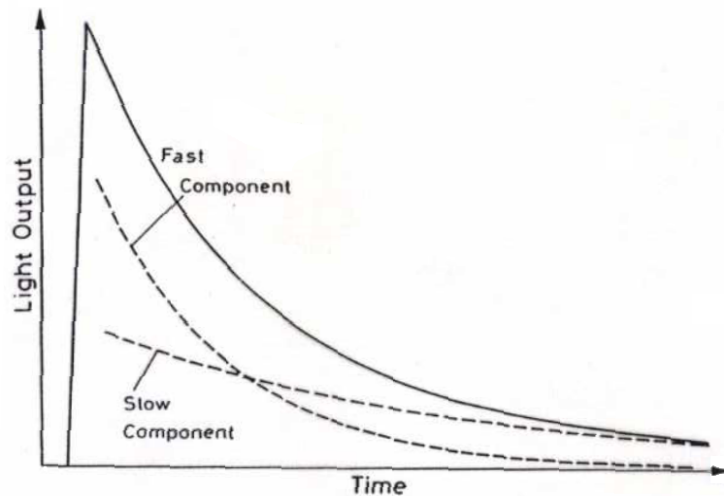


Figure 4: Light emission of a scintillator described by a superposition of a fast and a slow exponential decay [Leo, 1994].

One can find six types of scintillator materials used in current research: organic plastics, organic crystals, organic liquids, inorganic crystals, glasses and gases. The material, we use, is a plastic scintillator called BC 400 from Saint Gobain Crystals [Saint Gobain, 2005]. In the following we concentrate on plastic scintillators.

2.2 Plastic Scintillators

Plastic scintillators, as well as other organic scintillators, are hydrocarbon compounds containing benzene-ring structures. The BC 400 plastic scintillator consists mainly out of polyvinyltoluene which has one benzene ring per repetition unit, as shown in figure 5.

The following description of the scintillation process is valid for all organic scintillators. The special case of an organic plastic is discussed after wards.

The free valence electrons⁴ of the benzene-ring are responsible for the scintillation process. Figure 6 shows an energy level scheme of the π -electrons with spin singlet states, denoted with a S, and spin triplet states, denoted with a T, which are separated from each other for better visualization.

⁴Delocalized electrons occupying the π -molecular orbitals.

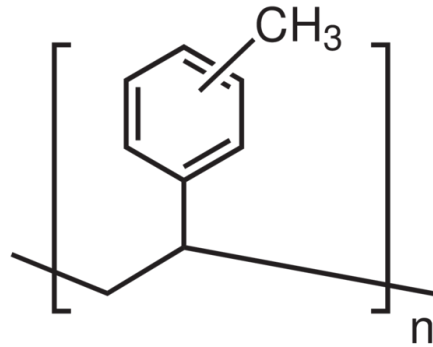


Figure 5: Repetition unit of polyvinyltoluene. The methyl group can sit on an arbitrary C-atom of the benzene ring, except the one where the benzene itself is coupled to the polymer [Sigma-Aldrich, 2013]

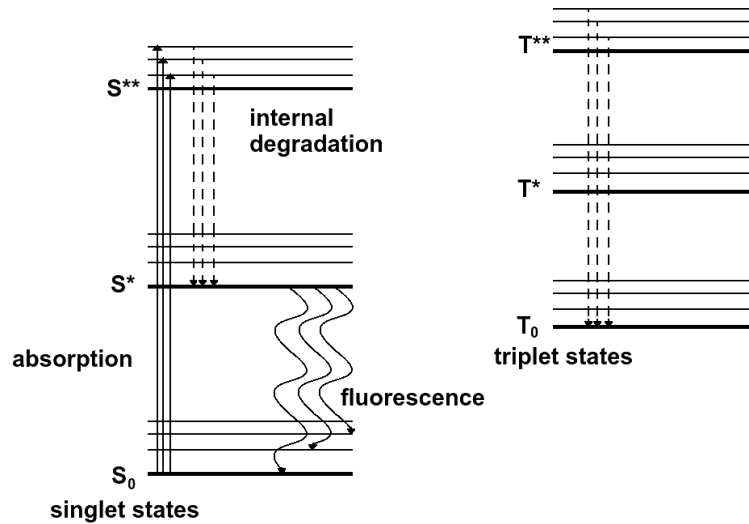


Figure 6: Energy level scheme of π -electrons

The thin horizontal lines, parallel to the thick S and T lines, represent the fine structure levels of the corresponding singlet or triplet level with an energy spacing of $\approx 0.16 \text{ eV}$ [White, 1988]. Penetrating radiation excites electrons in all possible states (solid arrows). The excited singlet states usually decay "immediately" ($\leq 10 \text{ ps}$) to the first excited level S^* (dashed arrows) [Leo, 1994]. This decay happens without emission of photons and is called internal degradation. The energy from this transmission goes into molecular vibration modes, called phonons. From

the S^* state the electrons will relax to the ground state or its fine structure modes by emission of light (wavy arrows). This decay happens in few nanoseconds⁵, making it the fast exponential component of equation 2.1.2.

The excited triplet states decay to their ground state T_0 also via internal degradation. A direct decay to the singlet ground state is forbidden by selection rules. The relaxation to the ground state happens via an interaction with another excited molecule:



The S^* state then decays by emission of fluorescence light to the S_0 states. The whole process needs a certain amount of time, corresponding to the slow component of equation 2.1.2.

In case of an organic plastic scintillator the response time of the scintillator can't be ignored any more due to the very fast recovery times of $\leq 3 \text{ ns}$ for such materials [Leo, 1994]. But on the other hand one can now neglect the slow component of the relaxation. It turned out, that the complete scintillation process can be described by a convolution of a Gaussian with an exponential function.

$$N(t) = N_0 \cdot f(\sigma, t) \exp\left(-\frac{t}{\tau}\right) \quad (2.2.2)$$

Where f is a Gaussian and σ is its standard deviation. For our scintillator the two constants are [Leo, 1994]:

$$\sigma = 0.7 \text{ ns}, \quad \tau = 2.4 \text{ ns} \quad (2.2.3)$$

Another characteristic of a scintillator is the amount of energy it takes to create a photon. These values differ for different scintillator types. For our plastic scintillator a penetrating particle has to lose $\approx 100 \text{ eV}$ of its energy for the production of a single photon [Leo, 1994].

The scintillating material is barely transparent to the light coming from relaxation to fine-structure state. To reduce the overlap of the absorption and emission spectrum of the scintillator, one uses secondary scintillating materials. These materials absorb the scintillation light of the primary scintillator and emit photons with a

⁵ \Rightarrow Fluorescence, see section 2.1.

longer wavelength [White, 1988]. Due to this effect the secondary scintillating substances are called wavelength shifter. In the next section we want to have a closer look on such materials.

2.3 Wavelength Shifter and Franck-Condon-Principle

Most of the transitions of a scintillating process happens in the UV region where the scintillator is just barely transparent. To improve the light output, or to fit the wavelength of the scintillation light to the region of the highest sensitivity of the photomultiplier, one adds wavelength shifting components, to the scintillating material to shift the UV light in the visible spectrum. These components are called fluors⁶. Commonly used fluors are for example PTP or POPOP [Biebel, 2009]. In a scintillator the concentration of fluors is rather small ($\leq 1\%$) and the energy loss of penetrating radiation goes mainly into the excitation of the primary scintillator [White, 1988]. A sketch of the scintillation process within a scintillator can be found in figure 7.

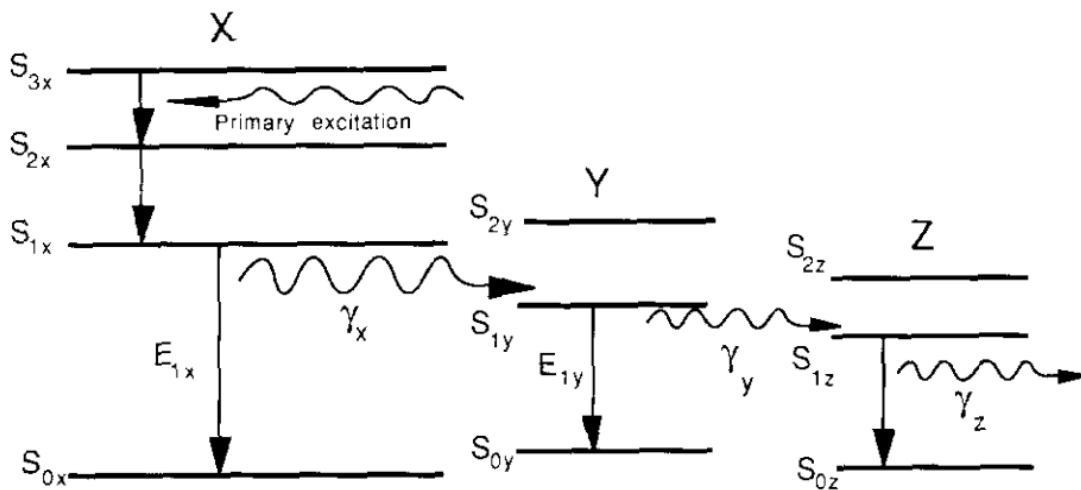


Figure 7: Scheme of wavelength shifting progress in an organic plastic scintillator. X is the primary scintillating material, Y and Z are subsequent fluors. [White, 1988].

The wavelength shifting is described by the Franck-Condon-Principle, as sketched in figure 8 [Herzberg, 1991].

⁶Not to confuse with the element fluor.

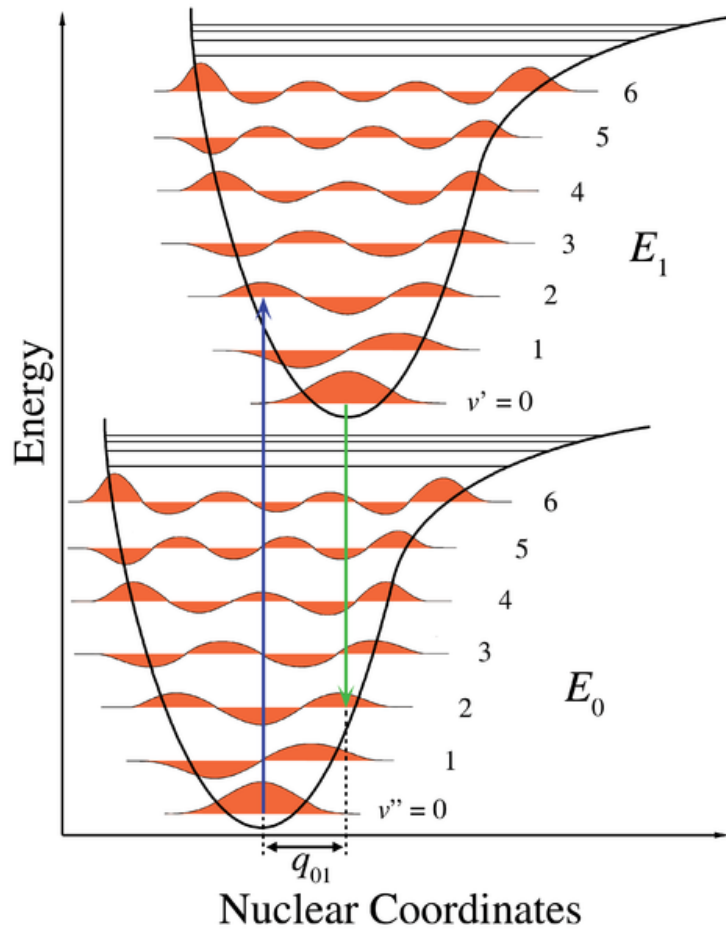


Figure 8: Scheme of energy levels explaining the Franck-Condon-Principle [Wikipedia, 2013].

An UV photon, coming from a scintillating process, can excite atoms of the fluor, represented by the blue line in figure 8. The excited level can be any vibration mode⁷ of the next electron level. The vibrational mode will immediately decay to its ground state by internal degradation, as described earlier. During the excitation process an atom of the molecule will be displaced a bit, so that the wave function of the vibrational ground state of the first excited electron level has less or even no overlap with the wave function of the ground state of the atom. According to the Franck-Condon-Principle, the most probable transition for the decay is the one, for which the wave functions show the biggest overlap. The atom therefore will

⁷The excitation, of course, has to respect multipole selection rules.

decay to one of the vibrational modes of the ground state, but not to the absolute ground state. This decay is illustrated by the green line in figure 8. Here one can see, that the overlap of the second vibrational mode of the ground state E_0 has the largest overlap with the first excited state E_1 . The energy of the emitted photon will have a smaller energy than the absorbed one, what results in a shift towards longer wavelengths.

Figure 9 shows the emission spectrum of the plastic scintillator BC 400.

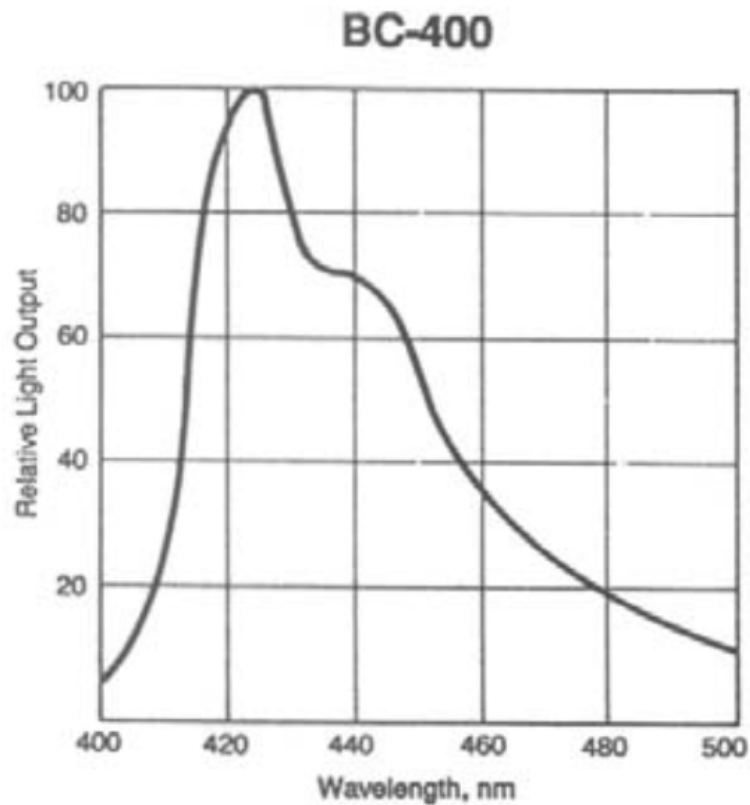


Figure 9: Light emission Spectrum of BC 400 [Saint Gobain, 2005].

2.4 Energy Loss of Particles in Matter

The mean energy loss⁸ of particles in matter is described by the Bethe-Bloch equation 2.4.1 [Lutz, 2007].

$$-\left\langle \frac{dE}{dx} \right\rangle = 2\pi r_e^2 \cdot m_e c^2 \varrho \cdot \frac{N_A \cdot Z z^2}{A \cdot \beta^2} \cdot \left(\ln \frac{2m_e c^2 \beta^2 \gamma^2 T_{max}}{I^2} - 2\beta^2 - \delta - 2\frac{C}{Z} \right) \quad (2.4.1)$$

with

r_e	$= \frac{e^2}{4\pi\epsilon_0 m_e c^2}$	≈ 2.82	fm	class. electron radius
$m_e c^2$		≈ 0.511	MeV	electron mass $\times c^2$
N_A		$\approx 6.022 \cdot 10^{23}$	$\frac{1}{mol}$	Avogadro constant
Z, A				atom number, atom weight
ϱ				density
z				charge of particle
T_{max}	$= \frac{2m_e c^2 \beta^2 \gamma^2}{1+2\gamma \frac{m_e}{M} + \left(\frac{m_e}{M}\right)^2}$			maximum energy transfer
M				mass of particle
β	$= \frac{v}{c} \equiv \frac{pc}{E}$			speed of particle
γ	$= \frac{1}{\sqrt{1-\beta^2}} \equiv \frac{E}{Mc^2}$			Lorentz-factor of particle
E, p				energy, momentum of particle
δ	$\propto \log_{10}(\beta\gamma)$			density correction
C	$\propto \frac{I^2}{\beta^2 \gamma^2}$			atomic shell correction

For muons passing copper, the mean energy loss, depending on the muons energy, is plotted in figure 10.

The muons and pions, investigated in this work, are considered to be minimum ionizing particle (MIP). The distribution of momentary energy loss of such particles in scintillators is highly skewed as long as their path length is of moderate length. The probability distribution of the energy loss follows a Landau distribution [Landau, 1944]. Figure 11 shows experimental data from our detector fitted with a Landau distribution. The long tail of the distribution means, that a muon can produce a high amount of photons in a single interaction (compared to the average photon production) with a not vanishing probability.

⁸also stopping power

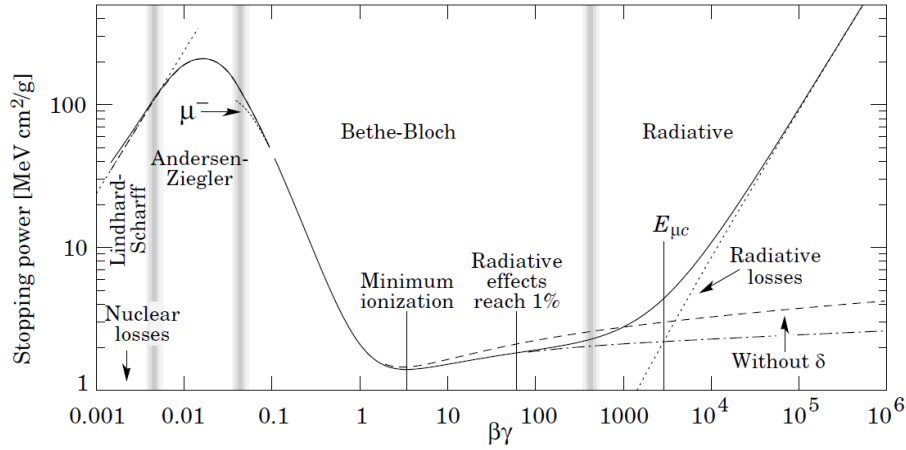


Figure 10: Stopping power for positive muons in copper [Groom et al., 2001].

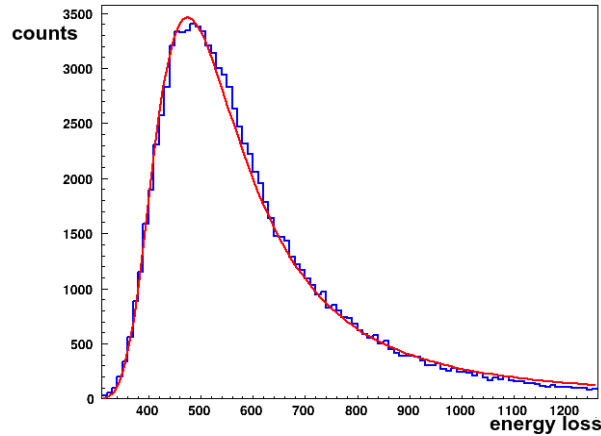


Figure 11: Experimental data (blue) taken from our detector. Landau distribution (red) fitted to the data. Arbitrary units on x axis.

In total, the deposited energy in the scintillator depends on the particle energy, path length in the active volume and the Landau distributed energy loss per interaction with the scintillator. The extraction of the path length out of the pulseheight is an important step in the position determination, see chapter 5. In order to calculate the path length out of the pulseheight of the signal, one has to find ways to eliminate the dependency on the particle energy and the Landau distributed energy loss. The quality of this elimination sets a limit to the position resolution of a detector. In the next chapter we discuss photomultiplier, with which we convert the optical pulse of a scintillator to an electrical signal.

3 Photon Detectors

There are various ways to convert electromagnetic light into an electrical signal. In this work two devices are used: the semiconductive silicon photomultiplier (**SiPM**) and the classic photomultiplier tube (**PMT**).

The **SiPM** is one of the basic devices of the trapezoidal tracking detector investigated in this thesis. It has several advantages compared to a **PMT**, which will be discussed later in section 3.3, but since it is a rather new device, we consider it as less understood than photo tubes. Therefore, to understand, study and optimize the geometry of the trapezoidal structure, we additionally use **PMTs** for measurements concerning the light output of the scintillator.

Both devices are introduced and compared in the following sections.

3.1 Classical Photomultiplier Tubes

Classic **PMTs** are devices, to convert electromagnetic waves to electronic signals using the photo-electric effect. Figure 12 shows the schematic principle of a **PMT**.

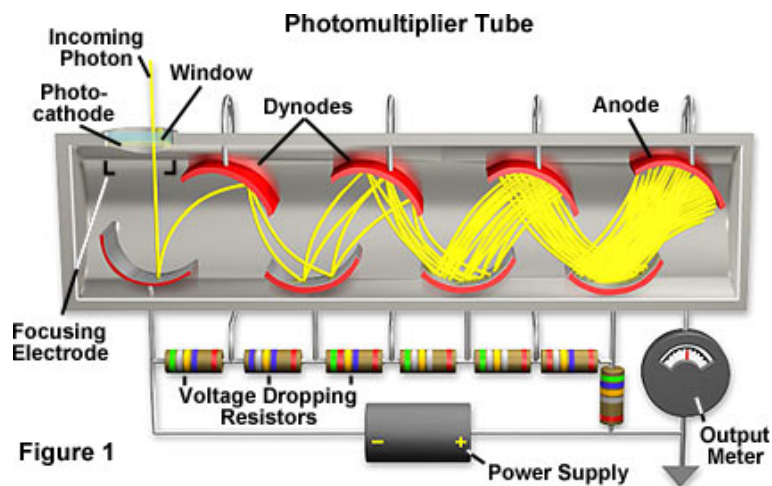


Figure 12: Schematic principle of a **PMT** [Abramowitz and Davidson, 2006]

A **PMT** consists of a vacuum tube containing a photo cathode and several electrodes, called dynodes. Dynodes are electrodes acting like anodes as well as like cathodes. They attract electrons from the dynode before and release electrons to the next dynode.

Incoming photons are converted in the bi-alkali-photo-cathode to electrons via photo-effect. An acceleration voltage is applied to the series of dynodes in such a way, that electrons created on one of the electrodes, are accelerated to the next one. A voltage divider creates the continuous electric field along the series of electrodes. Electrons coming from the bi-alkali-cathode gain energy on their way to the first dynode. The energy is high enough, that each electron coming from the cathode can knock several more electrons out of the dynode. These released electrons fly to the next dynode where an analogous electron multiplication takes place. This process is repeating itself until the electron avalanche hits the last electrode in the row, which is the final anode. It is connected to a readout system and in parallel to ground-potential. Electrons arriving at the anode lead to a charge signal in the readout system, which is recorded by a computer, see chapters 4.3 and 4.4.

3.2 Silicon Photomultiplier

SiPMs in some sense can be seen as a semiconductor analogous to classic PMTs. In contrast to PMTs, SiPMs use the inner photo electrical effect to convert scintillation light to electron-hole pairs. A SiPM consists of an array of avalanche photo diodes (APD), which are connected in parallel. In figure 13 each combination of a quenching resistor and an APD corresponds to one pixel of a SiPM, which are operated in reverse biased mode.

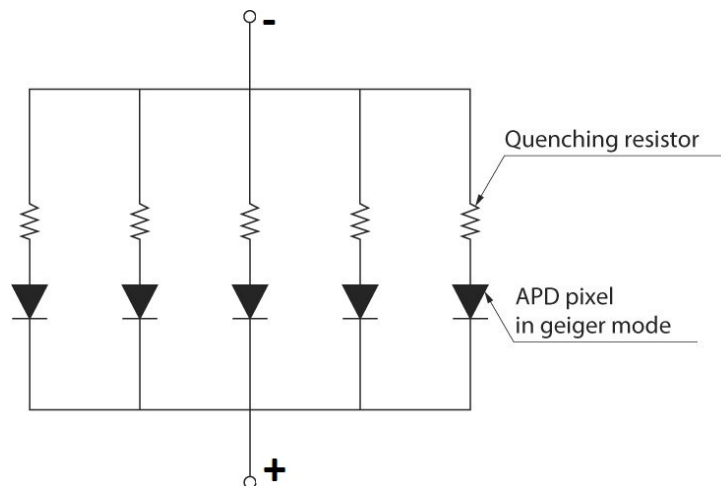


Figure 13: Equivalent circuit diagram for a SiPM [Hamamatsu Electronics, 2008]. Each combination of an APD and a resistor represents a pixel in the SiPM.

A sketch of the doping layers in an APD is displayed in figure 14.

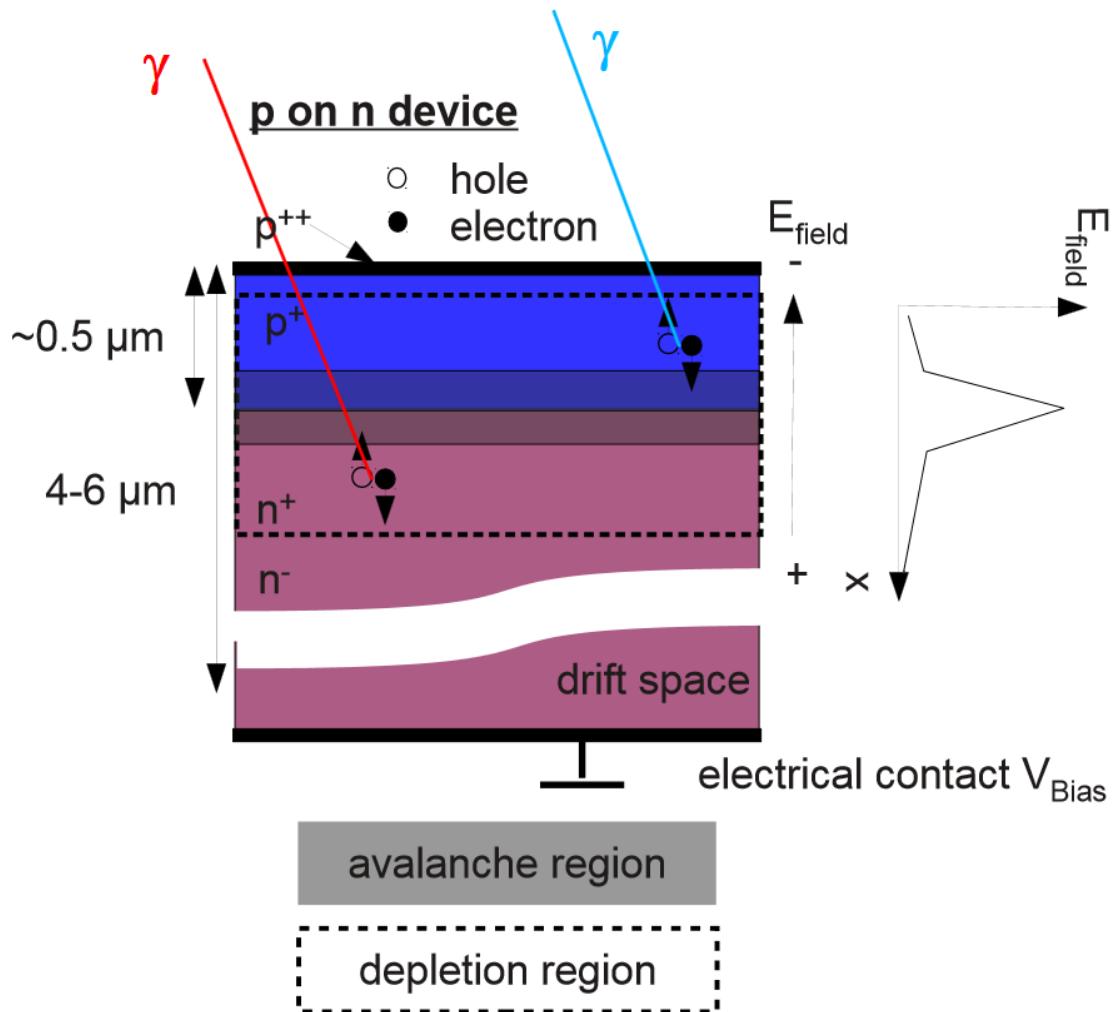


Figure 14: Schematic of a pn junction as used in Hamamatsu SiPMs [Ruschke, 2014].

The electrical field in the depletion region of an APD can be as high as $10^7 \frac{V}{cm}$. If a photon hits the active area of an APD, it excites a valence electron into the conduction band, leaving a hole in the valence band. The hole can be considered as a free positive charge carrier since electrons from neighboring atoms can jump into the hole, leaving a hole in their original position. The electron follows the electric field lines of the applied voltage and moves to the anode while the holes move to the cathode. On their ways they may pass the high field region of the

depletion zone. If the applied bias voltage (V_{bias}) is high enough, and therefore the electric field is large enough in the depletion zone, new electron hole pairs can be excited. Depending on V_{bias} one can divide the behavior of the diode in three branches [Lutz, 2007]. There are two characteristic voltages separating these branches. The lower one is called critical voltage (V_{crit}) and the upper one is called breakdown voltage (V_{BD}).

- If V_{bias} is lower than V_{crit} , i.e. $0 < V_{bias} < V_{crit}$, there will be no amplification at all. The electron and the hole are accelerated to their electrodes but never reach an energy, where they can further create electron-hole pairs. The gain of the SiPM in this region is therefore one.
- If $V_{crit} < V_{bias} < V_{BD}$, the electron gets on its way to the anode enough energy to create further electron-hole pairs, which themselves can excite further electron-hole pairs. The holes have a smaller ionization coefficient than the electrons in silicon [Leo, 1994], such that the production of further electron-hole pairs due to hole impacts can be neglected in first order. This results in an avalanche which is just triggered by electrons and will therefore stop, when all of them have reached the anode.
The pulseheight of the signal is proportional to the number of incident photons. This mode is called the proportional mode.
- The last mode is called the Geiger mode, due to the analogous behavior to Geiger-Müller-counters. If $V_{bias} > V_{BD}$, also the holes get enough energy to create new generations of electron-hole pairs [Lutz, 2007]. The avalanche is now also supported by holes. Without an external quenching, it will grow and finally destroy the diode. This is where the quenching resistor comes into play. The current, caused by the avalanche, results in a current through the quenching resistor. This causes a voltage drop at the resistor. The V_{bias} at the diode will consequently drop below V_{BD} and the avalanche will stop. After the detection of one photon, the diode recharges again and is ready to detect the next photon.

Due to the divergent amplification in the Geiger mode it is impossible to reconstruct the amount of incident photons triggering the avalanche in the APD. By introducing an array of diodes and making each diode very small, incident photons

hit different pixels. For linear response, the number of pixels must be large enough, that a pixel is hit only once. Figure 15 shows theoretical values of the number of responding pixels for a SiPM, which has 100 pixels on 1 mm^2 active area. As long as there is linear correlation between the number of incident photons and the number of firing pixels, one can recover the amount of incident photons.

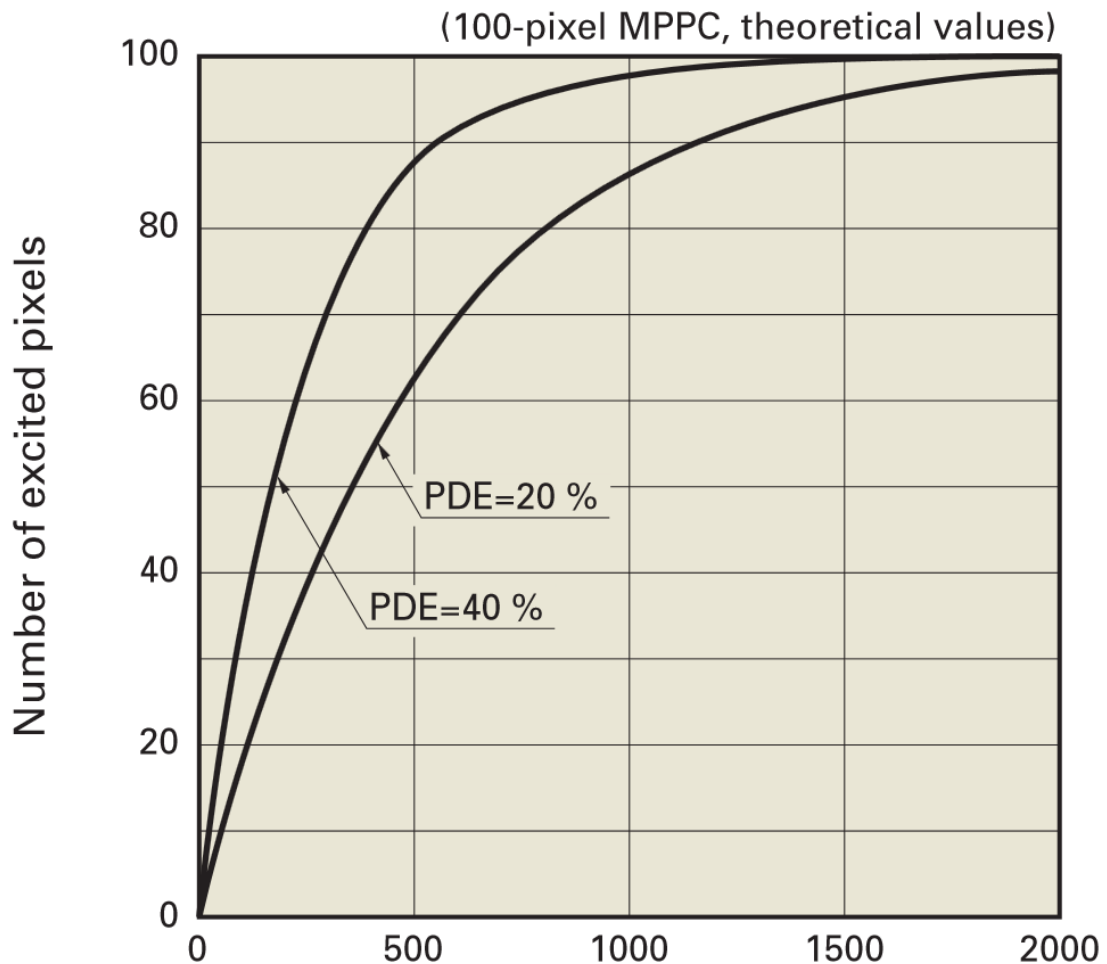


Figure 15: Correlation of the number of incident photons and the number of fired pixels for low photon detection efficiencies [Hamamatsu Electronics, 2008].

The gain of a SiPM depends on the difference between V_{bias} and V_{BD} , called over voltage (V_{over}). But V_{BD} is temperature depending, while V_{bias} is a fixed value from a power supply. Furthermore V_{BD} is different for each SiPM. For the determination of V_{BD} we use a setup in a climate chamber, which ensures a constant temperature of $20 \pm 0.1\text{ }^\circ\text{C}$. The description of the setup and the proceeding of

the measurement can be found in [Ruschke, 2014]. After determine V_{BD} for each SiPM, we could apply to each of it the same over voltage and therefore each SiPM in the setup has the same gain.

During a test beam at CERN, which will be discussed in more detail in chapter 6, it turned out, that this detector has a rather low light yield. Therefore it is important to detect as many photons as possible with the SiPM. The photon detection efficiency (PDE) of SiPMs is given by [Gomi et al., 2006]:

$$\text{PDE} = \varepsilon_{\text{geom}} \cdot \text{QE} \cdot \varepsilon_{\text{Geiger}} \quad (3.2.1)$$

The geometrical efficiency ($\varepsilon_{\text{geom}}$) depends on the photo sensitive area of a SiPM. The devices used in this setup are Hamamatsu SiPMs with two different active areas:

- $1 \times 1 \text{ mm}^2$ active area
- $3 \times 3 \text{ mm}^2$ active area

and three different pixel sizes:

- $25 \times 25 \mu\text{m}^2 \hat{=} \frac{40 \times 40 \text{ pixels}}{\text{mm}^2}$
- $50 \times 50 \mu\text{m}^2 \hat{=} \frac{20 \times 20 \text{ pixels}}{\text{mm}^2}$
- $100 \times 100 \mu\text{m}^2 \hat{=} \frac{10 \times 10 \text{ pixels}}{\text{mm}^2}$

Hamamatsu offers three different packages of their SiPMs: metal, ceramic and glass epoxy. To label the different types, we refer to the pixel size and the package type, e.g. the SiPM with a pixel size of $100 \times 100 \mu\text{m}^2$ and a ceramic package is called 100C. We use only the ones with a ceramic package. Pictures 16 and 17 show 100C SiPMs with $1 \times 1 \text{ mm}^2$ and $3 \times 3 \text{ mm}^2$ active area respectively.

The more pixel per mm^2 a SiPM has, the higher is the achievable resolution of incident photons, since it is more likely for two close by photons to hit different pixels. Also the range of a proportionality between incident photons and the pulse-height of the signal is higher, if the SiPM has more pixels on the same area. But there is also a disadvantage due to an increasing number of pixels. The pixels must be shielded against each other, see section 3.3, resulting in insensitive area. The percentage of the photo sensitive area to the whole active area is called fill factor

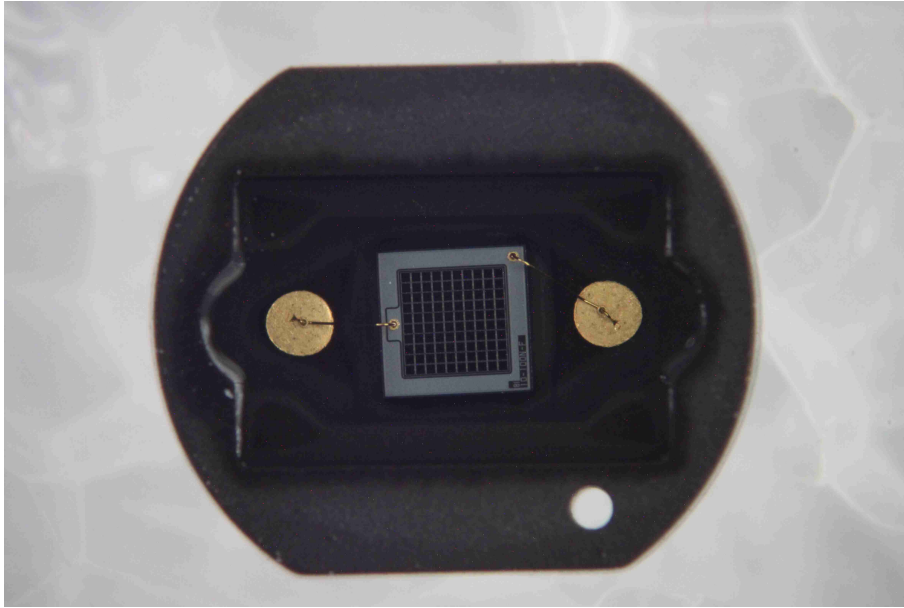


Figure 16: Microscopic picture of the $1 \times 1 \text{ mm}^2$ SiPM with a pixel size of $100 \mu\text{m}$.

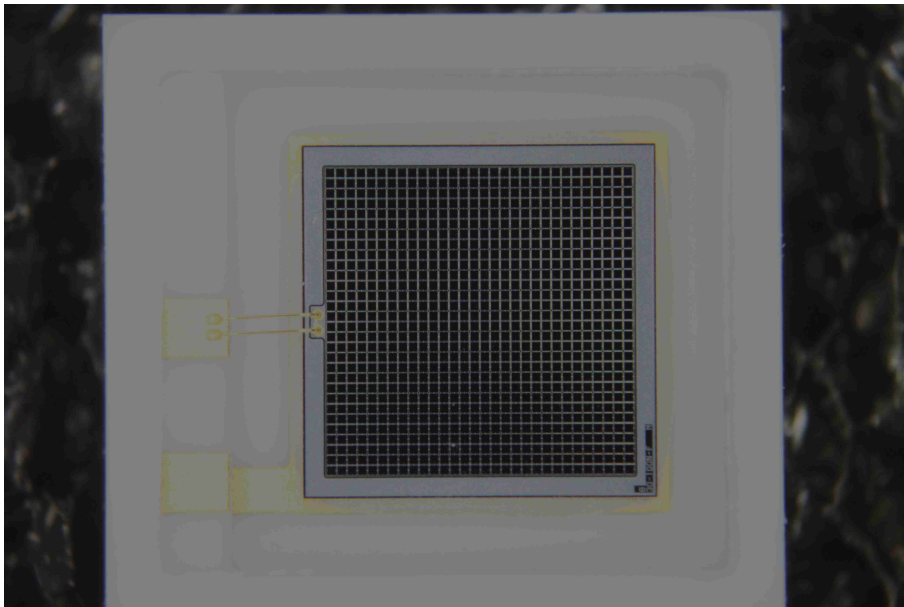


Figure 17: Microscopic picture of the $3 \times 3 \text{ mm}^2$ SiPM with a pixel size of $100 \mu\text{m}$.

ϵ_{geom} . It ranges from 0.3 for the $25 \mu\text{m}$ case to 0.7 for the $100 \mu\text{m}$ type [Gomi et al., 2006]. Figure 18 displays again 100C SiPM with an active area of $3 \times 3 \text{ mm}^2$ but this time it is zoomed in to see insensitive space between the pixels.

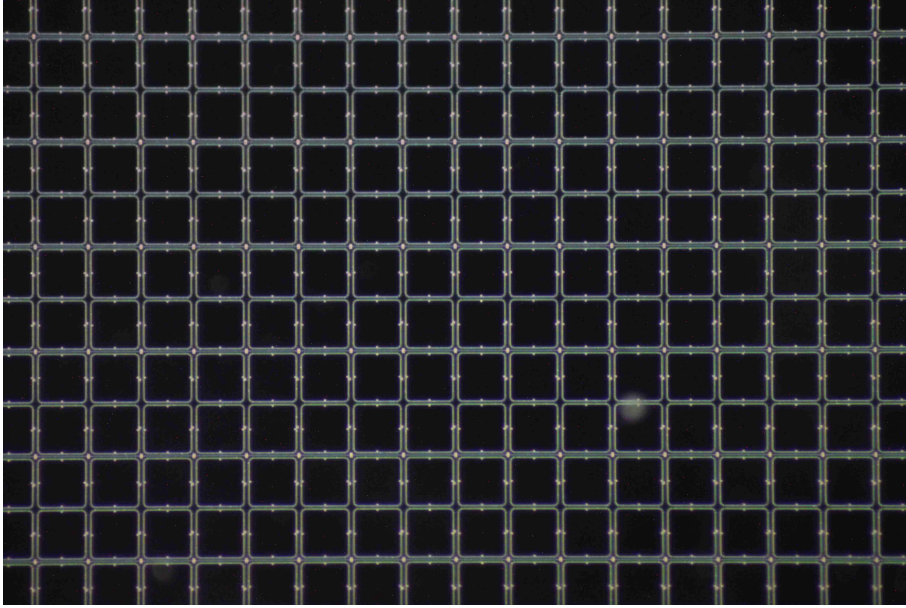


Figure 18: Microscopic picture of the $3 \times 3 \text{ mm}^2$ SiPM with a pixel size of $100 \mu\text{m}$. The black squares are pixel, while the rest is insensitive space.

The quantum efficiency (QE) depends on the wavelength of the photons and describes the ratio of incident photons to detected photons. For example a photon can be back reflected at the coating of the SiPM and will therefore not be detected. To increase the efficiency of the setup, the peak wavelength of the emitted light from the wavelength shifting fiber (WLSF) should fit to the peak wavelength for photon detection efficiency of the SiPM. Figure 19 shows the absorption and emission spectra of the used WLSF BCF 92 with a peak emission at $\lambda_{peak\ emission} = 492 \text{ nm}$ [Saint Gobain, 2011b].

The shape and the value of BCF 92 fits to the PDE of the SiPM as shown in figure 20. The peak sensitivity for the Hamamatsu SiPMs is at $\lambda_{peak\ detection} = 444 \text{ nm}$ [Hamamatsu Electronics, 2008]. Each incident photon has a certain efficiency to trigger an avalanche (ε_{Geiger}). Even if a photon with a suitable energy hits the sensitive area of the SiPM it still does not necessarily trigger an avalanche. To increase ε_{Geiger} one has to increase V_{bias} .

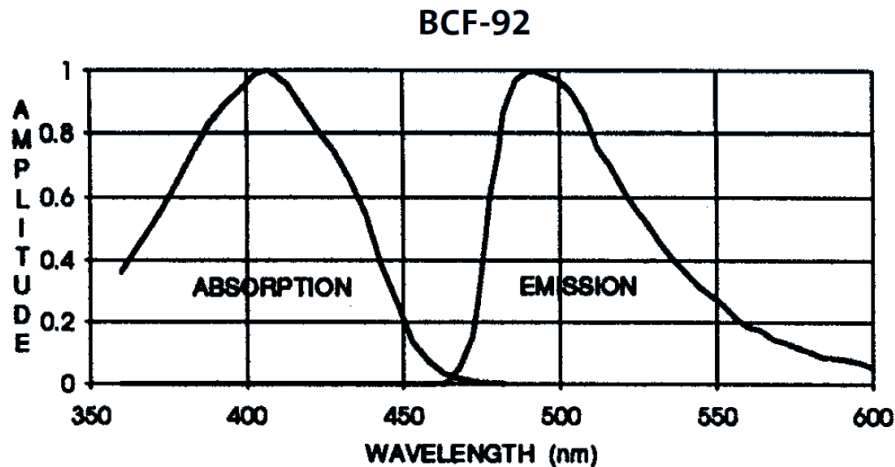


Figure 19: Absorption and emission spectra of BCF 92 [Saint Gobain, 2011b].

3.3 Comparison of both Detector Types

Finally we want to compare both photo multipliers and give reasons for our choice of one or the other in various situations.

SiPMs show important advantages compared to PMTs. Some of them are also very crucial for the tracking detector:

- SiPMs are a lot cheaper than PMTs.
- The V_{bias} for the used SiPMs lies at $\approx 70 V$ which is about an order of magnitude lower than the V_{bias} of the PMTs.
- With SiPMs it is possible to detect single photons. This is very important for the given detector since it has a rather low light yield between one and thirty photons per incident muon, see chapter 6. The minimal number of incident photons, needed to cause a signal in PMT, is dependent of the applied bias voltage. The lower this number should be, the higher V_{bias} must be. But with an increasing bias voltage also the noise rate increases, which limits the usage of such photo multipliers at low light yields
- In PMTs electrons fly from one dynode to another. Due to magnetic fields it is possible, that some of the electrons will not reach the next dynode. It is therefore very important to shield PMTs against B-fields. This effect does not occur for SiPMs. The drift region of electrons in a SiPM is roughly $6 \mu m$

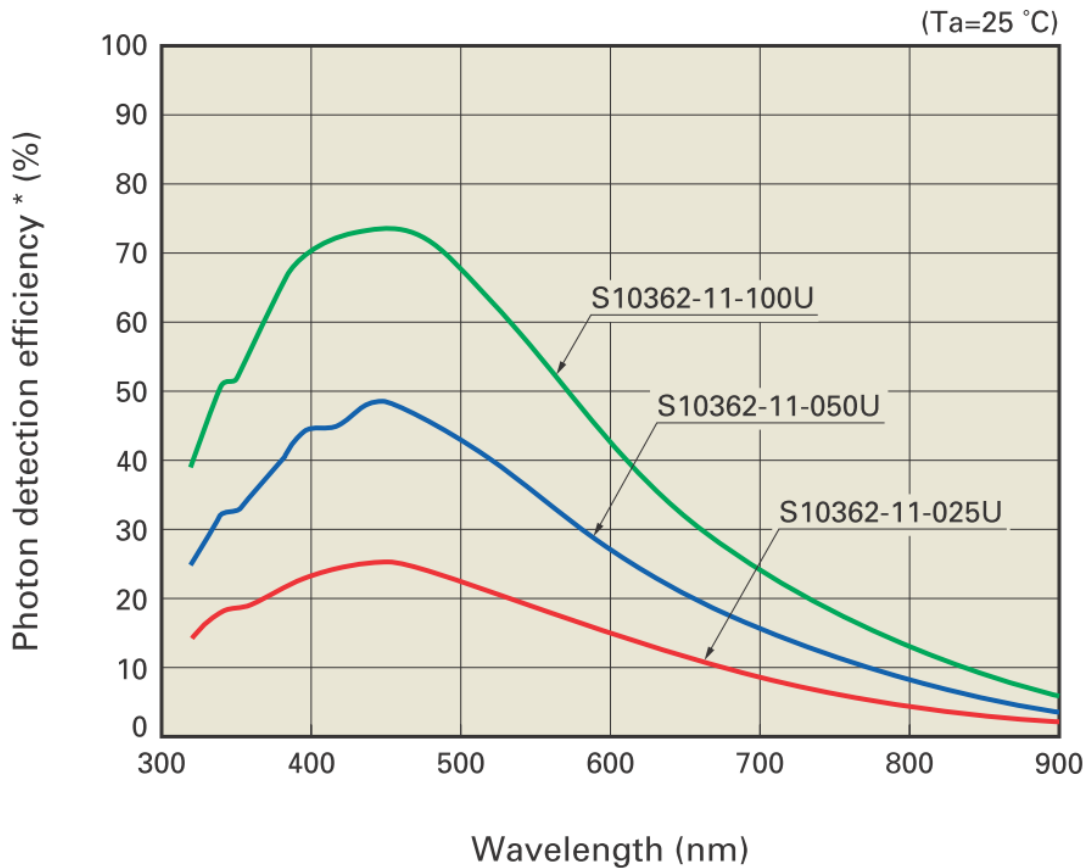


Figure 20: PDE for the three different pixel sizes of $100 \mu m$, $50 \mu m$ and $25 \mu m$ [Hamamatsu Electronics, 2008]. The "U" after the pixel size indicates, that the SiPM is covered in a metal case.

long. Compared to the distances from one dynode to the next in a PMT, this is about three orders of magnitude smaller. The short drift region makes SiPMs usable in presence of magnetic fields like in modern particle detectors.

- The timing resolution of SiPMs was shown to be below $150 ps$ [Gundacker et al., 2012]. As will be discussed in chapter 5 it is very important to have a good timing resolution to increase the position resolution in x -direction.

Beside this, SiPMs also have some drawbacks setting a limit to their usage. A detailed discussion on these features can be found in [Grossmann, 2012]. Here some of them are briefly mentioned:

- **Temperature behavior:** As mentioned earlier, V_{BD} increases with higher temperature. For a fixed value of V_{bias} the gain and thus the pulseheight will decrease with higher temperature. We saw, that we have to keep the temperature in a range of $\pm 0.25^\circ C$ around a certain operation temperature [Ruschke, 2014], that the change in pulseheight varies by only 10%. For the same type of a SiPM, i.e. the same pixel sizes, the temperature dependence is equal. This means, V_{BD} has to be determined for each SiPM at the same temperature⁹. After that, one operates at an arbitrary temperature adjusting V_{bias} , as long as the temperature is constant during the entire experiment [Grossmann, 2012].
- **Dark Current:** Even without incident photons, a SiPM can show photon like dark signals. This results due to two effects, the tunnel effect and thermal excitation. With a certain probability an electron can tunnel into the conduction band, even if its energy is too low, or it gets enough energy by a thermal excitation to reach the higher energy level. The rate, at which this happens is called dark count rate (DCR) and increases with increasing bias voltage, temperature and cell size. The DCR ranges from $10^5 Hz$ to $10^6 Hz$.
- **After Pulsing:** If a cell fires it sometimes happens, that single electrons of the avalanche are trapped in lattice defects. When they are released a new avalanche is triggered.
- **Crosstalk:** One cell of a SiPM emits about one to ten photons per avalanche due to recombination [Grossmann, 2012]. These photons can trigger avalanches in neighboring cells. The crosstalk probability (P_{cross}) is defined to be the ratio of the DCR with two or more simultaneous firing pixels, DCR_2 , to the total DCR, i.e. the one, for which at least one pixel has shown a signal, DCR_1 [Ramilli et al., 2010]:

$$P_{cross} = \frac{DCR_2}{DCR_1} \quad (3.3.1)$$

⁹In our case $20 \pm 0.1^\circ C$.

The crosstalk probabilities for $1 \times 1 \text{ mm}^2$ -SiPMs with the three different pixel sizes are given in figure 21. The higher crosstalk probability for the larger pixels sizes is an effect of the higher gain for these types [Hamamatsu Electronics, 2008].

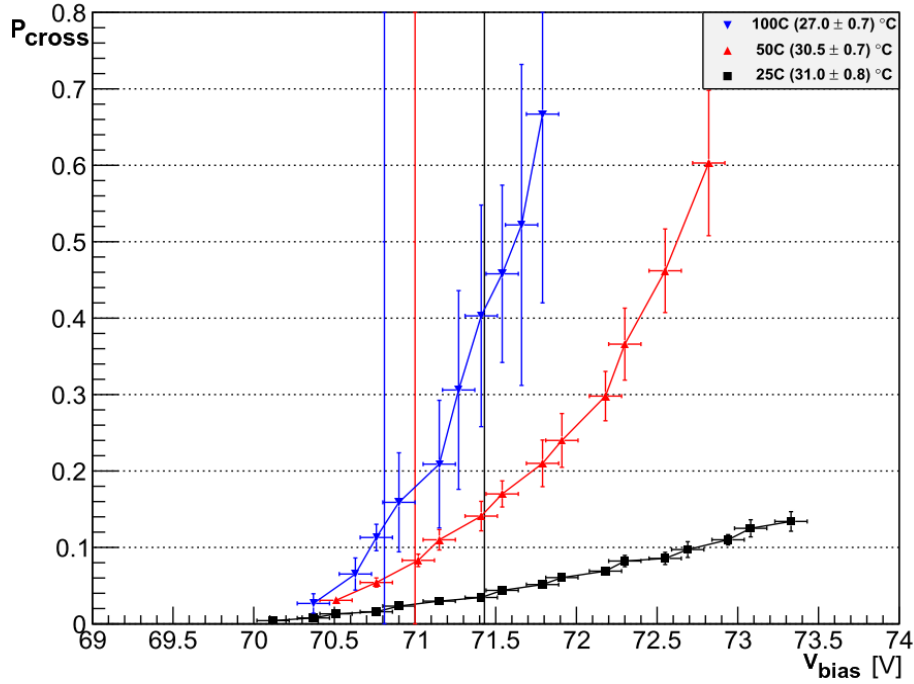


Figure 21: Crosstalk probabilities for the three pixel sizes depending on V_{bias} [Grossmann, 2012]. The three vertical lines indicate the recommended operating voltages for each type [Hamamatsu Electronics, 2008]

The DCR and the after pulses can be reduced by several methods.

The very first way to reduce the rate of fake events is, to apply a cut to the signal. The signals from background sources basically have the shape of one firing pixel. If we request at least two firing pixel, the rate of non photon induced signals drops by at least one order of magnitude [Grossmann, 2012]. This drop can be improved by applying even higher cuts which are matched to the minimal number of firing pixels in a real event. The light yield of the scintillator sets a limit to the cut, because we do not want to cut into the signal.

The second step to reduce this background requires more than one readout channel. In the case of two SiPMs mounted on the same scintillator, penetrating radiation results in a simultaneous signal in both devices. As an example, consider a DCR of 10^5 Hz for at least two firing pixels. Additionally let a signal from the second SiPM be called "coincident" to the signal of the first one, if it comes in an interval of 10 ns after the beginning of the first one. The probability for such an event is given by $10^5 \text{ Hz} \cdot 10 \text{ ns} = 10^{-3} = 0.1\%$. The simultaneous signal from penetrating radiation occurs in almost 100% of the cases. We can conclude, that a coincident signal in the readout channels of a single scintillator is almost always a result of a passing particle.

Crosstalk exists in real, as well as in fake events. To reduce the probability, one must reduce V_{bias} , but it still has to be above V_{BD} . We plan to use the SiPM with an over voltage of $1 - 2 \text{ V}$. According to figure 21, we expect a P_{cross} of $5 - 15\%$ in this range. The range for V_{over} is a compromise to maximize ϵ_{Geiger} and to minimize P_{cross} .

Due to the presented advantages SiPMs match very well with the conditions of the detector.

Due to the coupling of the scintillator to the WLSF and the coupling of the WLSF to the SiPM, see section 4.1, this case is more sophisticated than the simple gluing of the PMT. The PMTs are also much less temperature sensitive, but the measurements are also done in the climatic chambers.

4 Description of General Setup

The following sections describe basic parts of the light collection process, which are generally used in the experiments. As described in chapter 2, a scintillation detector contains always a device to convert the scintillation photons to a measurable electrical signal. For the performed measurements both types of photo multipliers described in chapter 3, are used. Measurements with SiPMs contain studies about position resolving properties of the detector, while the PMT readout is used to study the light output of trapezoidal shaped scintillators. The trapezoids are in both cases wrapped in a reflective material to prevent the photons from escaping the scintillator. The temperature for both setups is at least monitored or additionally stabilized with a cooling system.

The processing of the electrical signal from a photomultiplier was done with two different setups. The first one contains a flash analog-to-digital converter (FADC) and the second one contains a charge-to-digital converter (QDC). In the following section both photomultiplier as well as the readout electronics will be presented.

4.1 Photon Detection with SiPMs

The following readout setup of the scintillator is foreseen to be used in the final setup of the detector. The light of penetrating radiation propagates to a WLSF, in which the blue scintillation light is shifted to a green wavelength and is guided to SiPMs sitting at the edges of the fiber.

The fibers are glued into grooves in the scintillator with an optical cement, called BC 600 [Saint Gobain, 2011a], of the same refractive index as the BC 400 scintillator, $n_{BC400} = 1.58$ [Saint Gobain, 2005]. The WLSFs we use, are called BCF 92 with 1.0 mm and 1.5 mm diameter [Saint Gobain, 2011a]. The fiber has a core with a refractive index of $n_{core} = 1.60$ surrounded with an optical cladding with a refractive index of $n_{clad} = 1.49$ [Saint Gobain, 2011a].

By Snell's law

$$n_{core} \cdot \sin(\theta_{tot}) = n_{clad} \cdot \sin\left(\frac{\pi}{2}\right) \quad (4.1.1)$$

one obtains a total reflection angle of $\vartheta_{tot} = 68.63^\circ = 1.198 \text{ rad}$ for BCF 92.

Light entering the fiber is absorbed inside and emitted in a solid angle of 4π , see figure 22.

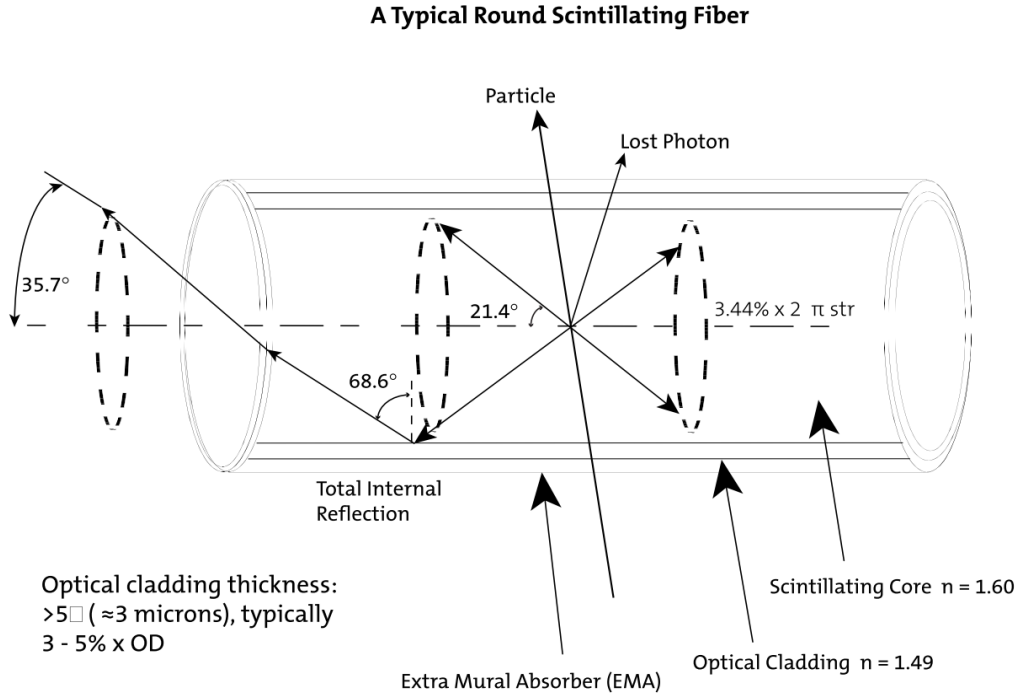


Figure 22: Scheme of a **WLSF** containing scintillating core, optical cladding and EMA [Saint Gobain, 2011a].

This step is needed to guide the light out of the detector to the **SiPM**, where it is detected. A wave guide like a **WLSF** has a higher refractive index than the surrounding material in order to guide the light via total reflection. Scintillation light from the detector always hits the fiber sideways with an entering angle smaller than 90° , which is refracted to an angle smaller than ϑ_{tot} . Consequently scintillation light can not be guided by a normal wave guide. To resolve this problem we use **WLSFs**, in which the light from the scintillator is shifted to a longer wavelength, which is in our case green. The emission of the green light happens in a solid angle of 4π and therefore a small fraction of this light fulfills the condition of total reflection and is guided to the **SiPM**. To be guided in the **WLSF**, the green light has to be emitted within a solid angle, which is obtained by the following integral:

$$2 \cdot \int_0^{2\pi} d\varphi \int_0^{\frac{\pi}{2} - \vartheta_{tot}} d\vartheta \sin \vartheta = 2 \cdot \int_0^{2\pi} d\varphi \int_0^{\frac{\pi}{2} - 1.198} d\vartheta \sin \vartheta = 0.8632 \quad (4.1.2)$$

4 DESCRIPTION OF GENERAL SETUP

The factor of 2 in front of the integral comes from the fact, that the light can be emitted in two directions with the same solid angle. If there is only one SiPM per fiber, one is only interested in an emission in one direction and the factor of 2 drops out. Dividing the result by the total solid angle of 4π shows, that only 6.9% of the total wavelength shifted light is guided to the SiPMs.

Each SiPM is mounted on an amplification board, as shown in figure 23. The amplification board consists mainly of a BGA-614 amplifier and the required connectors for readout and power supply [Ruschke, 2014].

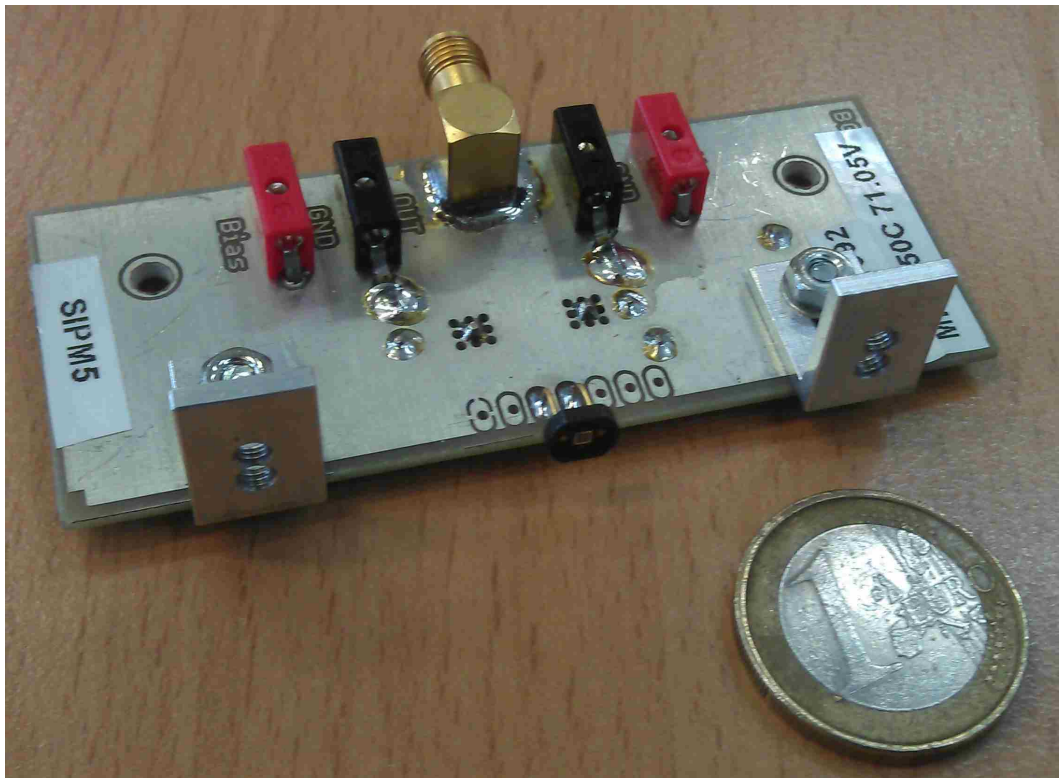


Figure 23: A $1 \times 1 \text{ mm}^2$ SiPM (small black piece close to the coin) mounted on an amplification board. There will be an aluminium plate mounted in front of the SiPM to connect it with an FC-connector to the WLSF.

We use FC-connectors, in which the end of a WLSF is glued, for coupling it to a SiPM. FC-connectors have the advantage, that they can be coupled and decoupled very fast and reproducibly, such that the fiber is always in the center of the SiPM and as near to it as possible. The connection of a fiber to an amplification board can be seen in figure 24.

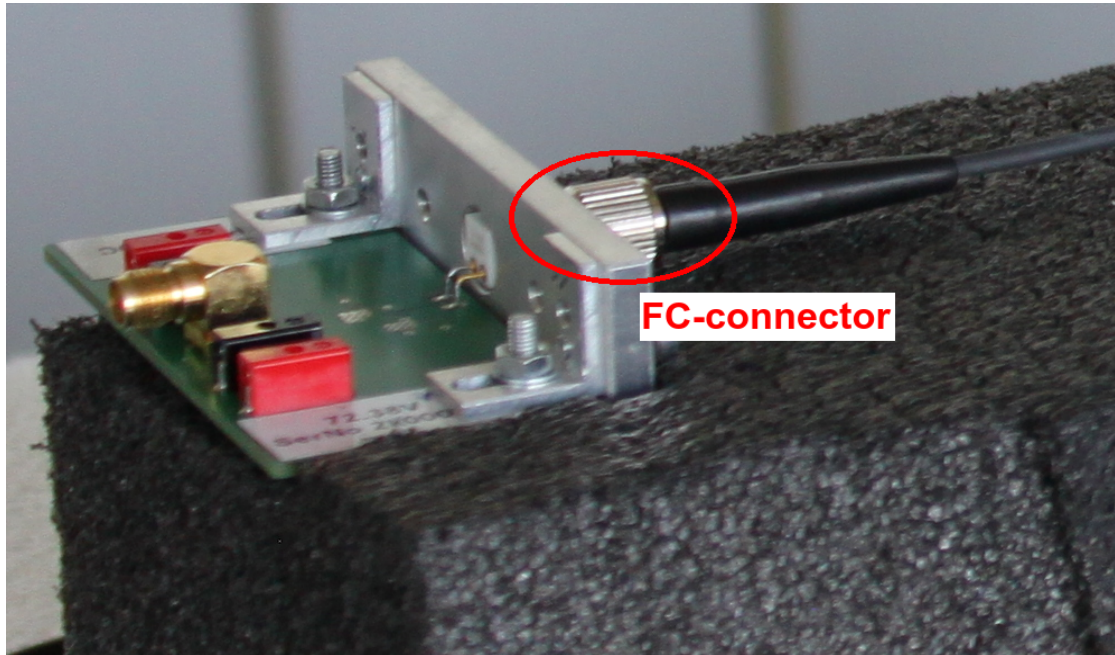


Figure 24: A $3 \times 3 \text{ mm}^2$ SiPM, this time in white, connected to a WLSF with a FC-connector.

4.2 Photon Detection with PMTs

The readout via PMTs is easier than with SiPMs. We glue the PMTs directly on the scintillator surface and supply them with a high voltage of the order of 750 V . The PMT can be removed again by putting the scintillator and the tube alternating in hot and cold water. The tube can after wards be re-glued at another position, making it possible to study the properties of a variety of different positions for the readout channels. If one uses the SiPM setup instead for such measurements, one would have to cut a groove in each position of interest.

4.3 Flash-ADC Readout

The used flash analog-to-digital converter (**FADC**)¹⁰ is a device, which samples the applied voltage signal in 2560 time steps with a frequency of either 1 GHz or 2 GHz . The time window in which the **FADC** can sample a signal is therefore $\approx 2.5\ \mu\text{s}$, respectively $\approx 1.25\ \mu\text{s}$ long. The dynamic range, in which the applied voltage can be measured, is -0.5 V to $+0.5\text{ V}$, which is covered by 4096 steps¹¹. The 0 V line is around 2048 **FADC** counts. An event recorded by a **FADC** can be seen in the following figure 25.

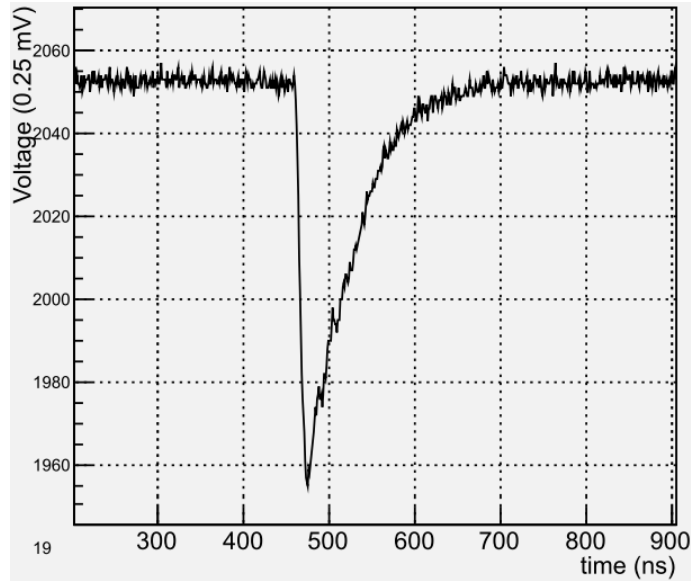


Figure 25: Measured **SiPM** signal with a **FADC**.

For this event the 1 GHz mode is used, such that the range on the x -axis goes from 0 to 2560 ns . To see details of the **SiPM** signal shape, we have to zoom in to a region from 250 ns to 900 ns . The signal of a photon detector is a voltage drop with a successive recharge of the device. An analysis tool extracts the starting point and the minimum of the signal, which both are used for the position determination. Actually the analysis tool converts the minimum of the signal to the absolute value of its difference from the 0 V line. The minimum of the signal is therefore also known as the maximum of the voltage drop.

¹⁰CAEN V1729 [CAEN, 2011a]

¹¹I.e. 12 bit resolution.

A schematic diagram for the [FADC](#) readout can be seen in figure 26.

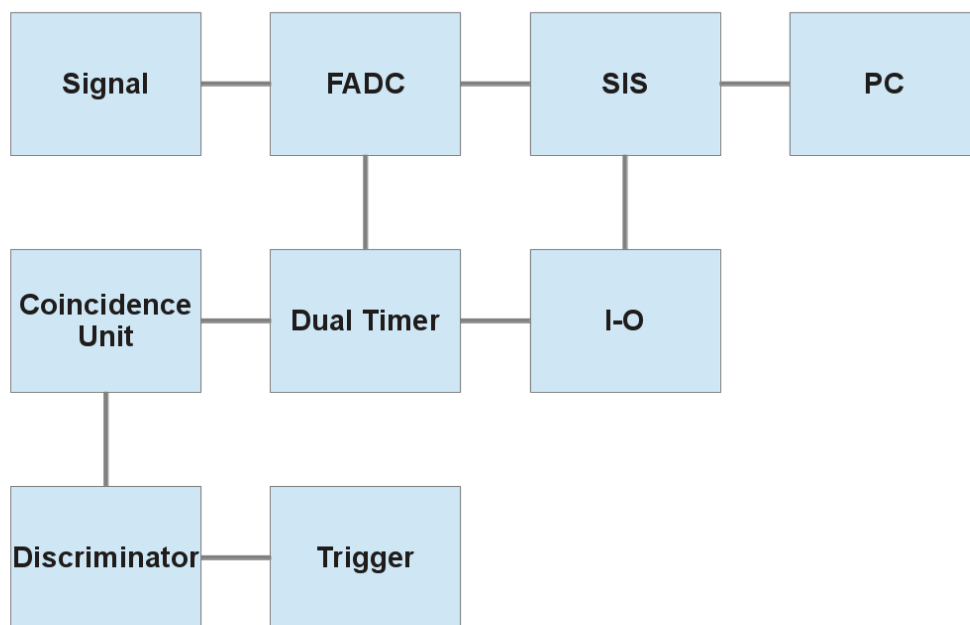


Figure 26: Schematic draft of the readout system containing a [FADC](#)

The signal from a trigger¹² goes at first through a discriminator and a coincidence unit. The discriminator responds with a digital signal, if the trigger signal has a pulseheight over an adjusted threshold. In most cases there are at least two trigger signals, which are time-compared in a coincidence unit. The coincidence unit has two modes. In the "or" mode, this unit gives an output signal if at least one of the input channels gave a signal. In the "and" mode, the unit checks, whether all input channels are high at the same time. This happens in nearly all cases only if one particle has passed all triggers in a row, similar to the example in section 3.3, in which we use more than one [SiPM](#) to reduce events caused by dark current. The signal from the coincidence unit goes to the dual timer. This device starts the data acquisition and blocks further trigger signals until it gets reset.

¹²For example two scintillators define a solid angle. Only particles coming within this solid angle cause triggers.

The **FADC** continuously samples the applied voltage at its input channels and stores this data in a ring memory meaning, that it continuously overwrite the old data in its memory. When getting a signal from the dual timer the **FADC** reads the stored data of the passed $2.5 \mu s$ respectively $1.25 \mu s$, depending on the sample frequency.

The data is send to the PC via the SIS¹³. The SIS is a VME controller connected to the PC via an optical fiber and acts as an interface between the PC and the readout electronics. The PC stores the data in a file. After wards the I-O register gets a command to send a reset to the dual timer finishing the data busy signal.

The **FADC** readout system can process a trigger rate of up to $250 Hz$. If the rate is higher, the system will miss some of the events.

With an **FADC** one can extract the two parameters mostly interesting for position determination: the time of the rising edge and the maximum pulseheight of the signal.

¹³VME controller

4.4 QDC Readout

With a charge-to-digital converter (QDC)¹⁴ alone, one can only get an equivalent quantity to the pulseheight of the signal, as measured with a FADC. In all measurements in this work, which contain a QDC readout system, we are interested only in this information and not in the timing information.

A QDC integrates the charge applied to its entrance over an adjustable time window, called gate. The plugging diagram for this system can be seen in figure 27.

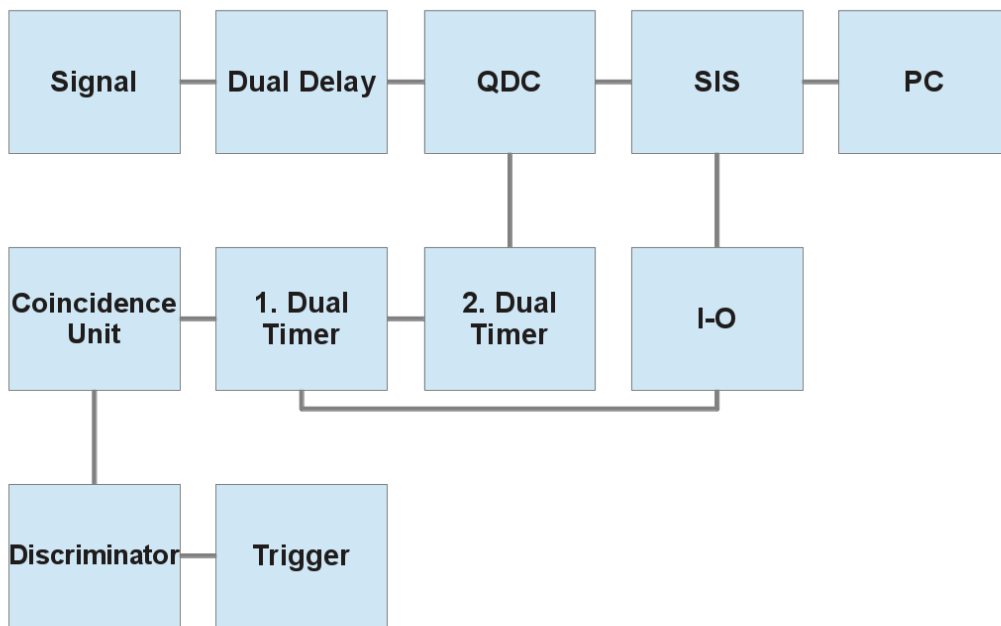


Figure 27: Schematic draft of a QDC readout system.

The steps from the trigger to the first dual timer are exactly the same as in section 4.3. The dual timer passes the trigger to a second dual timer and blocks further triggers until it gets a reset from the I-O register. The second dual timer produces a digital NIM pulse with the start point given by the first dual timer. This NIM pulse is given to the QDC and defines its gate. The length of the gate is adjusted

¹⁴We use the model CAEN V792N.

by the length of the **NIM** pulse, which can be done at the second dual timer. The total process up to this point needs a certain amount of time. In contrast to the **FADC**, the **QDC** reads the signal at its input channels only during a gate pulse. To produce this gate pulse the electronics need some time and the signal must be delayed with a dual delay unit to ensure that it lays totally within the gate. This delay has to be adjusted once before the measurement using an oscilloscope. For this, one plugs the cable coming from the dual delay to one of the channels of an oscilloscope. The output of the second dual timer is connected to another channel. A picture of the oscilloscope display can be seen in figure 28.

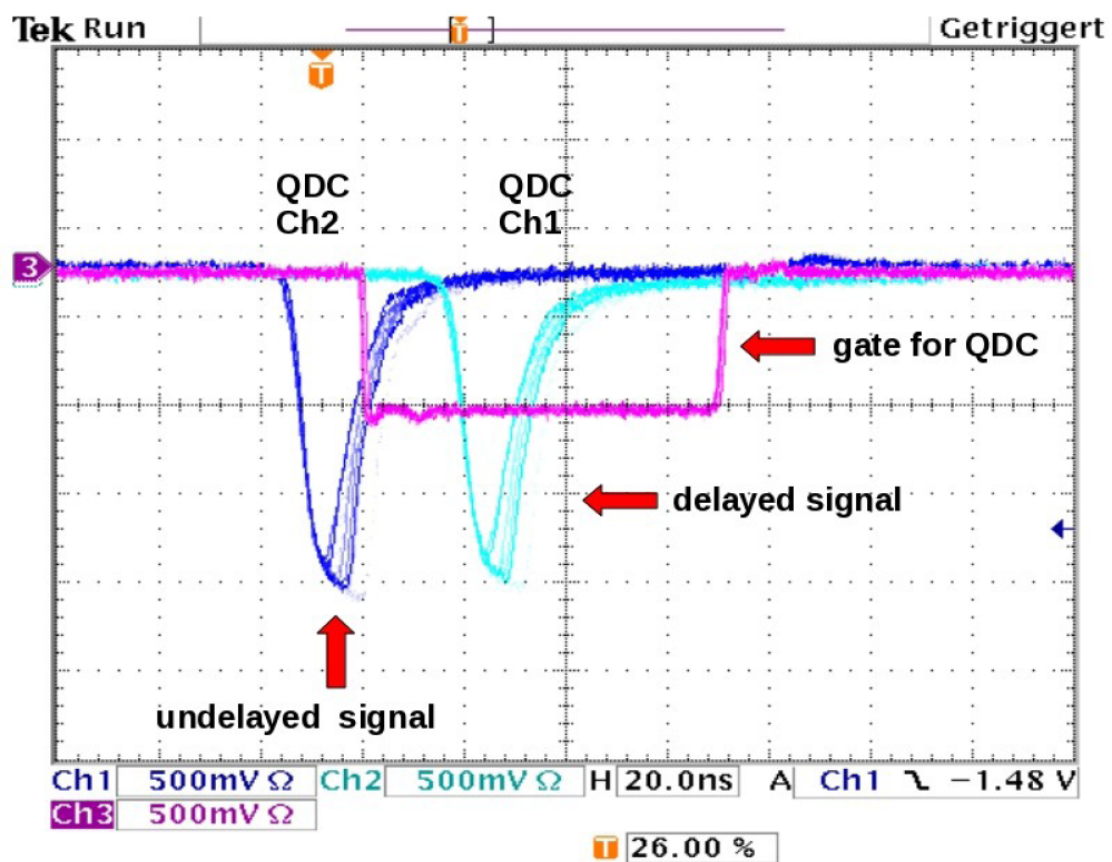


Figure 28: Oscilloscope displaying the undelayed signal, the delayed signal and the gate of the second dual timer [Ruschke, 2010].

The integrated charge is converted into a digital signal and passed to the SIS. The following processes are again equal to the **FADC** case. Besides the missing timing information, the **QDC** has two advantages in comparison to the **FADC**:

- The event rate at which the QDC can process triggers is $\approx 1\text{ kHz}$, so it can handle roughly a factor of four more events in the same time than the FADC.
- While the FADC gives 2560 data points for each event and each channel, the QDC gives only a single number per event and channel. The file size is therefore a lot smaller.

The QDC has a better performance when the rate of the penetrating radiation is higher. To get an additional time information, one has to use a second device in addition to the QDC like a time-to-digital converter (TDC) or a FADC.

During a beam time at CERN, where we test a first prototype, we use the FADC since it allows us to obtain the pulseheight as well as a time information with just one device.

The next chapter will describe the proceeding of track reconstructing out of the measured data.

5 Basic Idea of the Detector

The Cosmic Ray Facility (CRF), located in Garching, will be used for testing and commissioning large area *Micromegas* detectors with cosmic muons. This detector will be used to improve the energy selector of the CRF. The basic idea of this detector is, to obtain a position resolution due to the geometrical shape of two trapezoidal scintillators. A muon will first pass the reference chambers, and is then scattered within an iron absorber. This detector reconstructs the muon position behind the absorber and compares it to the predicted position of the reference chambers. With this information, we can reconstruct the energy of the muon.

Important for the track reconstruction is the amount of photons produced by a penetrating muon. The light production of muons depends, among other properties, on the path length in the scintillator¹⁵. In general the longer the path of a particle through the scintillator, the more scintillation light is produced. A schematic sketch of a detector is shown in figure 29.

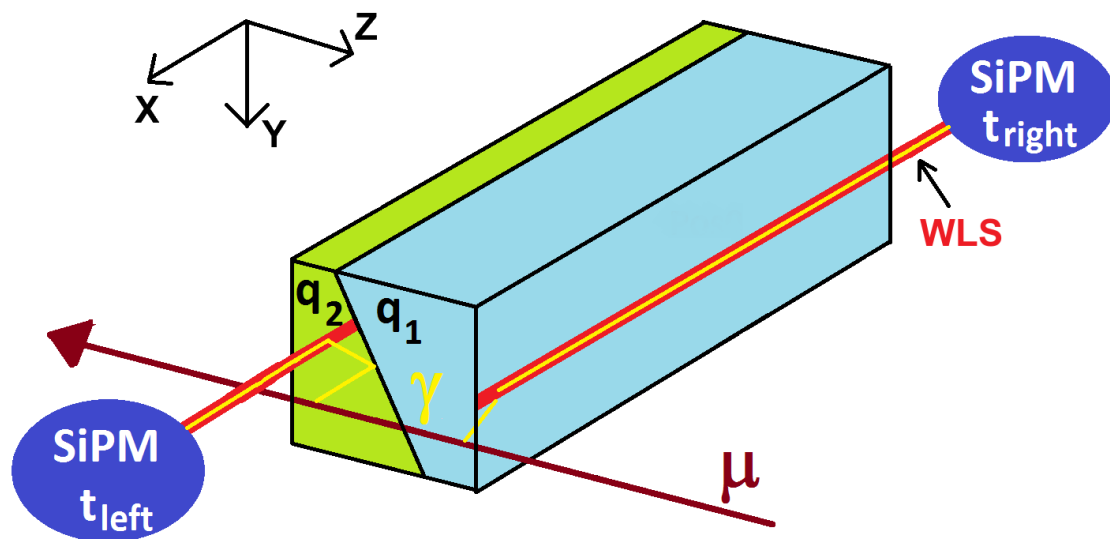


Figure 29: Schematic draft of the detector. Note that the colors are just for visualization of the principle.

¹⁵Other properties are for example particle energy, particle type, Landau distributed energy loss, etc.

One module of the detector consists out of two optically insulated trapezoidal scintillators. A muon passing the detector produces an amount of light q_1 proportional to the path length in the first half of the module (blue) and an amount q_2 proportional to the path length in the second half (green) of the module. The light (yellow) propagates in the scintillator, is collected in the **WLSF** (red) and then guided to a **SiPM** for photon detection.

In figure 29 each fiber has only one **SiPM**, but a double sided readout is foreseen to enhance the light yield.

In the following we use the coordinate system as sketched in figure 29 to label the axes of the detector. By comparing the arrival time of the signal on each side of the **WLSF**, or the pulseheight of the signal from each half of the scintillator, one can achieve a two dimensional spatial resolution. This chapter describes how the conversion of a light yield or a timing information to a spatial coordinate works and which position resolution is required for a cut to a certain energy of muons.

5.1 Position Resolution in x -Coordinate

From the point where the scintillation light is created, the photons need a certain time t_L to travel to the left readout system and another time t_R for the path to the right. Out of this timing information one can obtain the x -coordinate of the point where the particle has passed the detector. We want to present three methods here, how this can be done.

1. The sum of both times, t_{max} is a constant, proportional to the length of the scintillator X_{scin}

$$t_L + t_R = t_{max} = \frac{X_{scin}}{c_{BC400}} = \frac{X_{scin} \cdot n_{BC400}}{c} \quad (5.1.1)$$

with the speed of light in the scintillation material $c_{BC400} = \frac{c}{n_{BC400}}$. With the timing information one can now calculate the x -coordinate of the muon according to:

$$x = X_{scin} \cdot \frac{t_L}{t_{max}} = X_{scin} \cdot \left(1 - \frac{t_R}{t_{max}}\right) \quad (5.1.2)$$

The $x = 0$ position is defined to be on the left end of the scintillator rod, when looking in the flight direction of the muons.

2. The fraction of the difference in time and the sum of the times is also position dependent:

$$\frac{t_L - t_R}{t_L + t_R}$$

If the particle passes the detector on the left end of the scintillator rod, t_L will be zero and this ratio will be -1 . Similarly it will be zero in the middle and $+1$ on the right edge of the module. By multiplying this fraction by the half of the scintillators' length, one gets the x -coordinate of the particle, but this time the zero point will be in the middle of the detector:

$$x = \frac{X_{scin}}{2} \cdot \frac{t_L - t_R}{t_{max}} \quad (5.1.3)$$

3. In the last method one converts the difference of both times into a difference in length by multiplying it by the speed of light in the scintillator. Since the refractive index of **WLSF** and scintillator are almost equal, $n_{scin} = 1.58$, $n_{WLSF} = 1.60$, there is nearly no difference for the calculation of the x coordinate.

$$x = (t_L - t_R) \cdot \frac{c}{n} \quad (5.1.4)$$

This equation is not yet complete. The middle position of the detector is, like for method 2, the origin of the x -coordinate. The range of the scintillator goes from $-\frac{1}{2} \cdot X_{scin}$ to $+\frac{1}{2} \cdot X_{scin}$, but in equation 5.1.4 it would go from $-X_{scin}$ to $+X_{scin}$. Therefore a factor of $\frac{1}{2}$ solves this problem:

$$x = \frac{1}{2} \cdot (t_L - t_R) \cdot \frac{c}{n} \quad (5.1.5)$$

From a mathematical point of view all three methods are equivalent. The mid of the scintillator is shifted from $x_{mid} = \frac{1}{2}X_{scin}$ in equation 5.1.2 to $x_{mid} = 0$ in equation 5.1.3 and substituting $X_{scin} = \frac{c}{n} \cdot t_{max}$ in equation 5.1.3 results in equation 5.1.5 and vice versa. But from an experimental point of view method three should provide the best results, since one performs less operations with the measured values. Additionally any constant time offset cancels out in a difference $t_L - t_R$ but it gets doubled in a sum $t_L + t_R$.

We will use all three methods in section 6.1 to compare their results and to find the best one to get an optimal position resolution.

5.2 Position Resolution in y -Coordinate

The y -coordinate is slightly more difficult to obtain, than the x -coordinate. We have to compare the light yields of the two scintillator halves. The variables of the following calculations are given in figure 30.

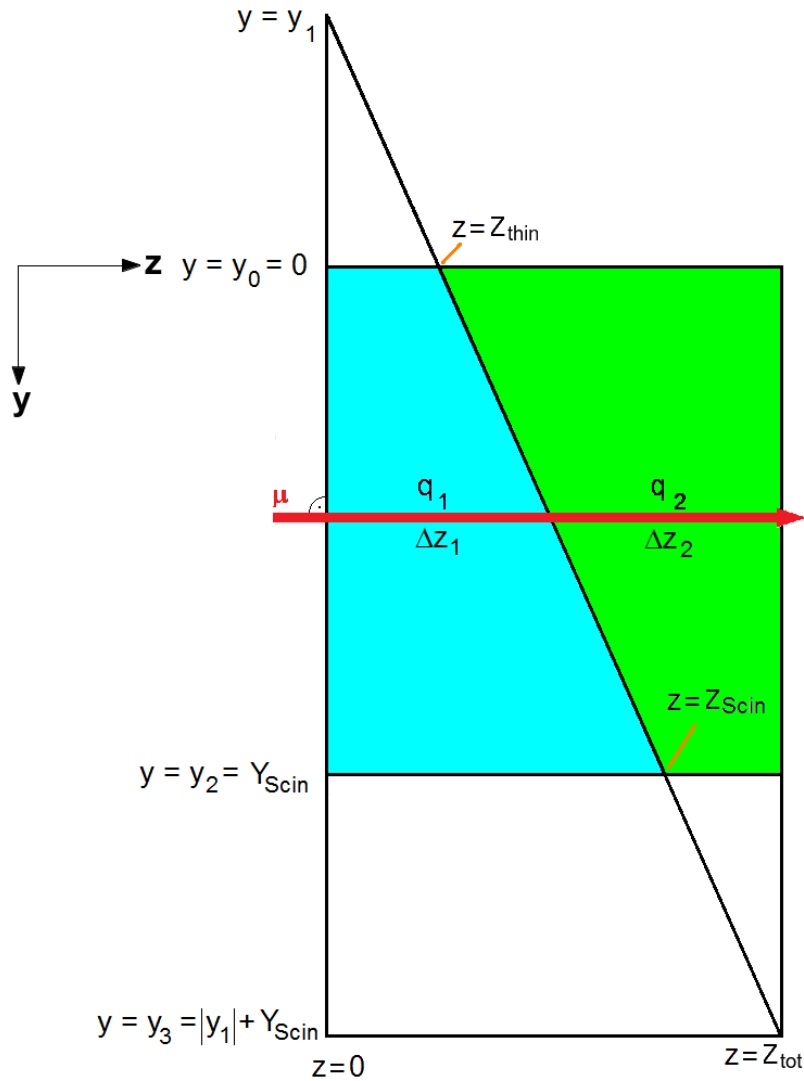


Figure 30: Definition of the parameters for y -coordinate calculation.

In y -direction the detector ranges from $y = y_0 = 0$ to $y = y_2 = Y_{scin}$. By extrapolating the separation line of the two scintillators, one arrives at $y = y_1$ and symmetrically to $y = y_3 = |y_1| + Y_{scin}$.

Each module has a thin and a broad side in z -direction. The length on the thin and broad side are given by Z_{thin} and Z_{scin} , respectively. In this thesis we concentrate on particles passing perpendicular to the $x - y$ plane through the scintillator. The path lengths in the scintillators are given by Δz_1 and Δz_2 . The light yields in both scintillators are proportional to their path lengths with a proportionality factor w , which depends on the particle energy, the mean energy it takes to create a photon and the Landau distributed energy loss as described in section 2.4. The first two dependencies are equal for both scintillators, the last one is not. In order to get the idea behind the position determination, we assume, that the dependency on the energy loss is eliminated. In this case the sum of both light yields is constant:

$$q_{max} = q_1 + q_2 = Z_{tot} \cdot w \quad (5.2.1)$$

For the later calculation we need an expression for y_1 . To obtain this we use the intercept theorem:

$$\frac{|y_1|}{Z_{thin}} = \frac{|y_1| + Y_{scin}}{Z_{scin}} \quad (5.2.2)$$

Solving this for $|y_1|$, one gets

$$|y_1| = Y_{scin} \cdot \frac{Z_{thin}}{Z_{scin} - Z_{thin}} \quad (5.2.3)$$

Investigating another intercept theorem, one gets an equation for the y coordinate.

$$\frac{|y_1| + y}{q_1} = \frac{2 \cdot |y_1| + Y_{scin}}{q_1 + q_2} \quad (5.2.4)$$

Inserting $|y_1|$ from equation 5.2.3 and solving for y finally results in:

$$y = \frac{Y_{scin}}{Z_{scin} - Z_{thin}} \cdot \left(\frac{q_1}{q_1 + q_2} \cdot Z_{tot} - Z_{thin} \right) \quad (5.2.5)$$

With q_1 and q_2 being the measured quantities. In the case of an **FADC** readout q_i are defined to be the pulseheight of the signal and for the **QDC** system the q_i are defined as the integrated charge. The pulseheight suffices because it is proportional to the integrated charge due to the known and fixed light emission curve for a particle species of the scintillator, confer equation 2.1.2.

5.3 Multiple Coulomb Scattering

As mentioned in chapter 1, the detector will be used as an energy selector in the CRF. A muon passing the active detector parts of the CRF will also traverse an 34 cm thick iron absorber. In this the muon will be deflected by many small angle scatterers due to Coulomb scattering at the iron nuclei, hence the name *multiple Coulomb scattering*. According to [Biebel et al., 2003] only muons with an energy larger than 600 MeV pass the iron absorber, which sets a preselection to the energy.

For particles passing the iron absorber the distribution of the scattered angle follows a Molière distribution, which is Gaussian like for small deflection angles [PDG, 2012]. Such particles will hit our detector at a different position as claimed by the reference chambers in the CRF. Our detector will be roughly 1 m below the iron absorber as shown in figure 31.

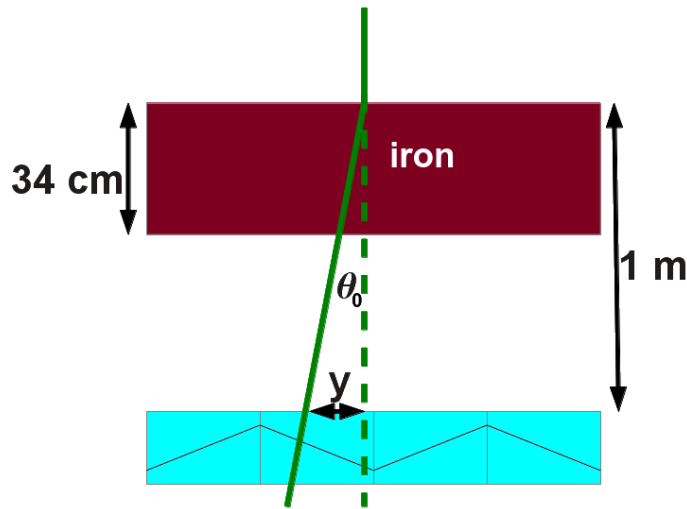


Figure 31: Schematic sketch of the energy selector in the CRF. Due to multiple Coulomb scattering the original track of the muon will be deflected on average by an angle θ_0 . The dashed line represents the track of the muon predicted by the reference chambers.

A fit to the Molière distribution gives us the mean deflection angle:

$$\theta_0 = \frac{13.6 \text{ MeV}}{\beta \cdot c \cdot p} z \sqrt{\frac{x}{X_0}} \left[1 + 0.038 \log \left(\frac{x}{X_0} \right) \right] \quad (5.3.1)$$

With $\beta \cdot c$, p and $z = \pm 1$ are the velocity, momentum and charge number of the muon and $\frac{x}{X_0}$ is the thickness of the iron absorber in units of radiation lengths [PDG, 2012]. The radiation length for iron is $X_0 = 1.76 \text{ cm}$ and equation 5.3.1 can be simplified:

$$\theta_0 = \frac{62.7 \text{ MeV}}{\beta \cdot c \cdot p} \quad (5.3.2)$$

which is only dependent on particle properties. We neglected the sign of the charge number due to symmetry reasons.

To further simplify equation 5.3.5 we assume, that the energy of the muon is much larger than its mass and that it therefore travels roughly at the speed of light, hence:

$$\begin{aligned} \beta &= c = 1 \\ p &= \sqrt{E^2 - m^2} \approx E \end{aligned} \quad (5.3.3)$$

Inserting relations 5.3.3 into equation 5.3.5 yields:

$$\theta_0 = \frac{62.7 \text{ MeV}}{E} \quad (5.3.4)$$

With this length and the mean deflection angle we can calculate the position in the detector

$$y = 1 \text{ m} \cdot \tan(\theta_0) = 1 \text{ m} \cdot \tan\left(\frac{62.7 \text{ MeV}}{E}\right) \approx \frac{62.7 \text{ MeV}}{E} \text{ m} \quad (5.3.5)$$

Where we use a small angle approximation in the last step. Table 1 lists track Gaussian width of scatter in the detector for eight muon energies.

$E_\mu \text{ [GeV]}$	< 1	1	2	3	4	5	6	> 6
$y \text{ [cm]}$	> 10	6	3	2	2	1	1	< 1

Table 1: Gaussian width of scatter for eight muon energies.

The next chapter deals with achieved position resolution in both dimensions with a prototype detector tested at CERN. It turns out, that the position resolution in y direction, calculated by pulseheight information, is better than in x direction, obtained from the propagation time information. Therefore we have two different energy resolution depending on the direction of the deflection.

6 Test of a Prototype Detector at CERN

During a beam time at [CERN](#) we have the opportunity to test a first prototype of the trapezoidal scintillating detector in a pion beam with high statistics in a short period of time. The beam time took place from October, 18th until November, 2nd 2012 at the H6 beam line.

The accelerator facility at [CERN](#) consists of a chain of pre-accelerators, which finally fill the Large Hadron Collider ([LHC](#)). One of them is the Super Proton Synchrotron ([SPS](#)), which is the last accelerator before the [LHC](#). Besides filling the [LHC](#), this accelerator also serves other experiments in a cycle, which lasts for ≈ 60 s. For roughly 10 s the [SPS](#) proton beam is targeted on the primary target T4. In the target station T4 the components of the secondary beam resulting from the collision of protons with the target material are selected regarding their momentum by a magnetic field. The beam is divided in different particle beams. One part is guided to the H6 beam line located in the [CERN-North-Area](#) in Prévessin. Our beam consisted of pions with a rate of roughly $40 \frac{kHz}{cm^2}$ and an energy of 120 GeV, which can be treated as [MIPs](#).

Our setup is shown in figure 32.

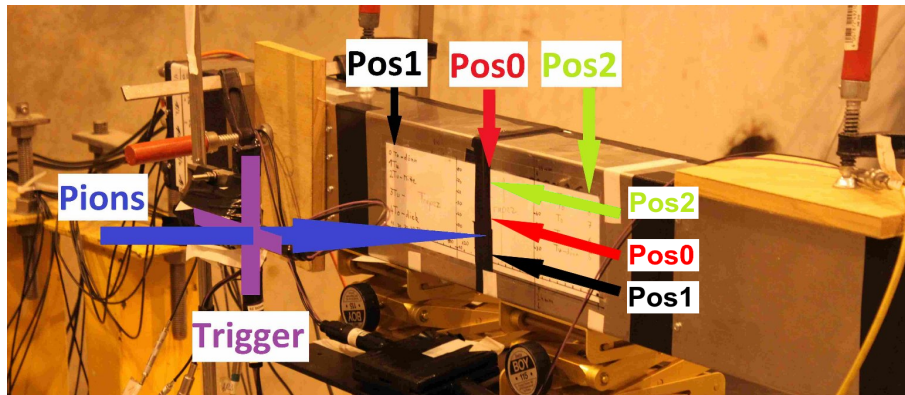


Figure 32: Setup in the H6 beam line at [CERN](#). The six displayed positions will be explained in more detail in section 6.1 and 6.2.

The pion beam passes the trigger from the left. This trigger consists out of two thin scintillators forming a cross with a $5 \times 5 \text{ mm}^2$ overlapping area. If there is a coincident signal in both trigger scintillators, a trigger is generated and the [SiPMs](#) are read out with the [FADC](#) system, for details see section 4.3. Since the beam is

perpendicular to the detector, it is not necessary to have one trigger in front and one behind the detector in order to select only perpendicular pion tracks. The pion will then go through the light tight box in which the two trapezoids are embedded. The white area on the box in figure 32 represents the active area of the detector. By moving the box vertically and/or horizontally, the position resolution of the detector in two dimensions can be tested.

Each half of the scintillator has five WLSFs of 1 mm diameter with one SiPM¹⁶ each for readout. The dimensions of the trapezoids and the position of the WLSFs with respect to the beam position can be seen in figure 33.

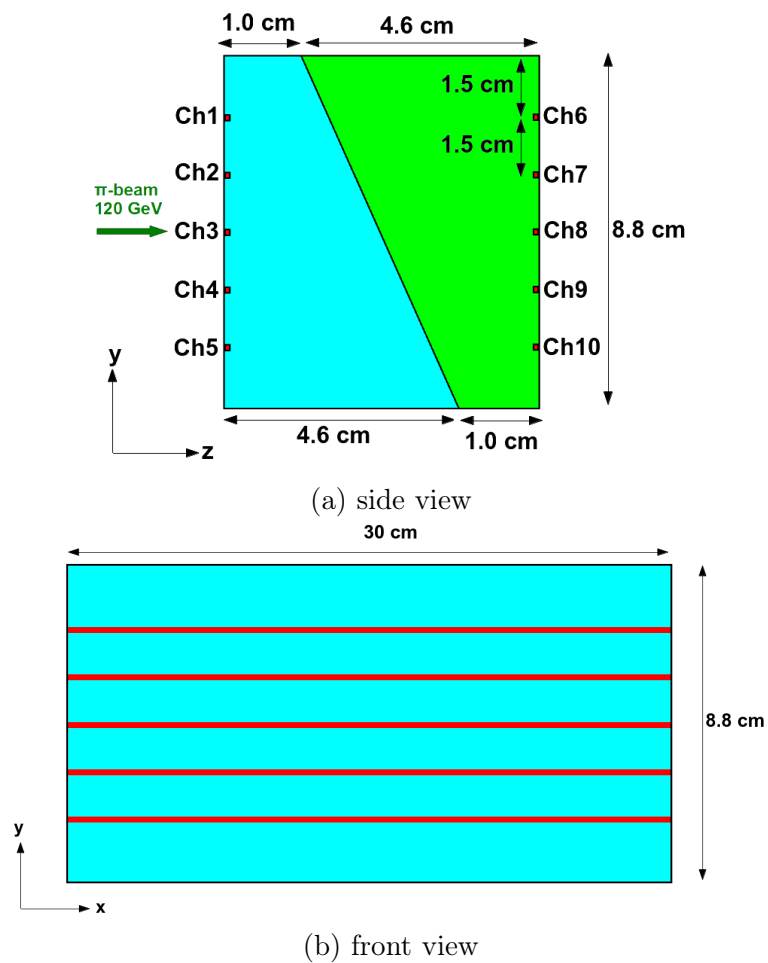


Figure 33: WLSF positions and dimensions of first prototype. Each groove (red) has a width of 1.5 mm.

¹⁶50C with an active area of $1 \times 1 \text{ mm}^2$

We start the experiments with the 1 GHz mode but switch to the 2 GHz mode to have a better timing resolution.

The two trapezoids are wrapped in aluminium to reflect the escaping photons back into the scintillator. The following sections will describe the procedure and results of the measurement for spatial resolution in two dimensions.

6.1 Timing Information: The x -Direction

Here we will present the procedure and the results for the timing analysis based on the 2 GHz data with $V_{bias} = 75\text{ V}$. The main task is, to determine the value of the starting point for a photon event in a SiPM.

We start with an approximation of how good this analysis can be at best. As mentioned in chapter 4.3, in the 2 GHz mode the FADC samples a time window of $1.25\text{ }\mu\text{s}$ in roughly 2500 steps. This means, that the difference between two steps of a sample is $\approx 0.5\text{ ns}$ corresponding to a length of

$$x = t \cdot \frac{c}{n_{BC400}} \approx 0.5\text{ ns} \cdot \frac{c}{1.58} \approx 10\text{ cm} \quad (6.1.1)$$

Since our detector has a length of only 30 cm in x -direction we only test three beam positions, shown in figure 32:

- Position 0 (Pos 0): Beam is in the middle of the detector.
- Position 1 (Pos 1): Beam is 12 cm left of Pos 0.
- Position 2 (Pos 2): Beam is 11 cm right of Pos 0.

The asymmetry between Pos 1 and Pos 2 results from given mechanical conditions of the mounting of the light right box.

From equation 6.1.1 one can also see, that determine the starting point just 4 steps (out of 2500) wrong, results in a position, which can not be within the detector.

We will now present three methods, which we use, to determine the starting point of the signal:

- In the first method one determines the first time bin, when the signal is below a certain threshold value. The threshold should separate the baseline noise from an event, but in order to improve the resolution, the threshold

must be as close to the baseline as possible. For the given setup we calculate a baseline of 2049 ± 4 FADC-channels and conclude, that a value below 2042 FADC-channels corresponds to a signal. This time bin is then used as the starting point of the signal and the method is called "First-Point-Below-Threshold"-method (FPBT).

- Alternatively the rise of the signal can be fitted by a Fermi function:

$$f(x) = (d - a) + \frac{a}{1 + \exp\left(\frac{x-b}{c}\right)} \quad (6.1.2)$$

A fitted event is shown in figure 34.

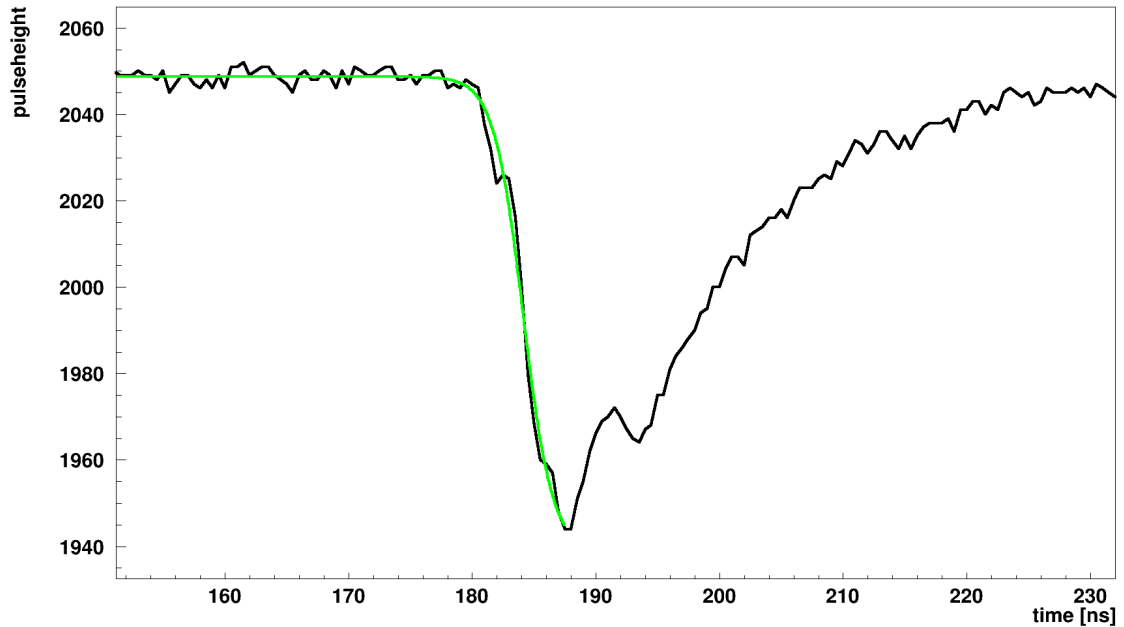


Figure 34: SiPM signal (black) fitted with a Fermi function (green) to the rise of the signal.

This function has four parameters: d is the height of the baseline, a is the pulseheight of the signal, b is the abscissa of the turning point of the function and c defines the gradient of the function. We use the parameter b , to define a point in time, when the signal arrives and call the method "Fermi function"-method (FFunc).

- For the last method we use a section wise defined function with five parameters.

$$f(x) = \begin{cases} c & ; x < a \\ -\frac{d}{b-a} \cdot (x - a) & ; a \leq x < b \\ c - d \cdot \exp\left(-\frac{x-b}{e}\right) & ; b \leq x \end{cases} \quad (6.1.3)$$

A fitted event is shown in figure 35.

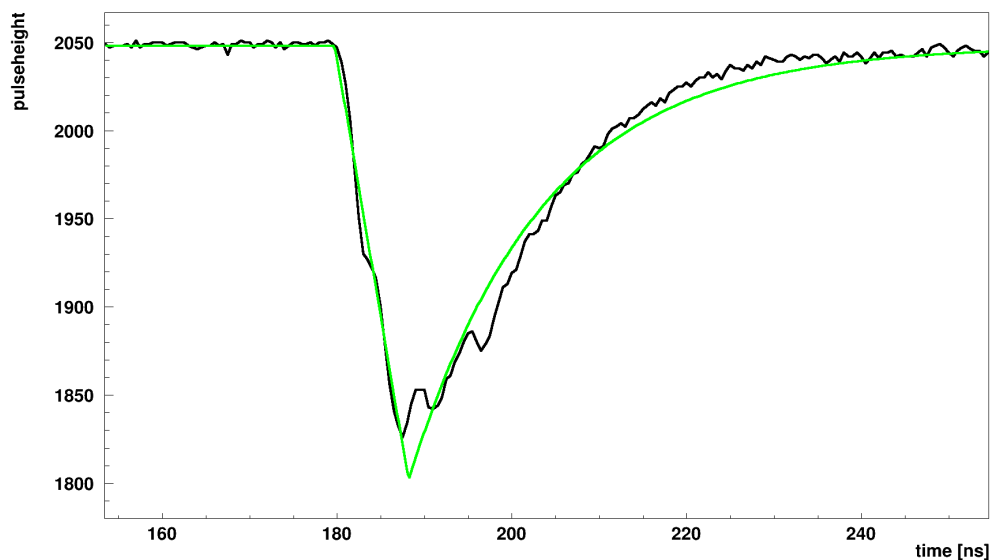


Figure 35: SiPM signal (black) fitted with a section wise defined function (green) describing the whole signal.

The first part of the signal is the baseline of the FADC and is described with a polynomial of degree zero by the parameter c . The rise of the signal is here described by a linear function from the starting point of the signal a to the maximum pulseheight of the signal b . After the signal reached its maximum, we consider the SiPM as a capacitor which is recharged over a resistor with a time constant e . Finally the parameter d represents the pulseheight of the signal. As the timing information we take the starting point of the signal a . This method is called "section-wise defined function"-method (SWFunc).

From pictures 34 and 35 one can see, that the starting point of the signal is always around 180 ns. This means, that the signal has a constant offset to the trigger signal and is situated always on the same position in the FADC time window.

For the further analysis the offset has to be subtracted, such that one remains with the true time it takes the light to the readout. If we take for example the [Pos 1](#) data, the time for the light to travel to the left [SiPMs](#) should be zero and therefore the measured mean for the time value can be interpreted as the offset. We fit a Gaussian function to the distribution of the timing values for all channels and subtract the means of this function in the further analysis from each timing value. The results are listed in [table 2](#).

	FPBT	FFunc	SWFunc
$t_{L,Ch1}$ [ns]	179.3 ± 2.0	183.1 ± 2.1	178.9 ± 2.0
$t_{L,Ch2}$ [ns]	179.4 ± 2.0	182.8 ± 2.0	179.1 ± 2.0
$t_{L,Ch3}$ [ns]	179.0 ± 2.0	182.4 ± 2.0	178.9 ± 2.0
$t_{L,Ch4}$ [ns]	179.2 ± 2.0	182.5 ± 2.1	179.0 ± 2.1
$t_{L,Ch5}$ [ns]	180.4 ± 2.1	183.9 ± 2.0	179.8 ± 2.0
$t_{R,Ch6}$ [ns]	180.8 ± 2.0	184.3 ± 2.0	179.8 ± 2.0
$t_{R,Ch7}$ [ns]	181.3 ± 2.1	184.1 ± 2.2	180.4 ± 2.3
$t_{R,Ch8}$ [ns]	181.7 ± 2.2	185.2 ± 2.2	180.6 ± 2.4
$t_{R,Ch9}$ [ns]	178.7 ± 2.0	181.7 ± 2.1	178.4 ± 2.1
$t_{R,Ch10}$ [ns]	177.2 ± 2.0	180.9 ± 2.1	177.3 ± 2.2

Table 2: Values for the offset for each channel and each method. Note that the zero point of the time value for channels 6 to 10 are for a beam at [Pos 2](#), hence the subscript R .

For the analysis we compare always a left and a right channel with the same position in y direction, see [figure 33](#). For each such pair of readout channels we only analyze events in which both have a pulseheight higher than 30 [FADC](#)-channels to sort out spontaneous thermal events. After this cut, the detector has an efficiency of roughly 15% coming from the fact, that the whole setup has a rather low light output, see [section 6.2](#). In next step we look for two channels, which are located at opposite sides of the detector and both have a high light output. The whole system has in total twelve readout channels, ten signal and two trigger, but one [FADC](#) has only four input channels. We therefore use three [FADCs](#) of the same type. It turns out, that, if the two channels for the different sides are connected to different [FADCs](#), there is a time offset between both devices, which varies for each event in the order of a few nanoseconds, being in the same region as our time differences ($t_L - t_R$) due to different light propagation times.

The only combination of SiPMs which is on the same FADC is Ch5-Ch10. Figure 36 shows the run time difference for Ch1-Ch6 and Ch5-Ch10 respectively.

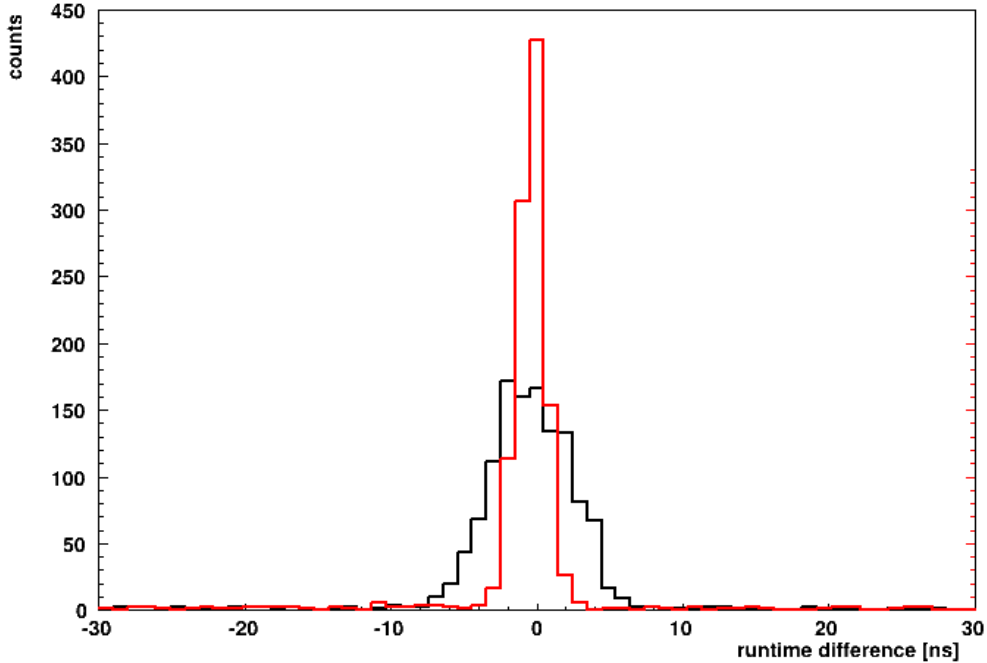


Figure 36: The difference in time between the left and the right SiPM for the case that the channels are on different FADCs (black) and that they are on the same FADC (red). The distribution for different FADCs is much broader.

One can clearly see, that in case of two FADCs the distribution is much broader and we therefore have to use the combination Ch5-Ch10 even if for example Ch1-Ch6 show a slightly higher light yield. To find the best method of determine the timing information for our analysis, we examine how well we can separate the three beam positions. The results can be seen in the figures 37, 38 and 39.

All means and standard deviations for the histograms in the figures 37, 38 and 39 are listed in table 3.

	FPBT	FFunc	SWFunc
Δt_{Pos1} [ns]	0.64 ± 1.1	0.46 ± 1.3	0.47 ± 2.1
Δt_{Pos0} [ns]	-0.35 ± 1.0	-0.20 ± 1.2	-0.21 ± 2.1
Δt_{Pos2} [ns]	-1.2 ± 1.1	-0.71 ± 1.3	-1.0 ± 2.1

Table 3: Time differences for each method and each position.

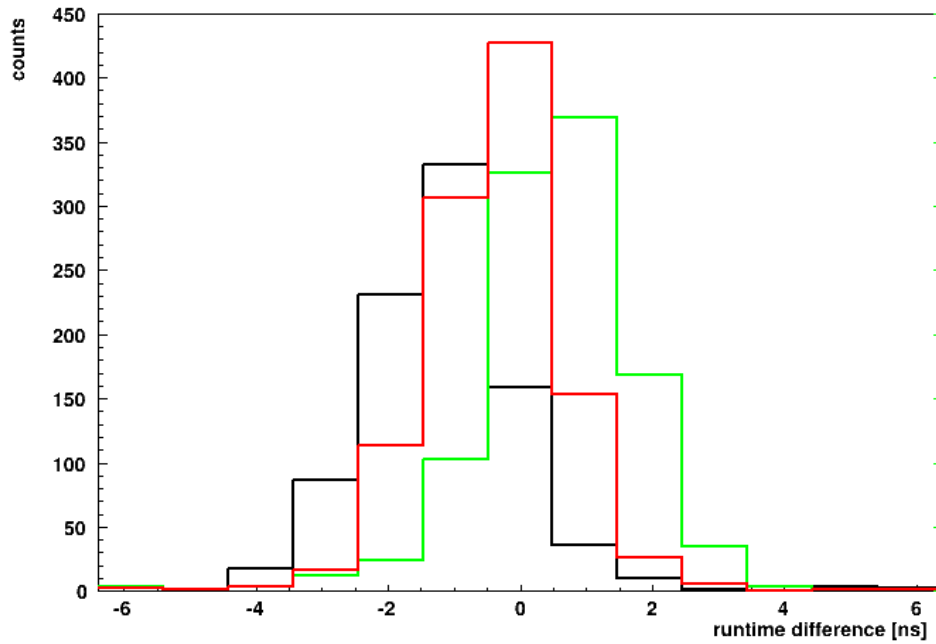


Figure 37: Time difference ($t_L - t_R$) for the FPBT-method for Pos 1 (black), Pos 0 (red) and Pos 2 (green).

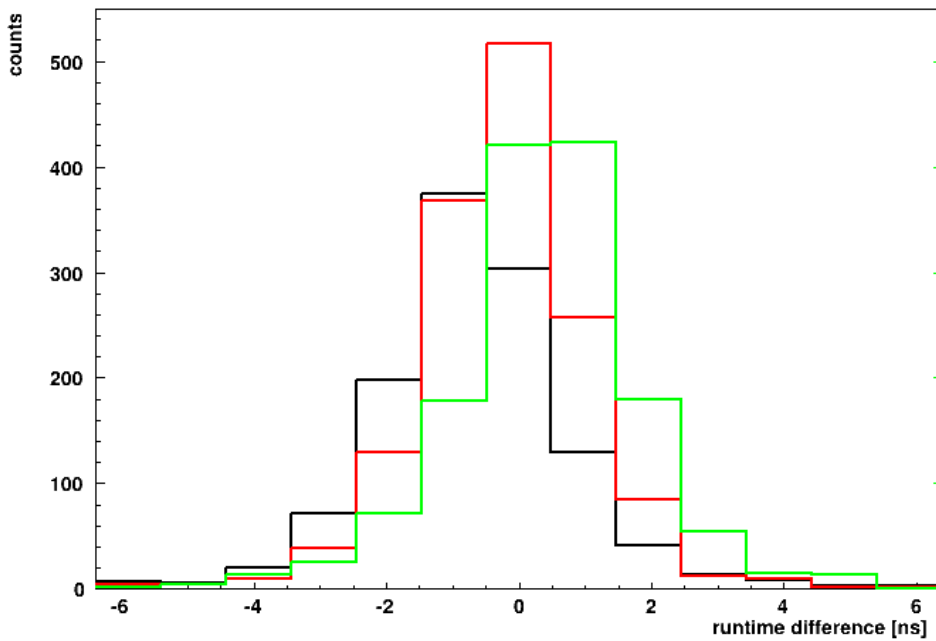


Figure 38: Time difference ($t_L - t_R$) for the FFunc-method for Pos 1 (black), Pos 0 (red) and Pos 2 (green).

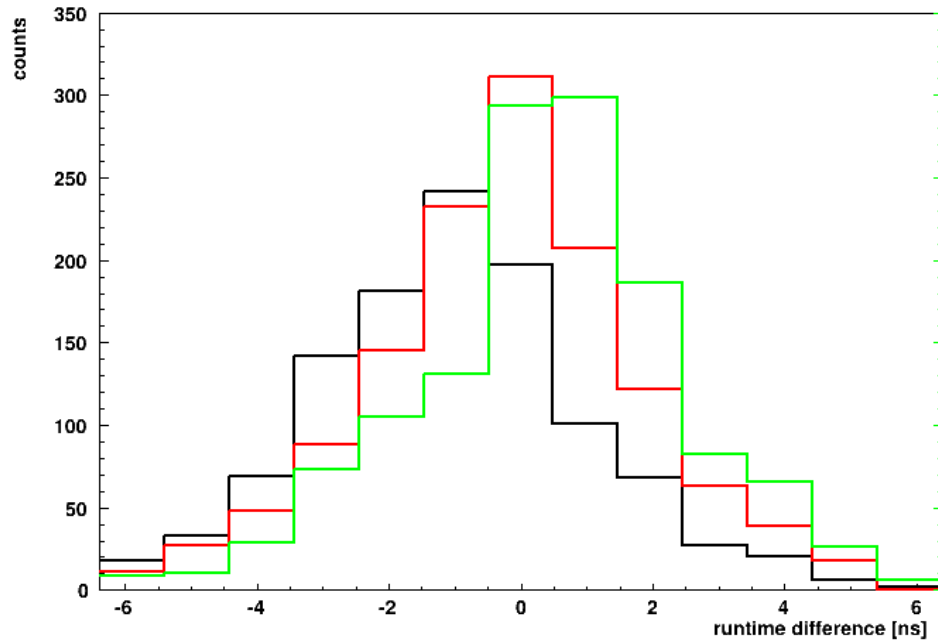


Figure 39: Time difference ($t_L - t_R$) for the [SWFunc](#)-method for [Pos 1](#) (black), [Pos 0](#) (red) and [Pos 2](#) (green).

Since the [FPBT](#) has the smallest errors, we continue with this method. The low errors can be explained by the fact, that this method is insensitive to the actual shape of the signal. The two fitting methods always depend on the shape of the signal and therefore the parameters can slightly vary due to the amount of collected light and/or after pulses, even if the actual time is always the same.

In section [5.1](#) we explained three ways how to convert a timing information into a spatial information and discussed the fact, that the third way, equation [5.1.5](#), has the lowest amount of operations with the measured values. Concerning the rather large errors as listed in [table 3](#), we expect that this way should provide the best conversion between time and space. Histograms for all ways of deriving the x position are displayed in [figures 40, 41](#) and [42](#). We insert here the results of the [FPBT](#) method into the three equations of section [5.1](#) and compare their results.

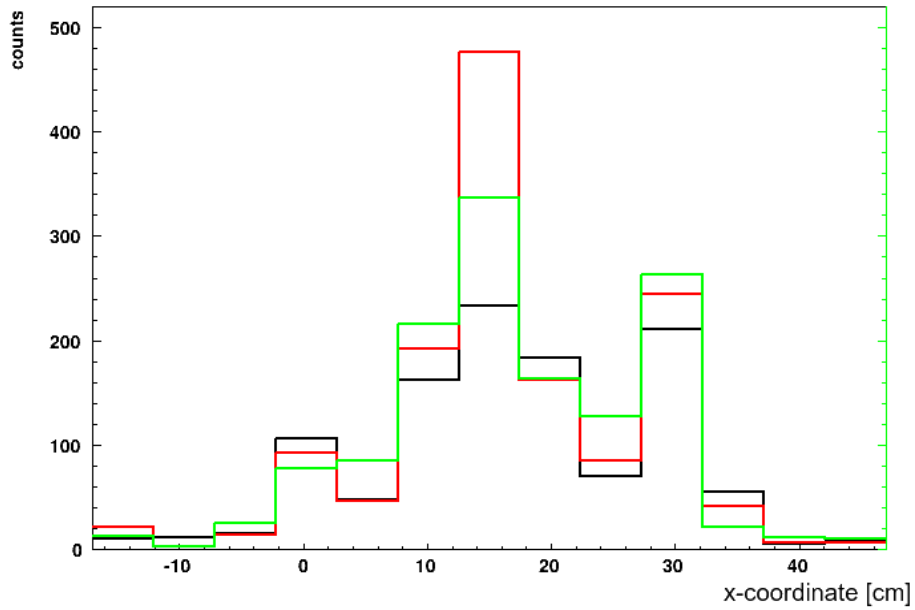


Figure 40: Determination of the x coordinate according to equation 5.1.2 for Pos 1 (black), Pos 0 (red) and Pos 2 (green).

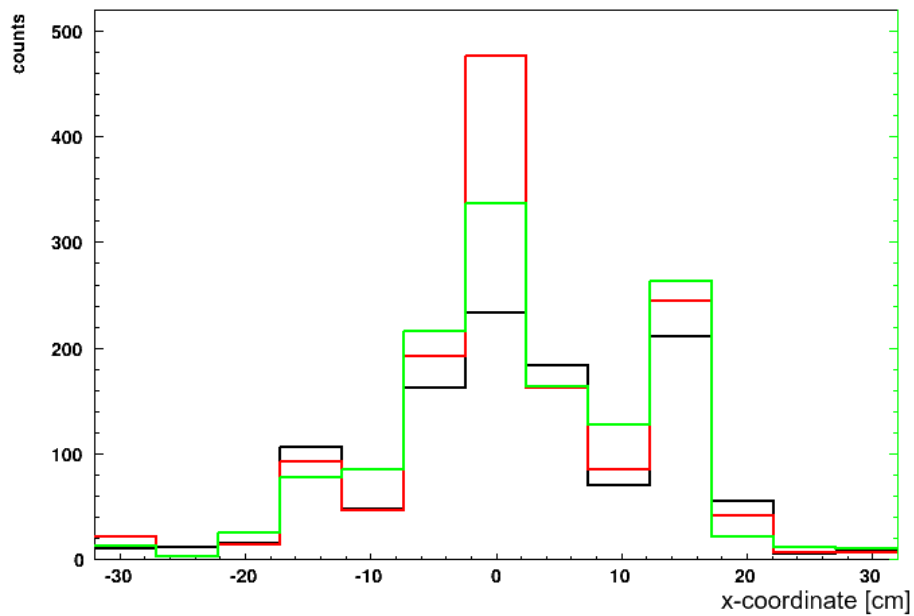


Figure 41: Determination of the x coordinate according to equation 5.1.3 for Pos 1 (black), Pos 0 (red) and Pos 2 (green).

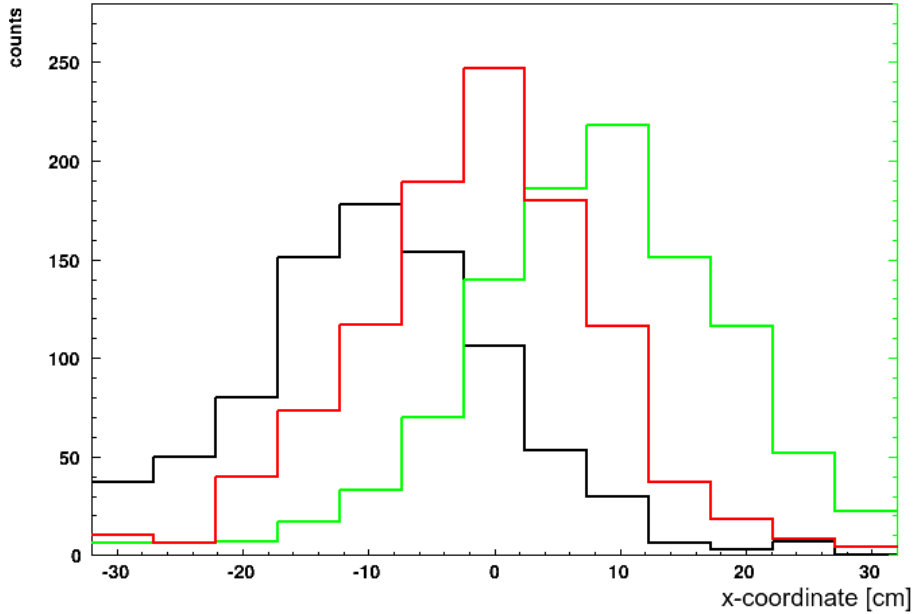


Figure 42: Determination of the x coordinate according to equation 5.1.5 for Pos 1 (black), Pos 0 (red) and Pos 2 (green).

The results of the analysis are listed in table 4 with respect to the equations in section 5.1 which are used to convert the time to a spatial information.

	equation 5.1.2	equation 5.1.3	equation 5.1.5
x_{Pos1} [cm]	16 ± 9.5	1.2 ± 9.5	8.6 ± 10
x_{Pos0} [cm]	17 ± 9.3	2.0 ± 9.3	-1.0 ± 9.2
x_{Pos2} [cm]	17 ± 9.9	1.7 ± 9.9	-9.5 ± 9.9

Table 4: Time differences for each method and each position.

The first two ways of deriving the x position show no position resolution at all. They both show a Gaussian like distribution around the mid of the detector and two peaks at the end of the detector¹⁷. The problem we have here is, that the points in time between both readout channels are too close to each other. In equation 5.1.2 the term $t_L + t_R$ is therefore approximately twice as large as the numerator resulting in a factor of $\frac{1}{2}$. Basically the same happens in equation 5.1.3 where the numerator $t_L - t_R$ is small and the denominator $t_L + t_R$ is large, which gives a factor zero. The peaks come from events where either $t_L = 0$ or $t_R = 0$. In

¹⁷The detector has a length of 30 cm.

these cases the fractions of the time values become either zero or one. Equation 5.1.5 has no such fraction. Here one can see a shift of the distribution towards the correct positions of the beam and therefore we can show, that a position resolution with light propagation time information can be achieved.

Comparing this results to the energy resolution for the Cosmic Ray Facility (CRF) as listed in table 1 it can be seen, that we can set a cut to cosmic muons with an energy lower than 1 GeV , which is not sufficiently better than the pre selector, as mentioned in section 5.3. Additionally the measured maxima do not fit the real beam positions and, due to the large resolution, there are non physical results, where the analysis claims a position outside the detector. All these problems come basically from a low light yield and readout electronics, which are not designed for the required resolution. Enhancing the light yield and using optimized readout electronics will sufficiently improve the resolution. A study to enhance the light output can be found in chapter 7 and measurements with better readout electronics are described in [Ruschke, 2014].

6.2 Pulseheight Information: The y -Direction

A detailed description of the measurement and the analysis for this direction can be found in [Ruschke, 2014]. This section gives just a brief summary of the achieved position resolution in y direction, obtained from results of the first prototype detector.

We perform a scan in y -direction in 5 mm steps with 10^4 events per beam position. As already mentioned in the previous section, the light output of the detector is low and the resulting position resolution is large and we therefore want to present only three steps of the scan, as shown in figure 43.

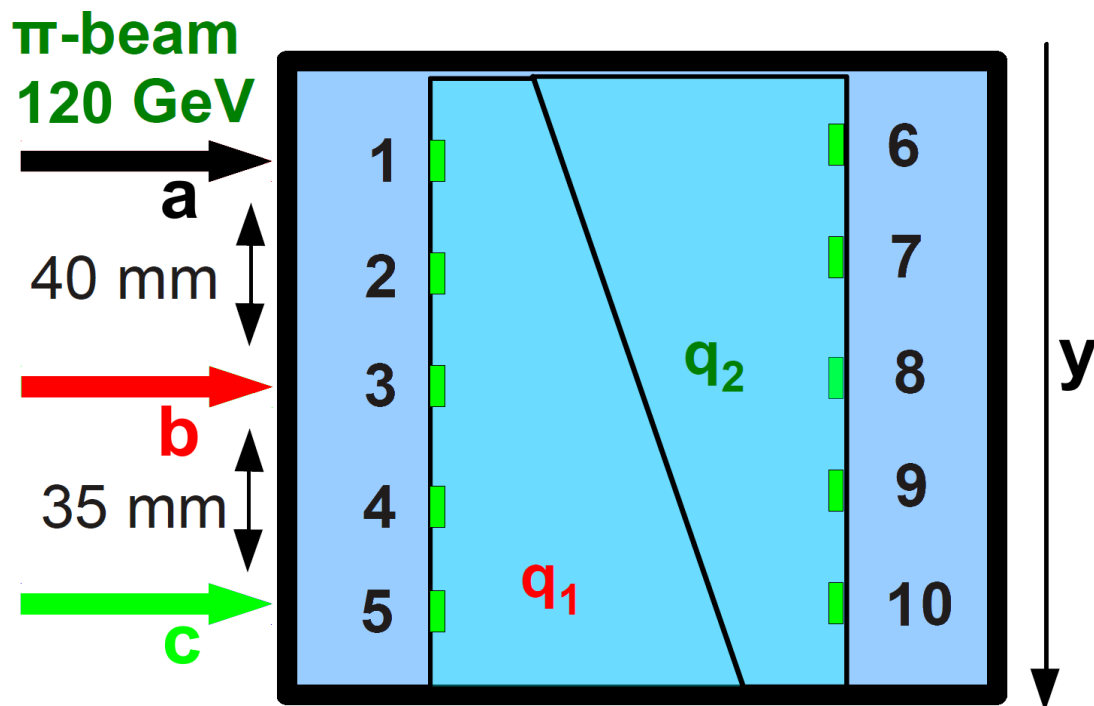


Figure 43: Analyzed beam position of the y scan with respect to the fiber positions.

As a first approach, we assume that all channels show a light yield, that is correlated to the position of the pion beam, as explained in section 5.2. The mean number of photons for the three beam position in each channel is plotted in figure 44

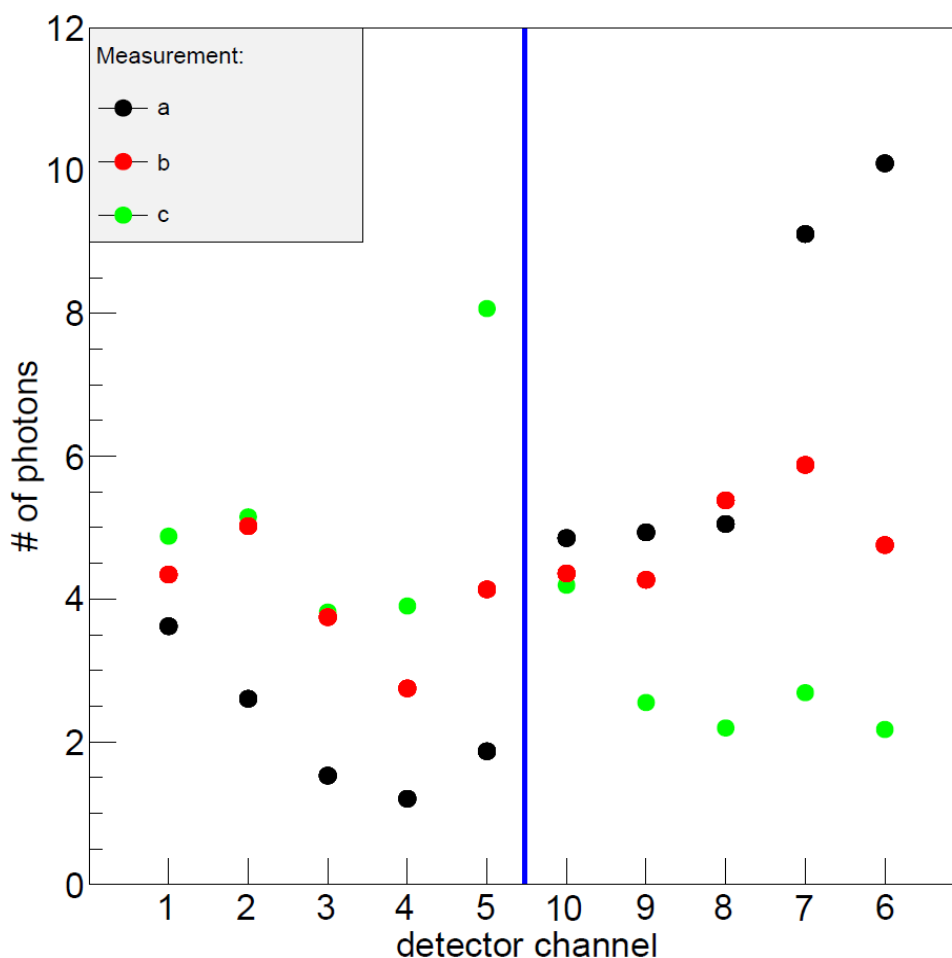


Figure 44: Mean number of photons in each channel for the three different beam positions. The variation of the photon number with the beam position for channels at the thin end of scintillator is low. For example channel 1 shows a signal in a region from 3.5 to 5 photons.

It can be seen, that the assumption, that all channels are position sensitive, is not true: Channel 1 - 3 and 8 - 10, i.e. the channels at the thin side, show only a small variation of light yield with beam position compared to the channels at the broad side. Still the overall light output from the detector is low, 1 to 10 photons per SiPM, especially when the beam position is far away from the readout channel. We use the channels at the broad end, channel 5 and channel 6, which show the best position dependency to reconstruct the beam position, according to equation 5.2.5. A result of the analysis can be seen in figure 45

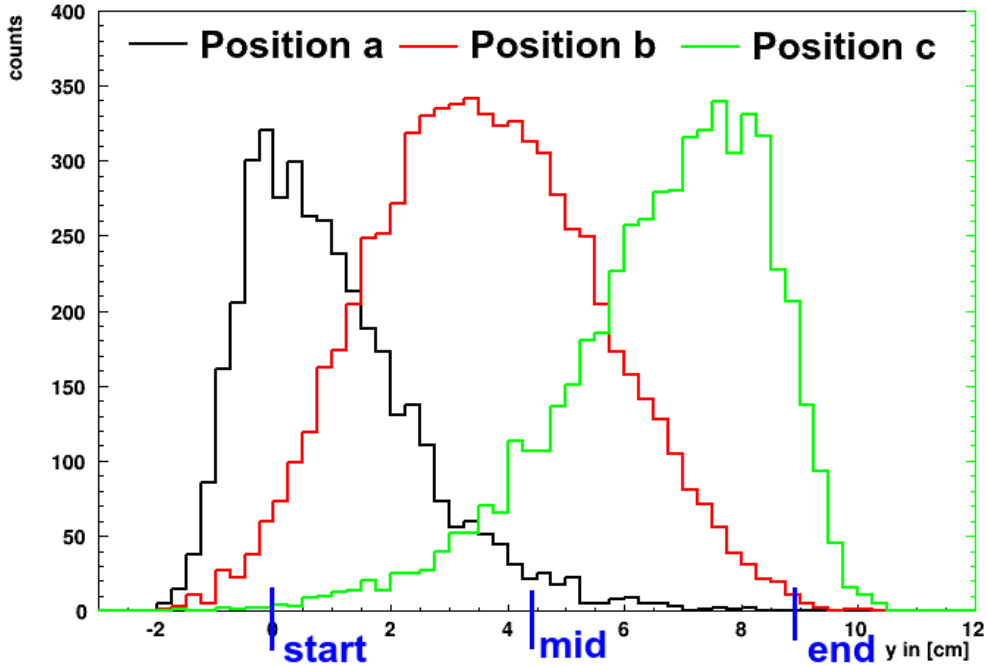


Figure 45: Reconstructed beam positions according to equation 5.2.5.

As for the x -direction, we see a separation of the three distributions resulting for the direction in a position resolution of 3 cm (FWHM). Comparing this value to the energy resolution of table 1 we see, that it is possible to set a cut on the energy cosmic muons in the CRF at 2 GeV , which is about a factor of three better than the preselection, see section 5.3.

One can also see, that the three graphs in figure 45 are not symmetric around the center of the scintillator, $y = 4.4\text{ cm}$. This may have two reasons: We could have an offset on the height of the beam position and the first trapezoid can have a slightly lower light output than the second one. A hint for a lower light output can be seen in figure 44, in which the channels 6 - 10 show slightly more photons than the channels 1 - 5.

Another problematic point is the fact, that we calculate beam positions where there is actually no scintillator. This result can be explained by a correlation between the position of the readout channel the beam position. If the distance is large, less photons will arrive at the readout channel due to absorption in the scintillator material. We will see this effect in all of the following measurements, but we will concentrate in this work to the enhancement of the light output of the detector.

We could demonstrate the concept of this detector and now have to find ways to further enhance the position resolution of the trapezoidal structure. We investigated several experiments to learn how we can optimize the light collection and output of the whole detector. Possible improvements, to enhance the light output, are for example:

- We do not take care of the fiber routing. On the distance between the scintillator and the FC-connector the fibers are highly bended. In an ordinary optical wave guide the light is inserted perpendicular into the fiber. In this case one can bend the fiber up to a critical angle and the light still fulfills the requirement of total reflection. For the case of a [WLSF](#) the light is produced inside the fiber within a solid angle of 4π . Therefore a bending of a [WLSF](#) results in less photons fulfilling the requirement of total reflection. Since only 3% of the light shifted to a green wavelength in the [WLSF](#) is guided to the [SiPM](#) in the case of a linear fiber, see section [4.1](#), we have to take care, to bend the fiber as less as possible.
- We choose the aluminium wrapping without testing its reflective properties. Different materials have to be tested to find the cover, which provides the best reflective properties, like low absorption coefficient or an emission of light in directions where photons fulfill the requirement of total reflection at the next wall of the scintillator as often as possible. As presented in chapter [7](#), we can enhance the light output by a factor of two when using a diffuse reflective cover material.
- With this prototype we also test just one trapezoidal geometry and five fiber positions. Further geometries and fiber positions have to be tested in the next prototypes. Possibilities are for example a smaller trapezoid in y direction and fibers at the corners of the scintillator.

Measurements and simulations concerning the enhancement of the light output will be presented in the next chapter.

7 Light Output Studies

One of the basic things we learn from the first prototype detector is, that the light yield has to be enhanced to improve the already visible resolution. We test, by measurements, as well as by Monte Carlo simulation, different approaches to enhance the light yield.

At first we test the effect of diffuse reflective cover material on the light output in experiment and compared it to the results of our simulations. The trapezoid we use for this experiment is half as long¹⁸ as the trapezoid of the "CERN prototype", but besides this it has the same geometry. The simulation is further used to check new possible geometries and positions for WLSFs.

7.1 Measurement with Different Reflective Cover

The first thing we do, to improve the light yield of the trapezoidal scintillator, is to search for other cover materials than aluminium foil. We choose a diffuse reflective paper-like material called Tyvek [DuPont, 2012], Teflon tape BC 642 [Saint Gobain, 2012] and a reflective paint based on TiO_2 called BC 622a [Saint Gobain, 2012]. Figure 46 shows the basic components of the setup and table 5 shows the dimensions of the used trapezoid.

X_{scin}	15.0 cm
Y_{scin}	8.8 cm
Z_{scin}	4.6 cm
Z_{thin}	1.0 cm

Table 5: Dimensions of the trapezoid used in the cover material measurement.

The used trapezoid is investigated with cosmic muons. The red cuboids in figure 46 are trigger scintillators defining the allowed trajectories of the incoming muons. Each of them has an effective area of $(10 \times 2.5)\text{ cm}^2$. They can be mounted at three positions, called "left", "middle" and "right". The sketched position is the left one. The coordinate of the centers of the three positions are listed in table 6.

¹⁸ $X_{scin} = 15\text{ cm}$.

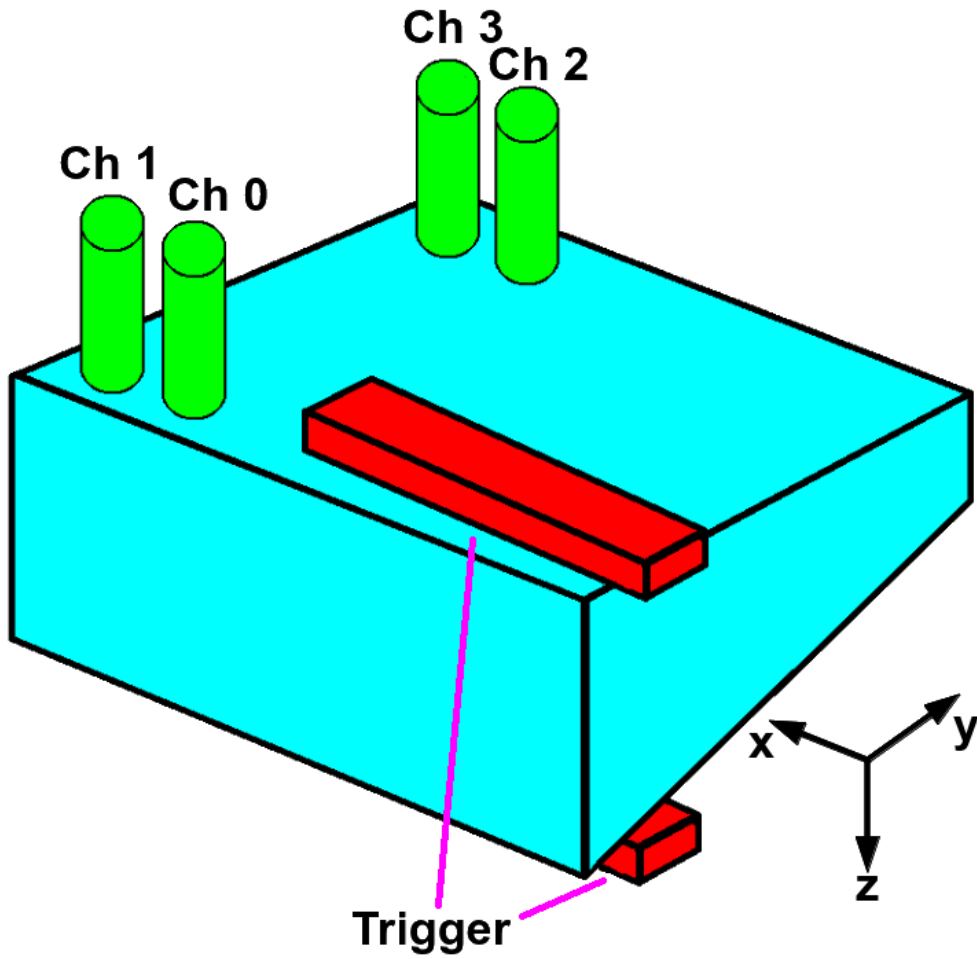


Figure 46: Setup of the cover material study. The green cylinders are [PMTs](#) and the red cuboids are trigger scintillators being in this case on the left side.

	left	middle	right
x [cm]	5.0	5.0	5.0
y [cm]	1.8	4.4	7.0

Table 6: Coordinates in the $x - y$ plane of trigger center.

The scintillator is read out with four [PMTs](#), as introduced in section 4.2, shown in green in figure 46, and the [QDC](#) readout system, explained in section 4.4.

Before the tubes are glued on the scintillator's surface, they have been calibrated to ensure, that they show the same pulseheight when being exposed to the same

amount of photons. For this purpose we used a LED-driver¹⁹ pulsing UV light into the tube with constant light yield. The bias voltage (V_{bias}) we apply to the PMTs was increased from 700 V to 800 V in steps of 10 V. The pulseheight diagram of each measurement was fitted with a Gaussian and the means were plotted in a graph. We define tube 3 at a bias voltage of 750 V to be our reference and then search the voltage for each PMT, where it shows the same pulseheight as tube 3 does at 750 V. Therefore we fit the means of the Gaussians for each PMT with a quadratic polynomial. This fit function was chosen because it interpolates the data points very well, see figure 47, and it can be inverted analytically.

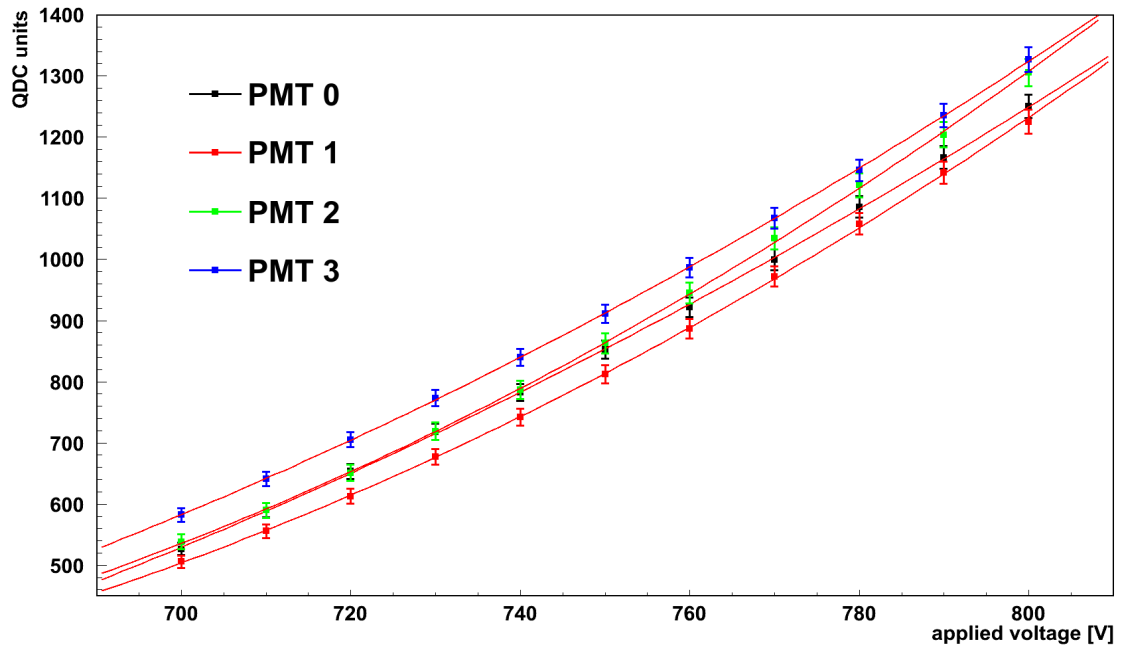


Figure 47: Amplification curves of the four PMTs, fitted with a polynomial of degree two.

A list of the four fitted function is given in the equation set 7.1.1

$$\begin{aligned}
 f_{Ch0}(V_{bias}) &= 0.01506 \cdot V_{bias}^2 - 15.38 \cdot V_{bias} + 3921 \\
 f_{Ch1}(V_{bias}) &= 0.01693 \cdot V_{bias}^2 - 18.17 \cdot V_{bias} + 4923 \\
 f_{Ch2}(V_{bias}) &= 0.01960 \cdot V_{bias}^2 - 21.71 \cdot V_{bias} + 6129 \\
 f_{Ch3}(V_{bias}) &= 0.01713 \cdot V_{bias}^2 - 18.28 \cdot V_{bias} + 4983
 \end{aligned} \tag{7.1.1}$$

¹⁹The LED-driver was taken from the SP5600A SiPM KIT from CAEN [CAEN, 2011c].

To get for each tube the correct voltage, we solve the quadratic function for the voltage and inserted the mean of the pulseheight of tube 3 at 750 V. The V_{bias} and the positions of the tubes on the scintillator are listed in table 7. The values of the bias voltages were set, computer controlled, at the power supplies, *iseg SHQ 224M* [Iseg, 2006].

	Channel 0	Channel 1	Channel 2	Channel 3
x [cm]	3.9	2.2	3.9	2.9
y [cm]	0.7	0.7	8.0	8.0
V_{bias} [V]	757.4 ± 2.0	762.5 ± 2.0	755.5 ± 1.9	750.0 ± 0.01

Table 7: Coordinates in the $x - y$ plane of PMT centers and corresponding V_{bias}

We shielded the PMTs against magnetic fields with a μ -metal cylinder. After that, we wrapped the detector in five kinds of cover material: aluminium foil, one layer of Tyvek, a multilayer wrapping of Tyvek consisting of at least four layers, a wrapping with Teflon tape and diffuse reflective paint based on TiO_2 . The latter four cases were both finally wrapped in aluminium to make the whole detector light tight. The aluminium foil is chosen, because the wrapping and unwrapping with it is practicable and it reflects the photons, which escape the diffuse reflective wrapping back into the scintillator. At the time when we wrap the scintillator with Teflon, we already know the results from the Tyvek multi layer measurement. From there one can see that if one deals with cover materials, which are a bit transparent, it is better to use more than just one layer. We therefore skipped the measurement with a single layer of Teflon and immediately wrapped the scintillator multi layered.

The measurements were performed in a climate chamber, which ensured a constant temperature of $T = 20^\circ C$ and a constant air humidity of 30%.

We choose this trigger configuration to increase the rate of the accepted cosmic muons, which is even in this case extremely low: $\approx 0.06 Hz$. But due to this configuration the setup has the disadvantage, that the path length in the scintillator can differ by a factor of up to 2 for each muon since this configuration does not cut on perpendicular tracks. As a result the shape of the distribution deviate from a Landau distribution as shown in figure 48.

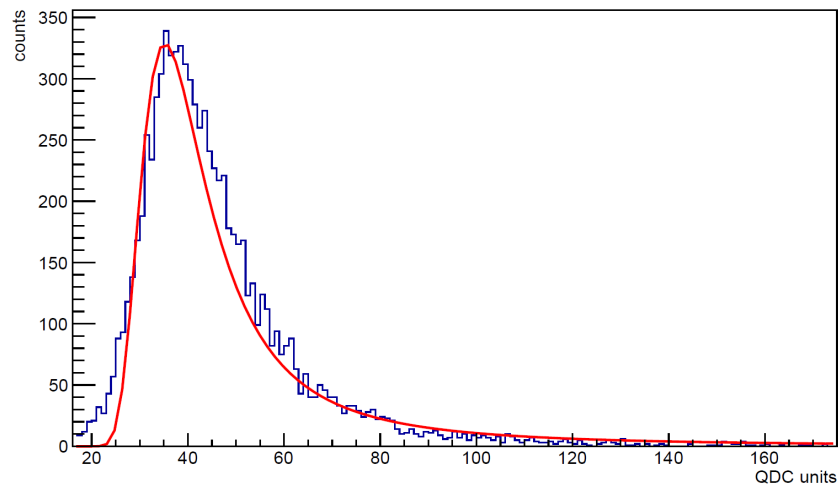


Figure 48: Distribution of the QDC values for Channel 1 and an aluminium wrapping with the triggers on the left. 8960 events. The red curve describes a fitted Landau distribution.

In order to fit the maximum of this distribution, we zoomed in, until the fitted Landau curve describes the given data points well. In general the Landau distribution describes the rising edge better than the falling edge. Figure 49 shows the same data as figure 48 but we zoomed in and fitted just the shown data points. One can see, that the fitted curve describes the behavior of the measured distribution at its maximum well.

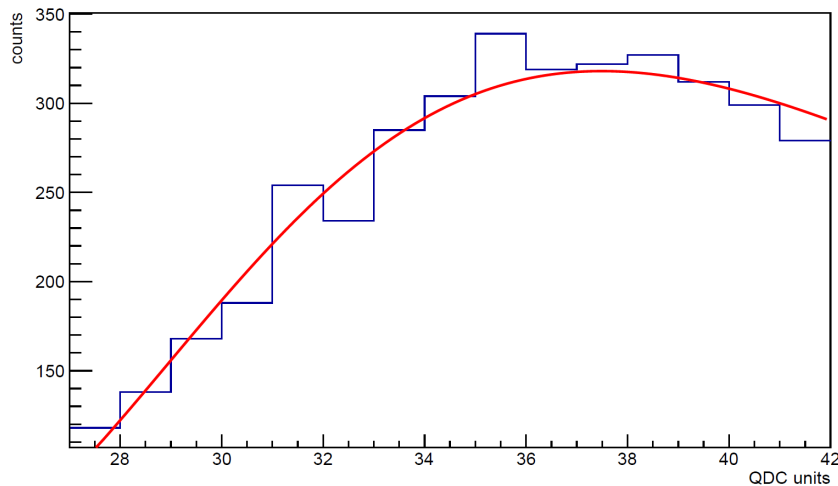


Figure 49: Distribution of Figure 48 zoomed around its maximum and fitted with a Landau curve.

The values of the maxima represent the measured light output for each cover and each channel. These values are listed in table 8

		Aluminium	1 × Tyvek	4 × Tyvek	4 × Teflon	TiO_2
left	Ch 0	39.3 ± 6.7	62.7 ± 9.2	79.3 ± 11	73.6 ± 12	48.6 ± 8.6
	Ch 1	38.3 ± 6.0	59.8 ± 9.2	73.2 ± 10	66.5 ± 10	42.9 ± 6.7
	Ch 2	31.9 ± 5.2	58.3 ± 8.1	74.0 ± 9.3	68.5 ± 10	40.7 ± 6.7
	Ch 3	35.4 ± 6.5	61.4 ± 8.1	76.3 ± 10	67.0 ± 9.0	42.5 ± 6.3
middle	Ch 0	21.9 ± 4.2	40.8 ± 6.7	51.0 ± 8.0	46.6 ± 7.9	31.5 ± 5.1
	Ch 1	22.2 ± 3.8	23.1 ± 3.6	46.1 ± 7.0	43.4 ± 7.2	29.2 ± 5.2
	Ch 2	27.5 ± 4.6	47.2 ± 7.7	60.6 ± 10	50.5 ± 8.5	28.3 ± 5.5
	Ch 3	28.2 ± 4.2	48.3 ± 7.0	59.3 ± 8.5	49.8 ± 7.7	29.8 ± 5.1
right	Ch 0	10.2 ± 2.6	22.8 ± 4.6	27.7 ± 5.8	24.5 ± 5.6	16.7 ± 3.8
	Ch 1	12.0 ± 3.1	22.3 ± 4.2	25.1 ± 4.8	22.9 ± 5.2	15.9 ± 3.4
	Ch 2	19.1 ± 4.2	31.6 ± 6.2	38.2 ± 6.8	31.1 ± 6.9	15.6 ± 4.0
	Ch 3	19.9 ± 3.9	32.3 ± 5.8	38.2 ± 6.7	30.2 ± 6.1	17.1 ± 3.9

Table 8: Maxima of light output for all channels and all cover materials in QDC units. The light yield of the scintillator can be doubled by using a multi layer of Tyvek as cover material.

The first thing to mention about the results, is the fact, that the measured pulse-heights for two neighboring channels, i.e. Ch0-Ch1 and Ch2-Ch3, are, with respect to the errors, equal. The only exception is channel 1 for the middle position with a single layer of Tyvek. For this measurement channel 1 shows a light output, which is about a factor of two too low, compared to other measurements. It turns out, that this is the result of a loose wire and the error did not occur in the next measurements.

At next we look at the effect of the different cover materials. As listed in table 8, a wrapping consisting out of multi layered Tyvek shows the highest light output of the measured five cover materials. This result is also shown in figure 50 for channel 0 and for all three trigger positions.

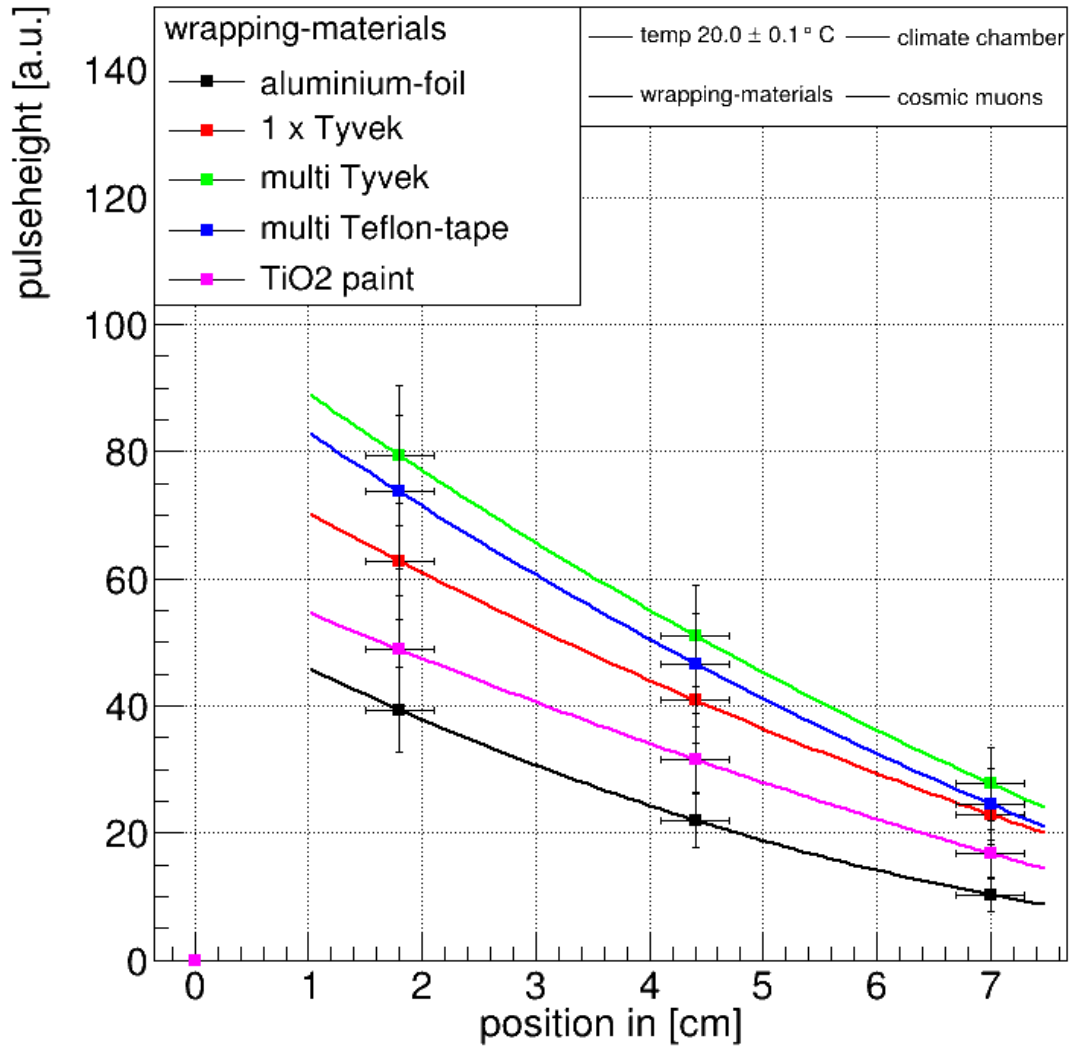


Figure 50: Result for channel 0 for the different cover materials at the three trigger positions. A polynomial of degree two is fitted through the data points.

The use of a diffuse reflective cover, no matter which one, enhances the light output of the scintillator by almost a factor of two, compared to the aluminium foil.

Comparing Tyvek and Teflon by eye, one sees, that Tyvek is shiny, while Teflon is pale. This might be an explanation for the slightly lower light output with a Teflon cover.

The last point we want to stress, is the decreasing light output as the trigger moves to the right. This behavior is plotted for the multi layer of Tyvek cover material and all channels in figure 51.

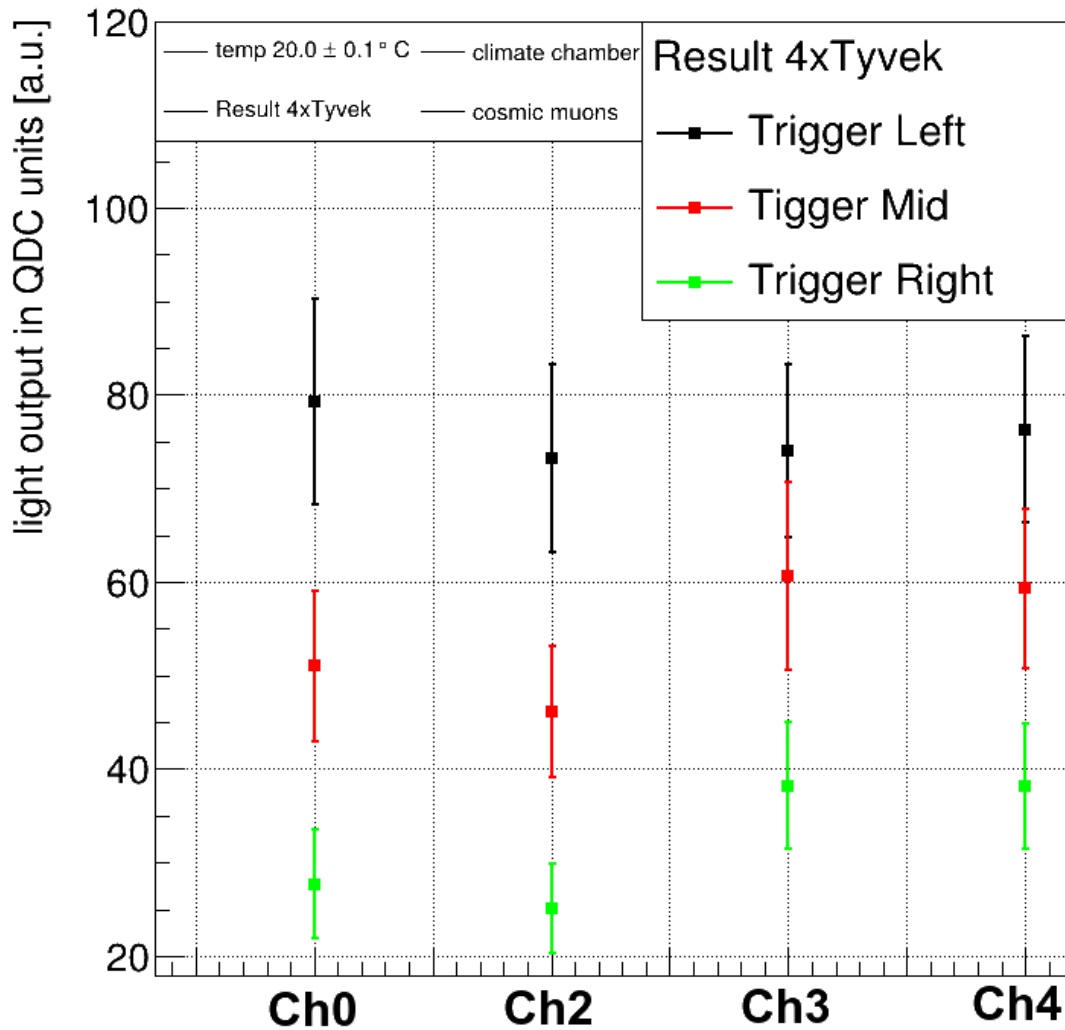


Figure 51: Results of the pulseheight measurement with three trigger positions for all channels. The scintillator is wrapped in a Tyvek multi layer. The data points for channels at the same side of the scintillators are almost equal. The decrease of the light yield at the thin side is weaker than on the right side.

Here channel 0 and 1 and channel 2 and 3 show almost the same light yield. If one compares the the different sides of the scintillator one can see, that the decreasing of the light output with a trigger moving to the right happens faster for the broad side. We want to have a closer look on this effect and concentrate on channel 0 and channel 2. Figure 52 shows the light yield of both channels as a function of the trigger position.

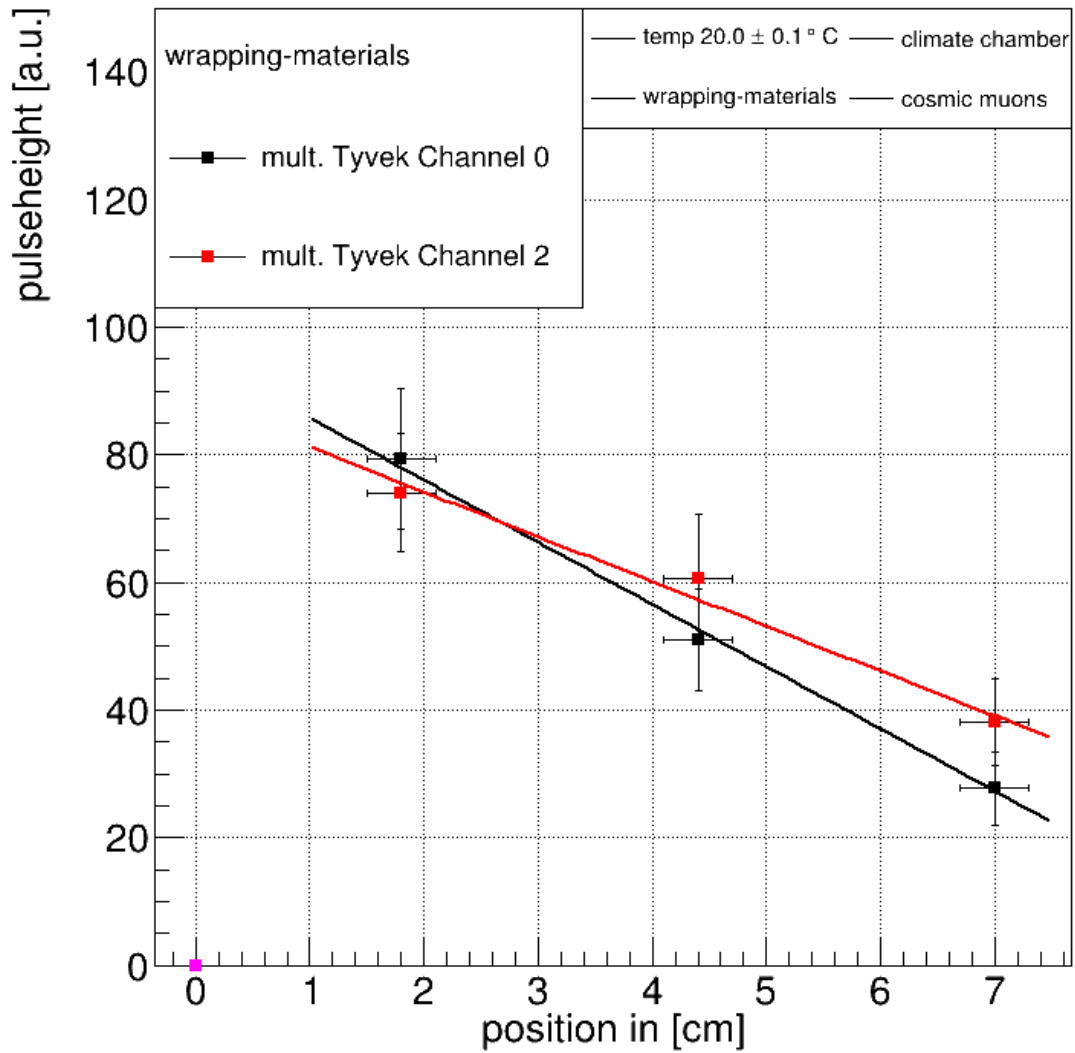


Figure 52: Results of the pulseheight measurement with different trigger positions for channel 0 and channel 2. The scintillator is wrapped in a Tyvek multi layer, since it shows the largest pulseheights and therefore gives the clearest picture. A linear function was fitted to the data points to visualize the faster decreasing of the light yield for channels at the broad side.

One can also see that decreasing of the pulseheight of channel 2 is weaker than for channel 0. This can be seen as a correlation between the trigger position and the readout channel position. We assume, that we see an increasing light output, if the trigger and therefore the photon source is closer to the readout channel. This means for channel 0 and 1, that a trigger at the thin side causes on the one hand

less photons than if it were on the thin side and on the other hand less photons will arrive at these readout channels since the distance between photon production and photon detection is large. The decreasing of the collected light is therefore intensified with the trigger moving to the right. For both readout channels at the thin side these effects adds up destructively. If the trigger is on the right, more photons will be produced but less of these photons will arrive at the thin side. The decrease of the light yield is therefore faster for a readout at the broad end of the trapezoid.

If we now set the trigger in the mid of both readout channels, we see that channel 0 already shows a lower light yield than channel 2. This means, that effective distance for photons traveling from the mid to the [PMT](#) at the broad side is longer, than for photons traveling to the thin side.

The company Saint Gobain Crystals notes, that a diffuse reflective covering is a bad choice if the scintillator is much longer than it is wide [[Saint Gobain, 2012](#)]. Therefore the result needs also to be tested with a longer scintillator. But from the current point of view, we should use a multi layer of Tyvek as cover material. In the next section we will introduce a simulation of light production and propagation within a trapezoidal scintillator. This simulation will be compared to this cover study and after wards used to analyze new geometries and fiber positions.

7.2 Monte Carlo Simulation of Light Propagation

In this section we describe the self developed simulation for light production and propagation in a trapezoidal shaped scintillator. An instruction sheet of how to use it, is given in appendix [A](#).

The program simulates a Landau like photon production and a light propagation containing total reflection as well as diffuse reflection at the scintillator surfaces. According to parameters one passes to the program, see appendix [A](#), it builds the shape of a scintillator and a readout structure. Currently the program can build three different kind of shapes: a cuboid, a trapezoid and a double layer of trapezoids like the first prototype. For readout, one can switch between fiber and tube readout.

After the construction of a certain shape of the scintillator and the initialization of the readout structure, the actual simulation starts. A total simulation run can be summarized as a repetition of the following steps for a given number of muons N_{muon} :

1. Calculation of a muon track
2. Calculation of an interaction point of the muon and the scintillator.
3. Production of a certain amount of photons at the interaction point and emitting of these photons isotropically in all directions
4. Processing a random walk of photons and counting them, if they hit a sensitive area
5. Filling the data in histograms
6. Continue with the production of photons along the trajectory of one muon

We will now go through all the steps in more detail:

1. The program calculates a random point A in the upper trigger area and a $\cos^2\vartheta$ distributed direction \underline{d} . If a line from A with the direction \underline{d} hits the lower trigger area in a point B , this line is a muon trajectory. If the lower trigger is not hit by the line a new direction \underline{d} is calculated. The recalculation will be repeated until a muon trajectory AB is found.

2. To find an interaction point of the muon with the scintillator, we calculate a random distance l from A or a later interaction point to the next one. The probability P for a particle to make an interaction with the scintillator after a length l is given by [Biebel, 2009]

$$P = 1 - \exp\left(-\frac{l}{\mu}\right) \quad (7.2.1)$$

with a mean free path μ . By inverting this function one gets an expression for l :

$$l = -\mu \cdot \log(1 - \text{rand}[0; 1]) \quad (7.2.2)$$

with $\text{rand}[0; 1]$ being a random number between 0 and 1 and $\mu = 1 \mu m$. We then go from A or from the former interaction point l units in the direction \underline{d} and end up at the interaction point.

3. In each interaction point the program calculates the number of photons emitted in this point. The distribution of this number follows a Landau distribution. Mathematically the number of produced photons can be arbitrary high. If a muon interacts with an electron in reality, the electron can get a maximum energy according to [PDG, 2012]:

$$T_{max} = \frac{2m_e c^2 \beta^2 \gamma^2}{1 + 2 \cdot \frac{\gamma m_e}{m_\mu} + \left(\frac{m_e}{m_\mu}\right)^2} \quad (7.2.3)$$

For a mean energy of cosmic muons of $E_\mu = 4 \text{ GeV}$ we get a maximum energy transition of $T_{max} = 1.1 \text{ GeV}$. As stated in section 2.3, the mean energy it takes to create a scintillation photon is roughly 100 eV . This results in a maximum photon production of $N_{Ph;max} = 1.1 \cdot 10^7$ for this measurement. Such a limit must also be implemented into the simulation. If the calculated number of produced photons is larger than $N_{Ph;max} = 1.1 \cdot 10^7$, the calculation will be repeated until it is smaller.

4. For each photon we first calculate a path length within the scintillator according to

$$L_{free\ path} = -L_{mfp} \cdot \log(1 - \text{rand}[0; 1]) \quad (7.2.4)$$

With L_{mfp} being the mean free path of a photon in the scintillation material, which was passed to the program as parameter 17, see appendix A. In the next step we calculate an emission direction, which is isotropically distributed. From the point where the photon is created we find the first interaction point with a scintillator wall and calculate the distance to this wall. If this distance is higher than $L_{free\ path}$ this photon will be deleted and the program processes the next photon. If the photon is not deleted, it will hit the wall of the scintillator and the traveled length is stored in a variable $L_{traveled}$, which will be important later on.

Within the simulation we can choose between six reflection cases according to the value of parameter 14. For a detailed description of the reflection cases see appendix A. The simulation at first checks, whether the angle of incidence is larger than the angle of total reflection. If the angle is larger and the photon therefore fulfills the requirement of total reflection, it gets reflected with an angle of reflection equal to the angle of incidence. Still there are reflection cases where distinguished walls, like the inclined one, do not provide such a total reflection. We assume, that such walls may contain micro scratches, which reflect incoming photons diffusely. If the photon hits such a wall, the program calculates a new random direction for the photon to travel.

If the angle of incidence is smaller, then the reflection happens at the cover material, which is described by the reflection case and the reflectivity R_{cover} , being parameter 18, see appendix A. In each reflection case, one first calculates a random number between zero and one. If this number is larger than the reflectivity, the photon is deleted. Otherwise it can either undergo a directed or a diffuse reflection. It should be noted here, that some reflection cases use a default reflectivity of $R = 0.91$, no matter which value parameter 18 has.

For a directed reflection the angle of reflection is again the angle of incident. At a diffuse reflective covering the program calculate uniformly distributed a new direction²⁰ for the photon with the only constraint, that the new direction must point inside the trapezoid. Now the program finds the next closest wall and calculates again the distance to it and add this distance to $L_{traveled}$. This process will be repeated until $L_{traveled}$ is larger than $L_{free\ path}$ and the photon is deleted. If the photon hits on its way through the scintillator an area where it is detected, then it may also be deleted according to the absorption mode of parameter 15, see appendix A.

5. Before processing the next photon, the program fills the data of the photon trajectory in histograms. Information stored this way is, for example:

- How often was a certain wall hit by this photon?
- Where exactly took this interaction place?
- Where was the photon detected?
- ...

All the histograms are themselves stored in a *root* file. The name of the *root* file contains several of the parameters passed to the simulation, as explained in appendix A.

6. Once all photons are processed and the important information of their trajectory is stored in histograms, the next intersection point of the muon with the scintillator is calculated with equation 7.2.2 and the procedure explained in step two and the whole process starts from the beginning. This will be repeated until the calculated intersection point is below the lower trigger area or below the scintillator. Then the next muon will be investigated until all muons are done.

In the following sections we describe studies with this simulation. At first we are going to calibrate the simulation and show that we can reconstruct the data of this cover measurement study.

²⁰This is of course a simplification since in reality a diffuse reflection provides an angle of reflection which is distributed around the angle of incidence.

7.2.1 Comparison of the Simulation to the Measurement

The goal of this subsection is, to calibrate the simulation and to compare it with the measurement. We therefore rebuild the cover measurement study, discussed in section 7.1, with the simulation program. The dimensions of the trapezoid and the position of the triggers and the PMTs are listed in the tables 5, 6 and 7.

For this study we vary the mean free path of the photons within the scintillator, L_{mfp} , and the reflectivity of the cover material.

We combine each L_{mfp} with all different reflectivities and compare the results to the real data. The used parameters are as follows:

- We investigated four values of the mean free path: 50 *cm*; 60 *cm*; 70 *cm* and 80 *cm*. We choose these values, since it was shown in former studies with the same OPAL scintillators, that they have a mean free path of roughly 60 *cm*, see for example [Adomeit, 2010] who found a mean free path of 63.5 *cm*. The fabricator of these scintillators claims a mean free path of new material being roughly 200 *cm*.
- We only simulated the directed reflection with one reflectivity $R_{dir.refl.} = 0.91$. The reflectivity of aluminium is 0.92, [Kohlrausch, 1996], for a wavelength of $\lambda_{BC400} = 423 \text{ nm}$, which is the peak emission wavelength of BC 400, [Saint Gobain, 2005]. Our aluminium foil is a bit faint and may partially contain scratches. Therefore we assume a slightly lower reflectivity than stated in the literature. Additionally the aluminium foil lays not everywhere directly on the surface of the scintillator, what may also effect the reflectivity.
- For the diffuse reflectivity we measure different light outputs for the four different diffuse reflective coatings, see section 7.1. We therefore vary the reflectivities for a diffuse reflection from $R_{dif.refl.} = 0.91$ to $R_{dif.refl.} = 1$ in 0.01 wide steps. Values for $R_{dif.refl.}$ smaller than 0.91 could also be possible. But since we have a higher light yield for a diffuse reflective cover, than for a directed one, we just test values higher than $R_{dir.refl.}$.

To check which simulation fits best to a certain cover material, we calculate two quantities.

1. The ratio of the most probable pulseheight for each channel within a particular measurement or simulation, resulting in six values, $\frac{Ch_0}{Ch_1}, \frac{Ch_0}{Ch_2}, \dots$, for each measurement and simulation. We can compare the values of the measurement to the ones of the simulation. For example, if we choose a too low L_{mfp} in the simulation and the trigger is on the left, less photons will arrive at channel 2 and channel 3. Fractions comparing one left channel with a right one, like $\frac{Ch_0}{Ch_2}$, will therefore be larger than in reality.
2. As discussed in section 7.1, different cover materials show different light yields. Therefore one has to find five reflectivities, which match the measurement data of the five cover materials, with one L_{mfp} . In order to compare different reflectivities, we calculate fractions of the pulseheights for each channel in different simulations, but with the same mean free path for photons. An example is the comparison for directed and diffuse reflection with the same reflectivity, $R_{dir.refl.} = R_{dif.refl.} = 0.91$, and $L_{mfp} = 70\text{ cm}$:
$$\frac{Ch_0(L_{mfp} = 70\text{ cm}; R_{dir.refl.} = 0.91)}{Ch_0(L_{mfp} = 70\text{ cm}; R_{dif.refl.} = 0.91)}$$

These quantities must be calculated for all measurements and all simulations. We now look for five simulations, which fit best to the measured data. One constraint to these simulations is the fact, that they all have to have the same mean free path for photons. Another constraint is the requirement, that they have to fit simultaneous the measured data, meaning that all simulations must fit on the one hand to their corresponding measurement and on the other hand a comparison for two different simulations must fit to the comparison of two different measurements. Therefore we start with the measurements containing the lowest and the highest light yields, i.e. aluminium and a Tyvek multi layer. For these we search the best mean free path. In the pool of all simulations with the best mean free path, we can then pick out two simulations which simultaneously fit the measured data. We keep in mind, that the remaining three measurements have a light yield in between these two reference measurements. After finding such a pair of simulations we go step by step through the other three measurements and find for each a corresponding simulation.

It turns out, that the simulations with a mean free path of 70 cm fit best to the measured data of the five materials. As stated above, [Adomeit, 2010] found a mean free path of 63.5 cm for the same scintillators, while [Saint Gobain, 2005] claims, that new scintillators of this kind provide a mean free path of roughly 200 cm . The amount of scintillator material from the OPAL experiment is large and some of the scintillator rods may have aged faster than others. The one we use for this study is bluish, while others shine more yellow. The bluish appearance is an indicator, that this scintillator is not much aged, resulting in a larger mean free path.

The five reflectivities in the simulations with $L_{mfp} = 70\text{ cm}$, which fit best to the five cover materials, are listed in table 9.

aluminium	directed reflection	$R_{cover} = 91\%$
$1 \times$ Tyvek	diffuse reflection	$R_{cover} = 93\%$
$4 \times$ Tyvek	diffuse reflection	$R_{cover} = 99\%$
$4 \times$ Teflon	diffuse reflection	$R_{cover} = 97\%$
TiO_2	diffuse reflection	$R_{cover} = 91\%$

Table 9: Parameters for the cover material in simulation, which provide the best agreement with the data.

The mentioned quantities to compare simulation and measurements for the five cover materials and their simulations are all listed in appendix B. In this section we want to discuss only a selection of these quantities.

At first we have a look on the quality of the simulation describing the light yields for channels at the broad side and channels at the thin side of the trapezoid, see figure 46. We therefore look at the ratio $\frac{Ch_0}{Ch_2}$ for a trigger on the left side, i.e. near to channel 0. Figure 53 shows the values of this fraction for all five cover materials and a trigger on the left.

The fact, that the ratio between channel 0 and channel 2 is larger than in reality, means, that in the simulation less photons arrive at the thin end of the trapezoid for a trigger being on the left. But obviously this effect is rather small for all covers except aluminium. The ratios for a TiO_2 cover are even almost equal. In case of Aluminium the large discrepancy, compared to the other values, might result from a lack of simulations with directed reflectivity. Another reason can be a partially diffuse reflective behavior of the Aluminium foil, since it may contains scratches and does not lay perfectly on the surface of the trapezoid.

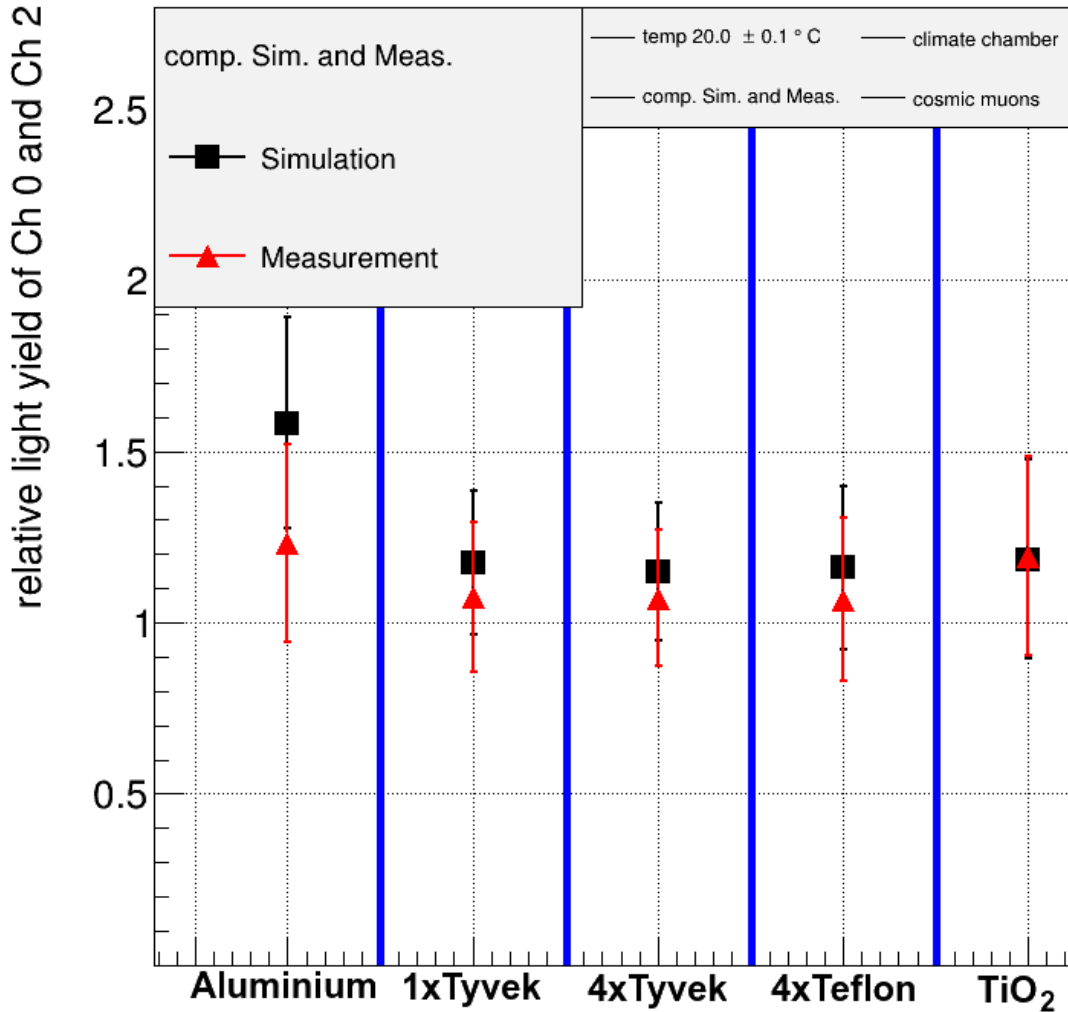


Figure 53: Relative light yield of channel 0 and channel 2 with the trigger on the left position. The values fits within the errors to the measurement for each cover material of the simulation. To optimize the discrepancy for the aluminium cover, we have to perform simulations with other reflectivities for directed reflection.

For the case of a trigger on the right, the simulation shows a lower ratio than the measurement, see appendix B. This also means, that less photons arrive at the broad end of the scintillator when the trigger is on the right. Generally speaking photons are absorbed too early in the simulation and thus the channels far away from the trigger show systematically a too low light yield.

One obtains the same results for the difference between measurement and simulation, when looking at the ratios of channel 1 and channel 3, see appendix B.

In a next step, we have a look at the ratio of the light yields for two cover materials. We take the Aluminium cover as a reference, since it is the material of the first prototype, and calculate the percentage of the light yield for an Aluminium cover compared to the diffuse reflective materials. The results for channel 0 and a trigger at the middle position is shown in figure 54.

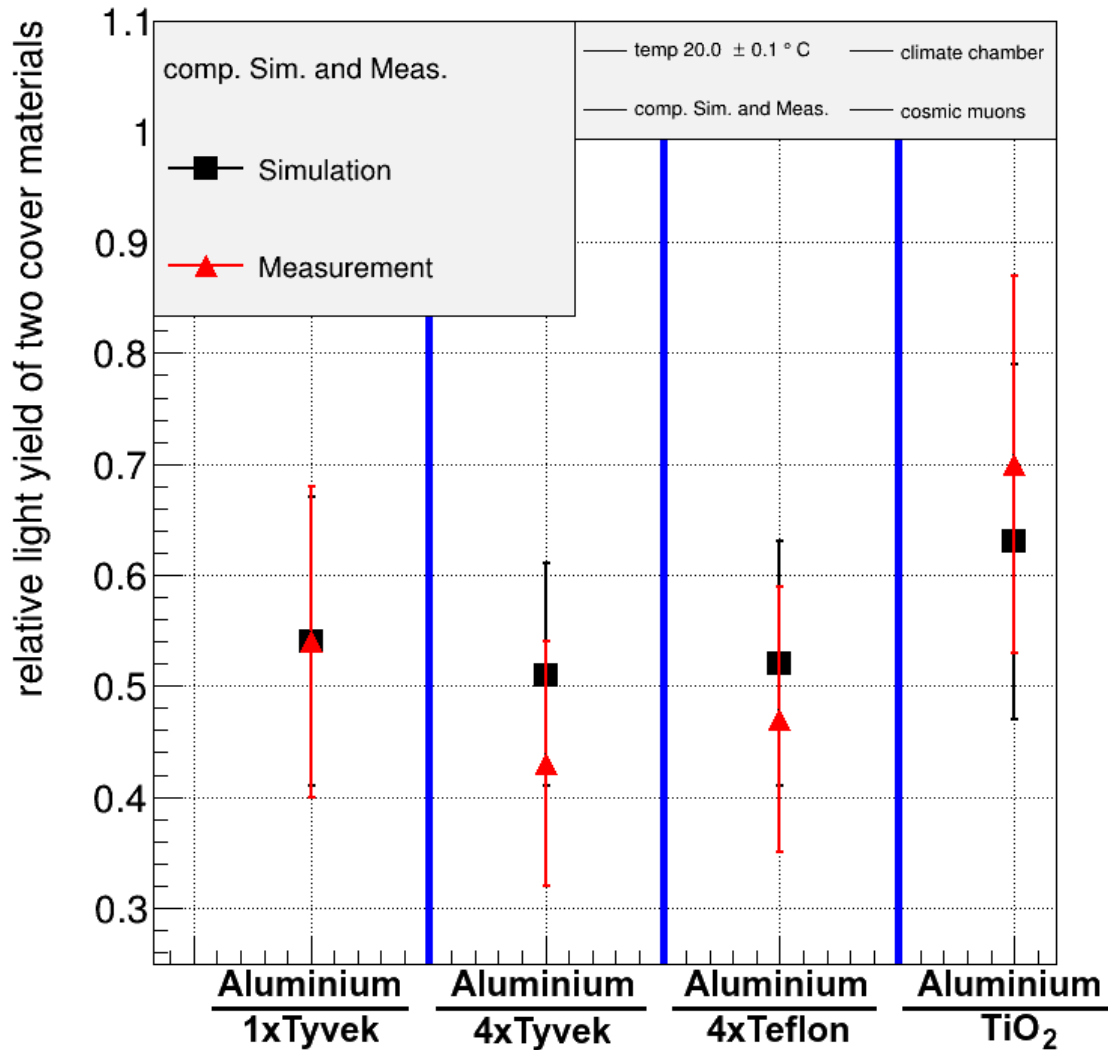


Figure 54: Relative light yield of different cover materials for channel 0 and a trigger in the middle position. This value is lowest for aluminium and a Tyvek multilayer, meaning that a wrapping with a multi layer of Tyvek provides the highest light yield.

Results of the other three channels can be found in tables 19 - 22 in appendix B. The behavior is analogous to channel 0.

As already indicated by the choice of the reflectivities, listed in table 9, the relative light yields of the simulation follow the measured data: a multi layer of Tyvek provides the highest light output and the TiO_2 paint the lowest light output of the diffuse reflective coverings. In the cases, where the simulation provides a higher light yield than the measurement, the light output of the diffuse reflective cover is too low in the simulation, or the directed reflection provides a too high light yield. Still one can see a match between the data points within the errors. We use the standard deviation of the photon production as error. These ratios can be optimized, for example implementing regions at the surface where photons are absorbed due to scratches or micro cracks. The inclined wall of the trapezoid is cut by a machine, which can produce such micro cracks, invisible for the eye.

Another interesting point in figure 54 is the ratio of Aluminium and the TiO_2 paint. A change from directed reflection to diffuse reflection, keeping the reflectivity constant, enhances the light output by roughly 40%. This means, that diffuse reflected photons undergo more often a total reflection, resulting in a longer mean free path of the photons.

Since figure 54 gives only results for one trigger position we now have a look at all trigger positions but concentrate to the Aluminium foil and multi Tyvek cover and to channel 0.

We want to compare the position dependency of the light yield for measurement and simulation. This time we deal with absolute values of the light yield. Problematic is therefore in first place the different quantities of both methods. The simulation gives us the mean number of photons per incident muon hitting the readout channel, which is in the order of a few thousand. In the measurement we have the integrated charge over a certain time window, which is collected by the QDC and is in the double digit range. Of course, there is a conversion factor, with which one can get one quantity using the other one. This factor depends for example on the photon detection efficiency of the tube, which can be different for different tubes, or the gain of the tube adjusted by the bias voltage and the intrinsic gain due to geometry of the dynodes. Consequently we decided to normalize the simulation to the measurement with the trigger being on the left position. This means we calculate the ratio

$$f = \frac{\text{light yield}(\text{Sim}; \text{left}; \text{Ch}0)}{\text{light yield}(\text{Meas}; \text{left}; \text{Ch}0)} \quad (7.2.5)$$

We get the following conversion factors for Aluminium and a Tyvek multi layer:

$$\begin{aligned}
 f_{Aluminium} &= \frac{2816 \pm 439}{39.3 \pm 6.7} = 71.7 \pm 17 \\
 f_{4 \times Tyvek} &= \frac{4141 \pm 547}{79.3 \pm 11} = 52.2 \pm 10
 \end{aligned}
 \tag{7.2.6}$$

In theory these factors should be equal. In our case they are not equal, because the simulations do not fit the measurement perfectly. To see the correlation between the conversion factors and the ratio of the light yields for measurement and simulation, we calculate the ratio of the conversion factors:

$$\frac{f_{Aluminium}}{f_{4 \times Tyvek}} = \frac{\frac{\text{Meas}}{\text{Sim}}(Alu)}{\frac{\text{Meas}}{\text{Sim}}(4 \times Tyv)} = \frac{\frac{Alu}{4 \times Tyv}(\text{Meas})}{\frac{Alu}{4 \times Tyv}(\text{Sim})}
 \tag{7.2.7}$$

The ratio of the conversion factors equals the ratio of the relative light yields of Aluminium foil and multi Tyvek and their corresponding simulations. This proves the assumption that the difference in the conversion factors are due to the deviation of the simulation.

We now use the conversion factors to normalize the simulation data for the trigger in the mid and on the right. Figure 55 shows the light output dependency for Aluminium foil and the Tyvek multi layer cover.

One can clearly see that the curves of the light output of the simulation fits to the measurement.

Still one can argue that this plot is artificial, since the conversion factors are calculated such that the corresponding curves match each other. We therefore take the simulation, we claim to describe the aluminium cover, and try to normalize it to the multi layer of Tyvek cover and vice versa. The calculated conversion factors for these cases are

$$\begin{aligned}
 f_{4 \times TyvekSim \leftrightarrow AluMeas} &= \frac{4141 \pm 547}{39.3 \pm 6.7} = 105 \pm 23 \\
 f_{AluSim \leftrightarrow 4 \times TyvekMeas} &= \frac{2816 \pm 439}{79.3 \pm 11} = 35.5 \pm 7.4
 \end{aligned}
 \tag{7.2.8}$$

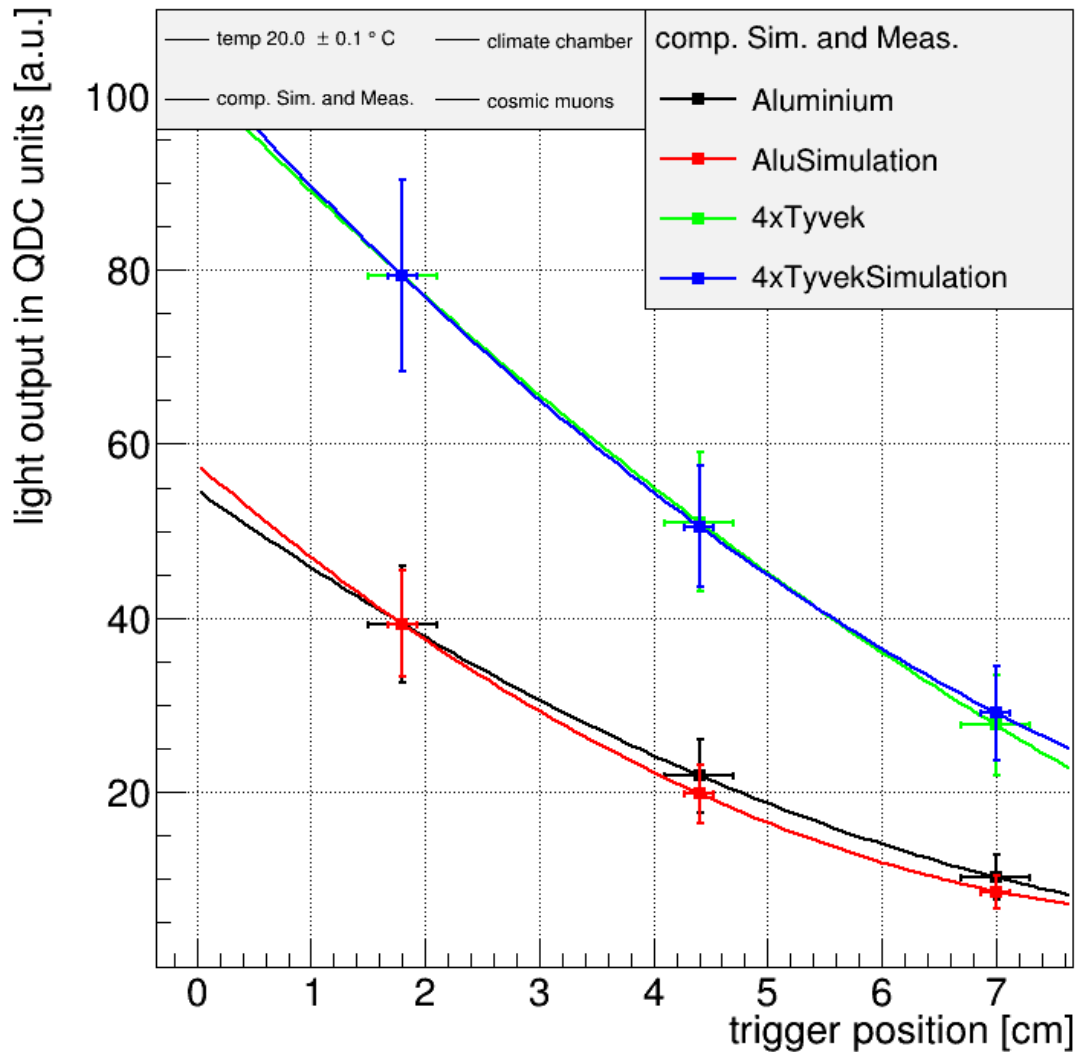


Figure 55: Light yields for an aluminium and a multi Tyvek cover compared to the corresponding simulations for channel 0 and all trigger positions. A polynomial of second degree is fitted to the data for a better visualization. The light yields of the simulation are normalized to the corresponding measurement, such that the left trigger position has the same light yield for measurement and simulation.

The ratio of these conversion factors is worse than it is for the "correct" factors of equation 7.2.6. According to equation 7.2.7 this is a first indicator, that this combination of simulation and measurement leads to bad results. The second indicator gives figure 56, where we plot the light yield curves for measurement and simulation but this time with the conversion factors of equation 7.2.8.

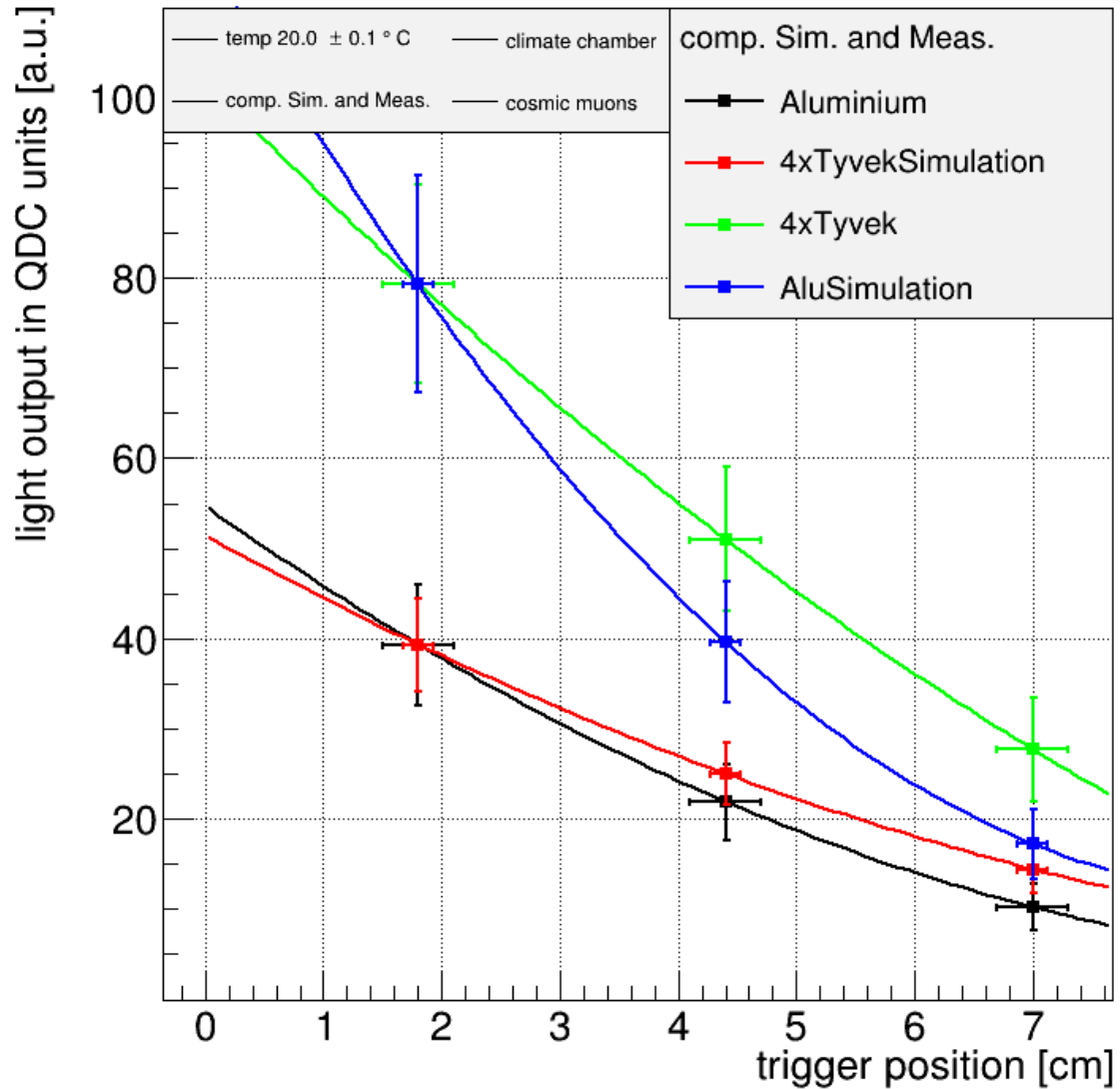


Figure 56: Light yields for an aluminium cover compared to the simulation corresponding to the Tyvek multi layer measurement and vice versa for channel 0 and all trigger positions. A polynomial of second degree is fitted to the data for a better visualization. The light yields of the simulation are normalized, such that the left trigger position has the same light yield for measurement and simulation.

One can see, that the shape of the curves for measurement and simulation do not match. It is therefore not possible to normalize an arbitrary simulation to the measured data.

For the multi Tyvek cover material measurement, green curve in figure 56, the data points of the simulation, blue curve in figure 56, are below the measured data points²¹. This means, that in the simulation the number of photons arriving at channel 0 drops too fast with the trigger moving to the right. The correlation between the light yield and the distance of the photon production place to the readout channel is therefore not well described by the simulation. An analogous conclusion can be drawn with the aluminium measurement in figure 56, which results in too many photons arriving at channel 0 in the simulation.

In contrast to this wrong assignment of simulation and measurement, we see a good agreement between measurement and simulation in figure 55, where we plot the correct assignment.

Summarizing this chapter one can say, that the parameters listed in table 9 are suitable to describe the results of the measurement of section 7.1. In the next sections we use the parameter of the multi layer of Tyvek cover material to simulate new fiber positions and trapezoidal geometries, since we want to use this cover in the next prototypes.

²¹The data points for a trigger on the left position are by definition of the conversion factor, equation 7.2.5, equal, not matter which simulation one compares to the measurement.

7.2.2 Fiber Position

In this section we want to present the results of the simulation with two new fiber positions for the trapezoidal scintillator. We simulate the five fiber positions of the prototype investigated at CERN, shown in green in figure 57, and two additional fibers, which are located at the edge of the scintillator as shown in red in figure 57.

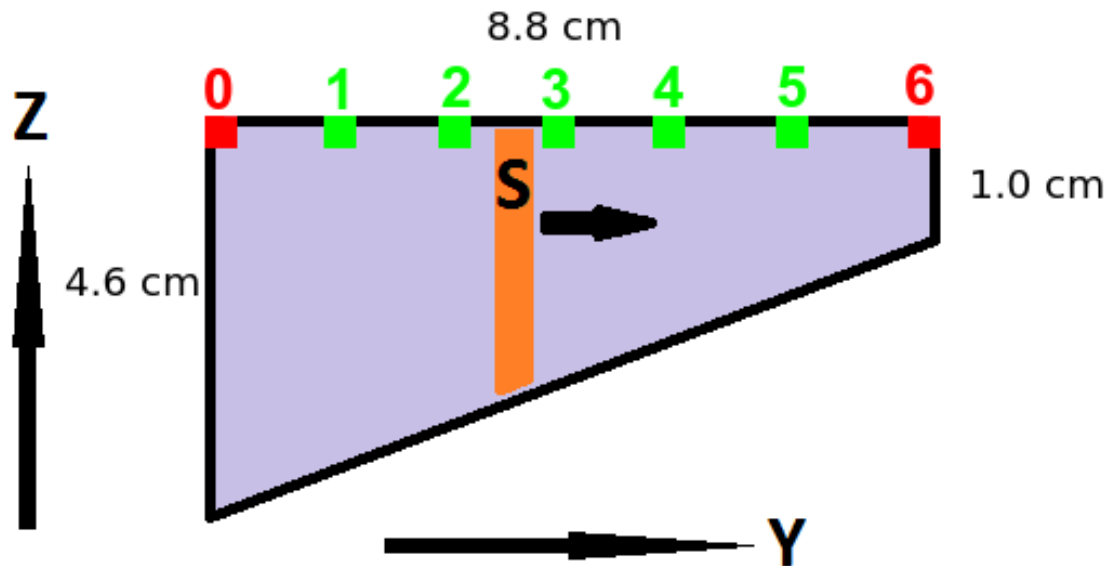


Figure 57: Scheme of the positions of the fibers in the simulation. The fibers of the first Prototype are sketched in green and the two new fibers are painted in red. The orange bar represents the area for allowed muon trajectories by the trigger.

As a motivation of the two new fiber positions one has to have a look at figure 58. This figure displays a scintillator, which contains only the five fibers present in the prototype of the CERN test beam. If the scintillator is wrapped in a diffuse reflective cover, the edges show an increased amount of photons compared to rest of the detector. This cover reflects the incident photons uniformly in every direction, meaning, that the photon density is constant for equal solid angles. Figure 59 shows a sketch for two cones with the same solid angle.

The projection of each cone on the wall results in a larger area for the upper (red) cone. As a result, if the cone is closer to the edge, the density of photons in the projection area is higher.

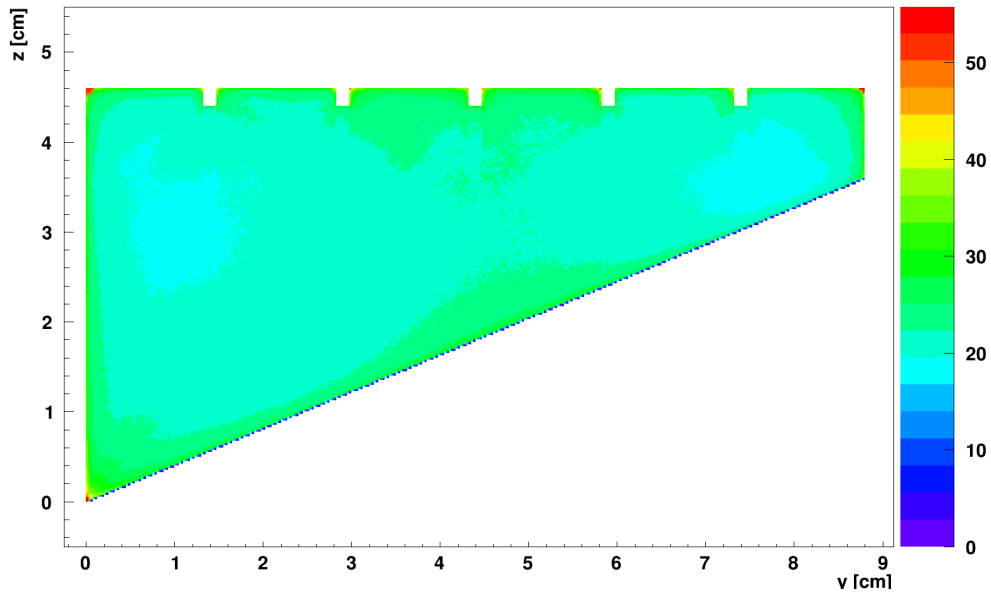


Figure 58: Hitmap of one scintillator wall. The edges of the wall show high photon concentration (red bins).

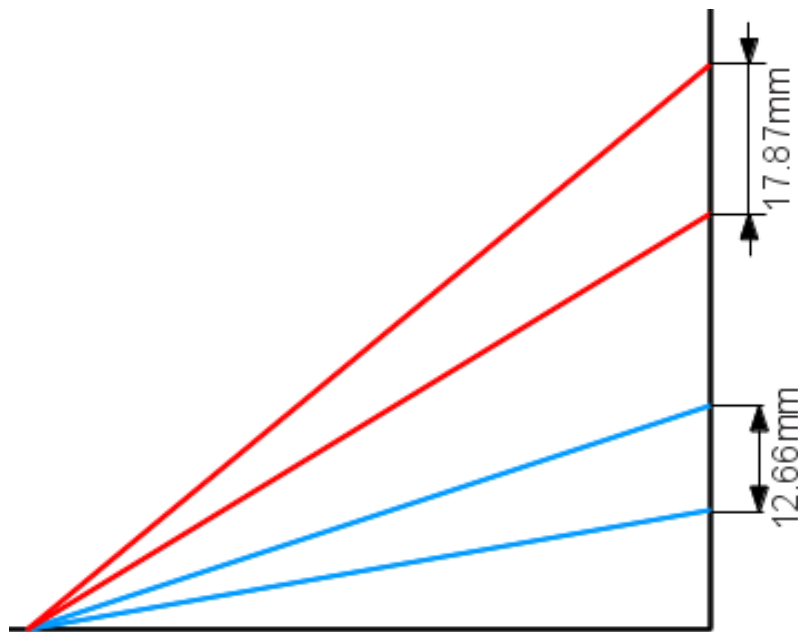


Figure 59: The red and blue lines define a cone of the same angle. The projection of the cone on a wall results in a larger projection area for the red cone than for the blue one.

Also, like at the test beam at [CERN](#), we use a $5 \times 5 \text{ mm}^2$ trigger area and move it in 5 mm steps across the scintillator in y -direction, as shown in figure [57](#). In x direction the trigger was set to be in the middle of the detector: $x_{trigger} = \frac{1}{2}X_{scin} = 7.5 \text{ cm}$. The rest of the dimensions are the same, as shown in figure [57](#).

For each of the seven fibers we calculate the mean number of detected photons over all muon events by fitting a Landau distribution to the distribution of collected photons, see figure [60](#).

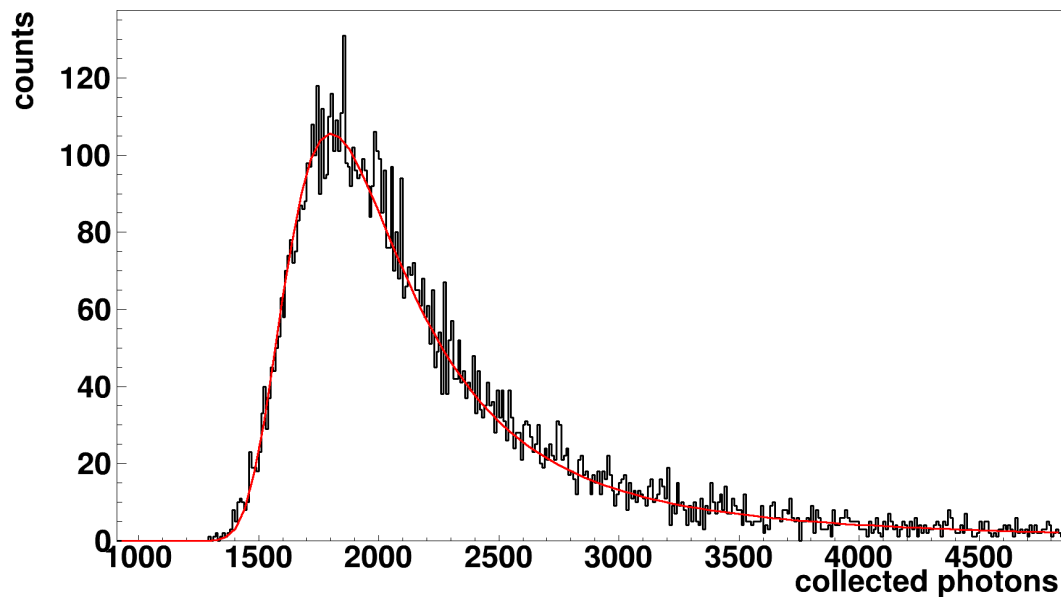


Figure 60: Distribution of collected photons in channel 0 during a simulation for a trigger in the center of the trapezoid.

We now take the calculated means of the distributions and superimpose them for all channels in a graph. The result can be seen in figure [61](#).

When the muon beam is close to the fiber, the number of counted photons increases. For a position determination these peaks are bad. For example the green curve in figure [61](#), representing channel 2, shows for a trigger at $y = 2.0 \text{ cm}$ approximately the same number of counted photons as the for $y = 3.5 \text{ cm}$. We conclude that having only the amount of photons we can just say, that the muon was somewhere between $y = 2.0 \text{ cm}$ and $y = 3.5 \text{ cm}$. In contrast to this, Channel 0 show a monotonous behavior over the whole detector.

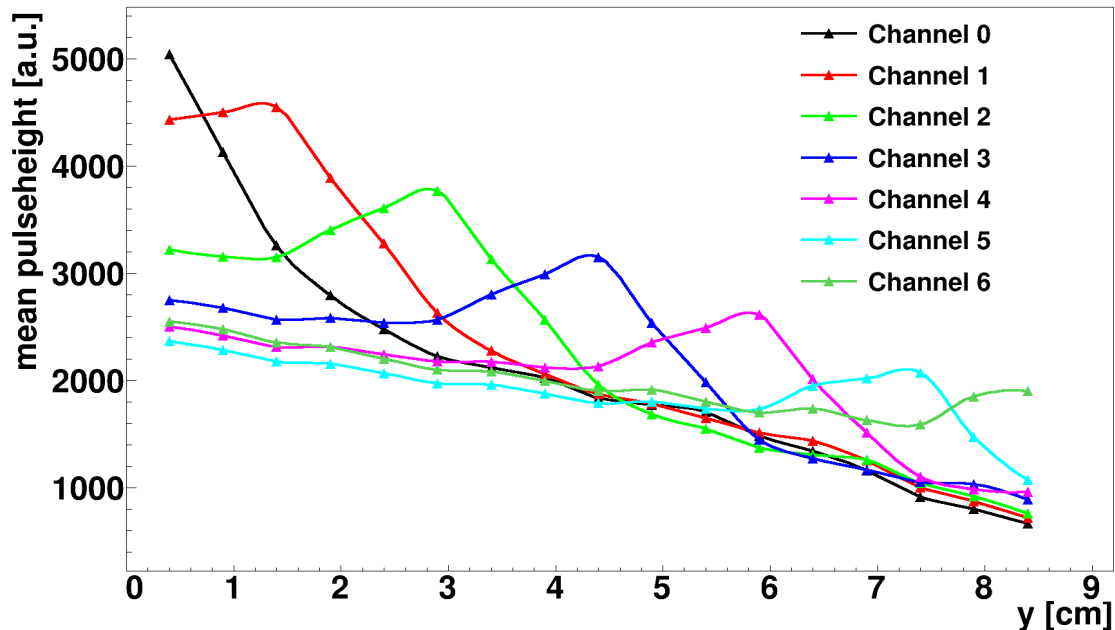


Figure 61: Mean amount of photons per fiber during a scan of the detector in y -direction. The measured points are connected with a smooth line to guide the eye.

We remember, section 2.4, that the energy loss of muons depends on their path length in the scintillator, the particle energy and the Landau distributed energy loss. Since we calculated the average photon production of 10^4 muons per measurement point, the measurements contain approximately the same amount of interactions with a high photon production for all trigger positions. Therefore we can assume, that the dependency of the calculated means is independent of Landau distributed energy loss. Since we do not simulate a variation in the particle energy, the given results do not depend on them. From the former sections we also know, that the light collection of a readout channel is correlated to the distance between photon source and readout channel.

The effects of the path length and the distance interfere destructively for channel 6 over the whole detector range. Therefore this curve is flatter than the other ones. This means that the dependency of the muon's position for this channel is weaker.

We assume, that it could be possible to use this channel to calculate the energy loss due to the Landau distribution for a single muon. If, as an extreme case, the

light output of a readout channel is totally uncorrelated to the beam position, a variation in the pulseheight can only be caused by the Landau distributed energy loss. An average value for the light production can be defined and compared with the actual pulseheight. We therefore can perform a normalization and apply it in the position sensitive channels, where we are left with an information, that is just depending on the path length of the muon in the scintillator and the distance between photon source and readout channel. If the position dependence of channel 6 is small enough to use it as an indicator of the energy loss by the Landau distribution has to be proven in the future.

Looking at channel 0, we see a fast decreasing of the signal in the first few centimeters of the detector, which then flattens. Such a monotonously decrease is the required behavior to a position sensitive readout channel and we will refer our next results to this channel. Currently we built a new detector, where this behavior should be proven, experimentally.

To further increase the position sensitivity of channel 0, one could think about optimizing the trapezoidal geometry. This was done with our simulation and will be reported in the next section.

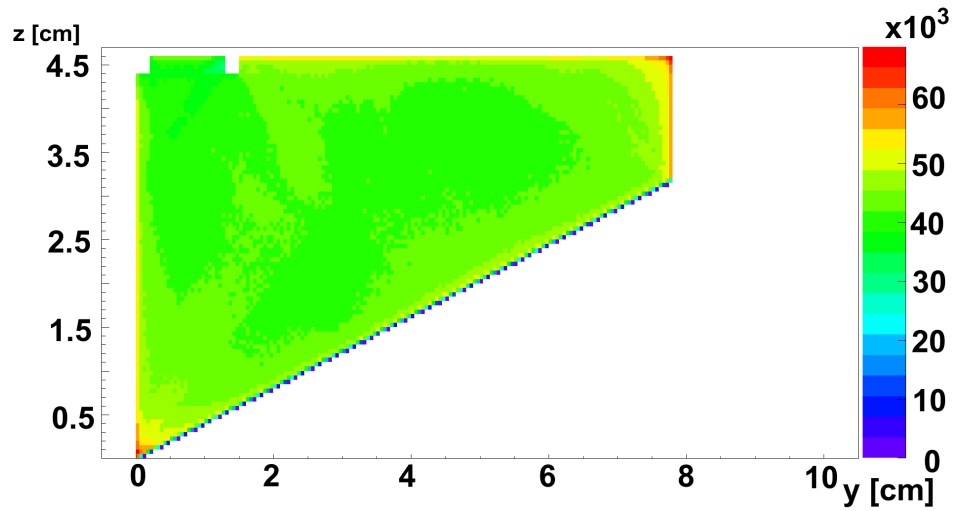
7.2.3 Detector Geometry

One result from the "CERN prototype" is a low light yield, if the beam is on the opposite side of the trapezoid as the readout WLSF, see section 6.2. This effect is more intense if the beam was at the thin side and we read out the channel at the broad side as already displayed in figure 52. A similar behavior can be seen in figure 61. Here the light output decreases by a factor of five, when the source is at the thin side and we look at channel 0. We expect a decreasing factor of roughly 4.6, which is the ratio of the thickness of the trapezoid at the broad and at the thin side. This difference is again a result of the distance correlation between photon source and photon detection. Additionally this decreasing is not linear and we therefore investigate a simulation run with different detector geometries, to find a case with a linear decreasing. As in the previous section we use simulated fibers to read the detector out.

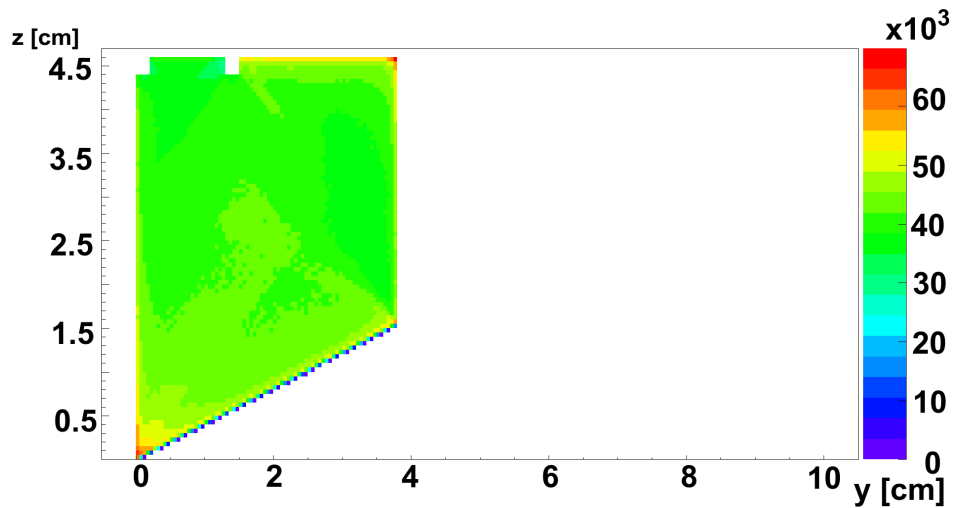
Since we recycle OPAL scintillators we are restricted in the possible geometries, we can realize. These scintillators have a length of $X_{scin} = 250\text{ cm}$, a width of $Y_{scin} = 8.8\text{ cm}$ and a height of $Z_{scin} = 4.6\text{ cm}$. We are limited in the x range due to facilities, like the cutting machine, which sets an upper limit of 70 cm . This is currently by far long enough, but in y and z the first prototype was as large as possible and it makes only sense to simulate smaller geometries.

In the following two runs we set X_{scin} in the simulation to 15 cm . In figure 61 one can see the flattening of the decreasing shape for channel 0 with an increasing distance to the trigger. One can think about, if it is possible to "cut" away this flat part of the curve by shorten the scintillator in y direction. To answer this question we investigated two possibilities to shorten the scintillator. In the first one, we continuously cut the given structure of figure 57 parallel to the $x - z$ plane. After each cut the scintillator is 1 cm smaller. The final scintillator has a width of $Y_{scin} = 3.8\text{ cm}$. We implement only the fibers for channel 0 and channel 1, since they are present in all geometries and show the best position resolution in figure 61. A fiber at the edge of the thin side, which will possibly be used to handle the Landau distributed energy loss, is not simulated, since we want to concentrate just to the light output enhancement of the position depending readout channels.

As an illustration of the new geometries figure 62 displays hitmaps of three width measured during this run.



(a) Cut at 7.8 cm.

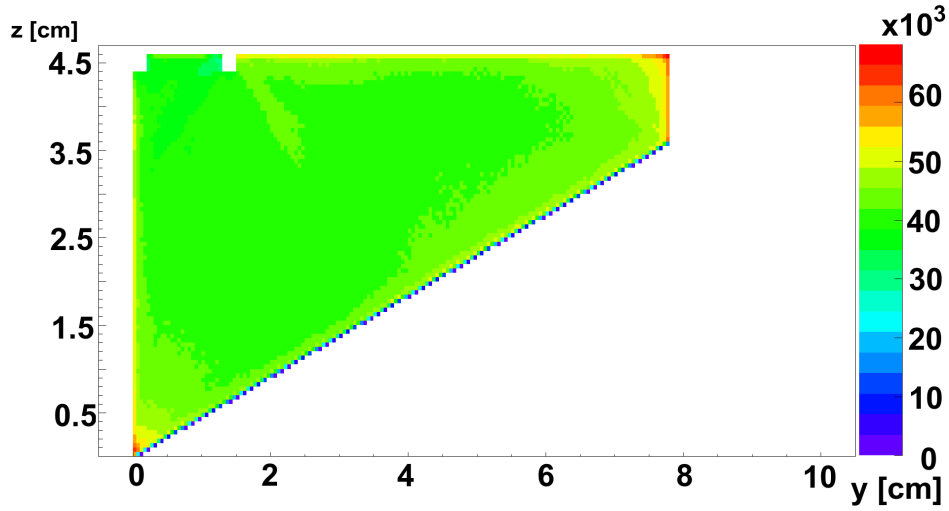


(b) Cut at 3.8 cm.

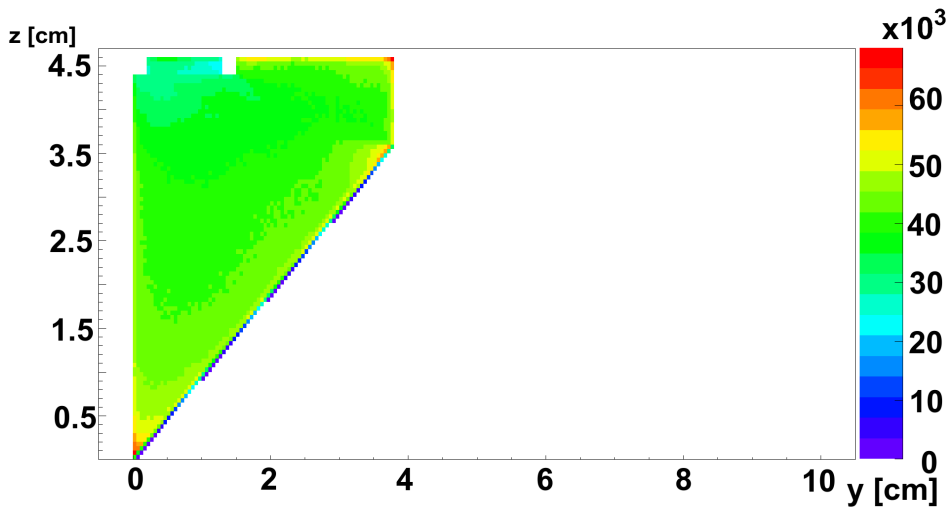
Figure 62: Two examples of the cut study: 62a: $Y_{scin} = 7.8 \text{ cm}$, 62b: $Y_{scin} = 3.8 \text{ cm}$.

Another possibility would be to compress the scintillator, meaning, that one keeps the height of the scintillator at the thin side constant. This is done again in steps of 1 cm with a minimal scintillator width of $Y_{scin} = 3.8 \text{ cm}$. Figure 63 shows hitmaps for compressed trapezoids.

One can see again in all hitmaps of figures 62 and 63, that the edges of the scintillator show an increased amount of photons, which results from the diffuse reflective cover material used in this run, as in section 7.2.2.



(a) Compression until 7.8 cm.

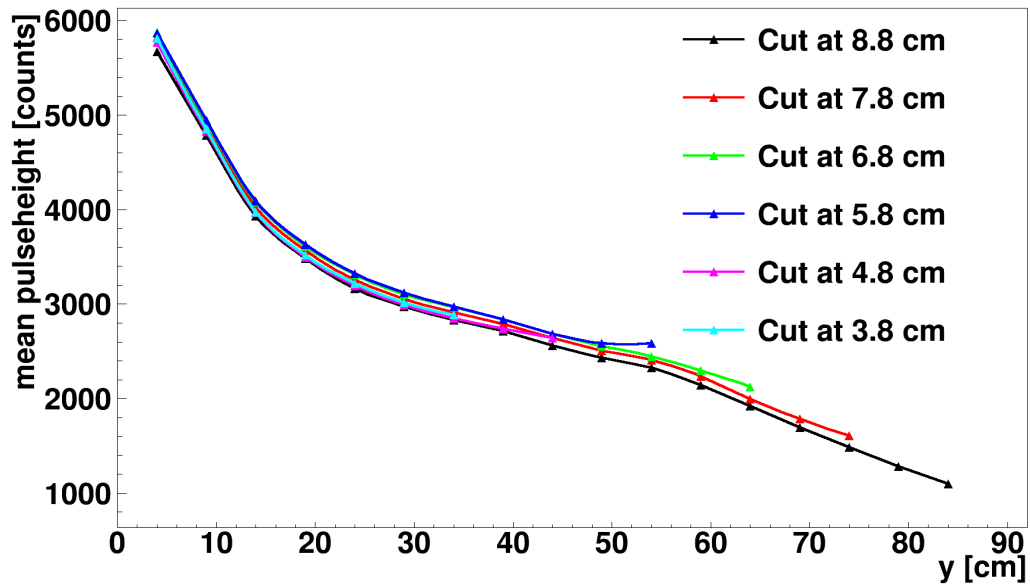


(b) Compression until 3.8 cm.

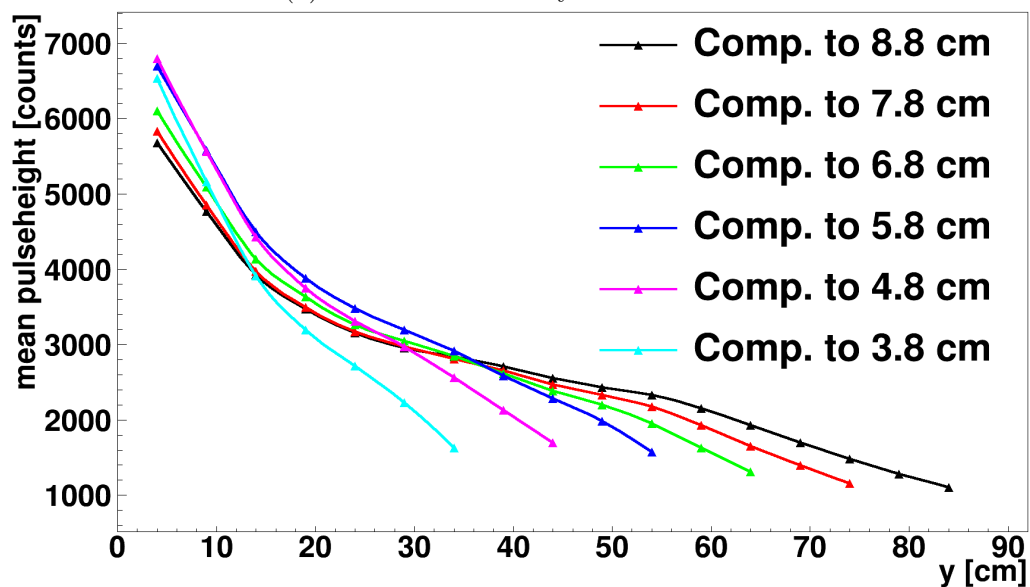
Figure 63: Two examples of the compression study: 63a: $Y_{scin} = 7.8 \text{ cm}$, 63b: $Y_{scin} = 3.8 \text{ cm}$.

We start the discussion with channel 0 since we assume, that it has the best position resolving properties. We again move the $5 \times 5 \text{ mm}^2$ trigger area in 5 mm steps from the broad side to the thin one. The results of both studies can be seen in figure 64.

In both cases we see, that it is possible to cut away the flat part of the curve, without any negative effect on the steep part.



(a) Result of cut study for channel 0.



(b) Result of compression study for channel 0.

Figure 64: Results for the studies with both methods to shorten the trapezoid for channel 0.

For the case of a cut trapezoid the curves in figure 64b show, that the flat part is cut away and the rest of the curves stay constant. This still means, that we are left with a visible transition from the steep decrease in the beginning to a

moderate decrease in the end.

In contrast to this, the compression study result in a trapezoid, where there is a steep rise over the whole detector. We assume, that this would increase the position resolution of the detector, since there is now a clear position depending photon collection for channel 0, correlated to the beam position. Additionally we find, that the photon collection per unit path length of the muon increases: If the trigger is at the broad side of the scintillator, the path length of the muon are approximately equal for all geometries and the photon collection increases by 10%. For the thin side one has to look at the data points with the largest y coordinate. In this case the mean amount of collected photons per muon event increases from $1.1 \cdot 10^3$ for a trapezoid with $Y_{scin} = 8.8 \text{ cm}$ to $1.6 \cdot 10^3$ for the small trapezoid with $Y_{scin} = 3.8 \text{ cm}$. We explain this behavior with the mean free path of the photons. In a smaller trapezoid a photon has to travel a shorter distance to the readout channel and the chance, that it is absorbed before it is detected is less than it would have to travel a long distance.

We can now finally compare the smallest trapezoids for the cut and the compression study. Figure 65 displays the graphs for both studies.

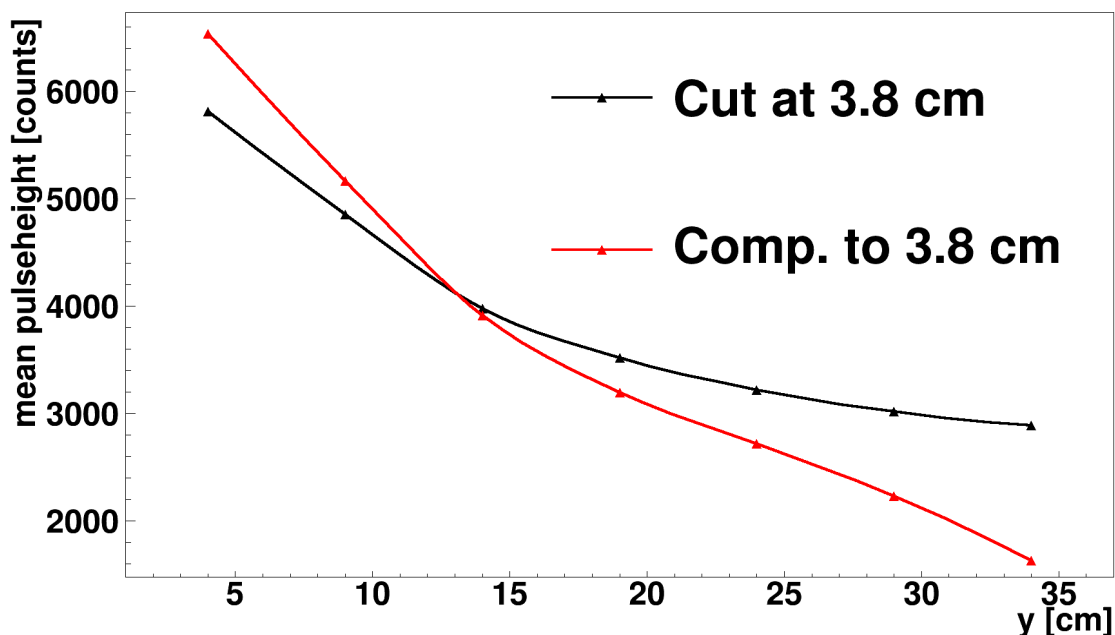


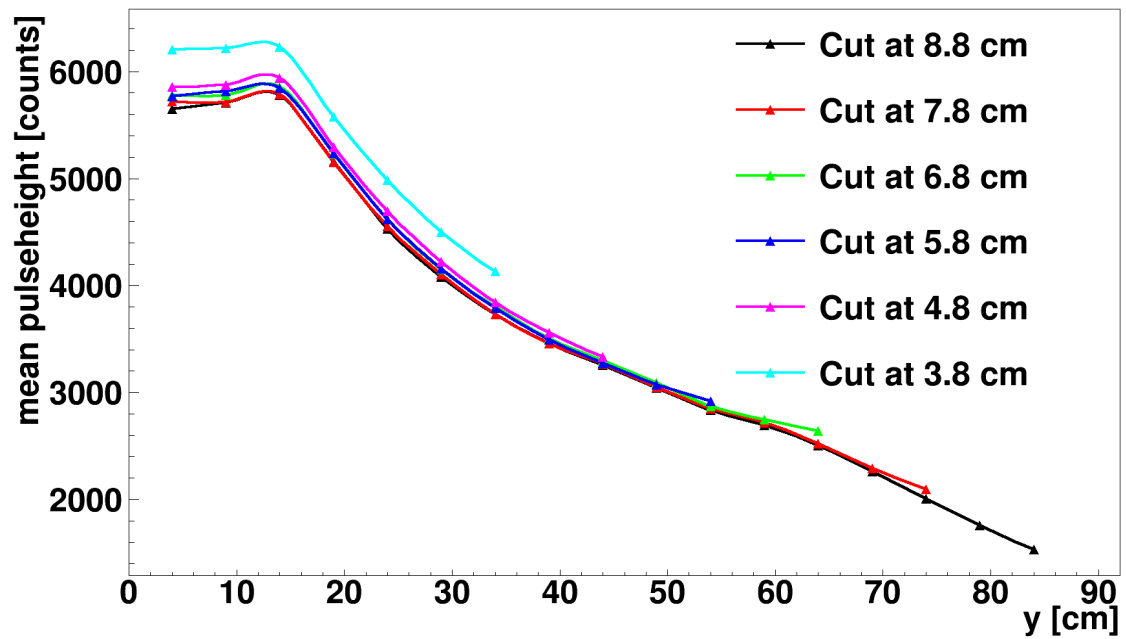
Figure 65: Cut and the compression study for channel 0 and $Y_{scin} = 3.8 \text{ cm}$.

While the decrease of the collected photons with a decreasing path length of the muon is steep for a compressed trapezoid, it is flat for a cut trapezoid. We assume, that readout channels with such a steep decrease have good position resolving properties. Still there might be an advantage for the flat decrease. The "CERN prototype" showed a light response of the order of two photons per event, if the beam was at the thin side and we read out at the broad side, see figure 44. This low light yield results from a combination of the large distance between the beam and the WLSF and from short tracks in the scintillator. Looking at figure 65 we see, that the number of collected photons is higher for a cut trapezoid when the trigger is at the thin edge. We could reach a better position resolution due to the steep decrease for a compressed detector but a possible low light yield would ruin this achievement. This has to be checked experimentally. If this occurs in reality, we prefer the cut trapezoid, since it is a compromise of a good position resolution and a high light yield for tracks through the thin side.

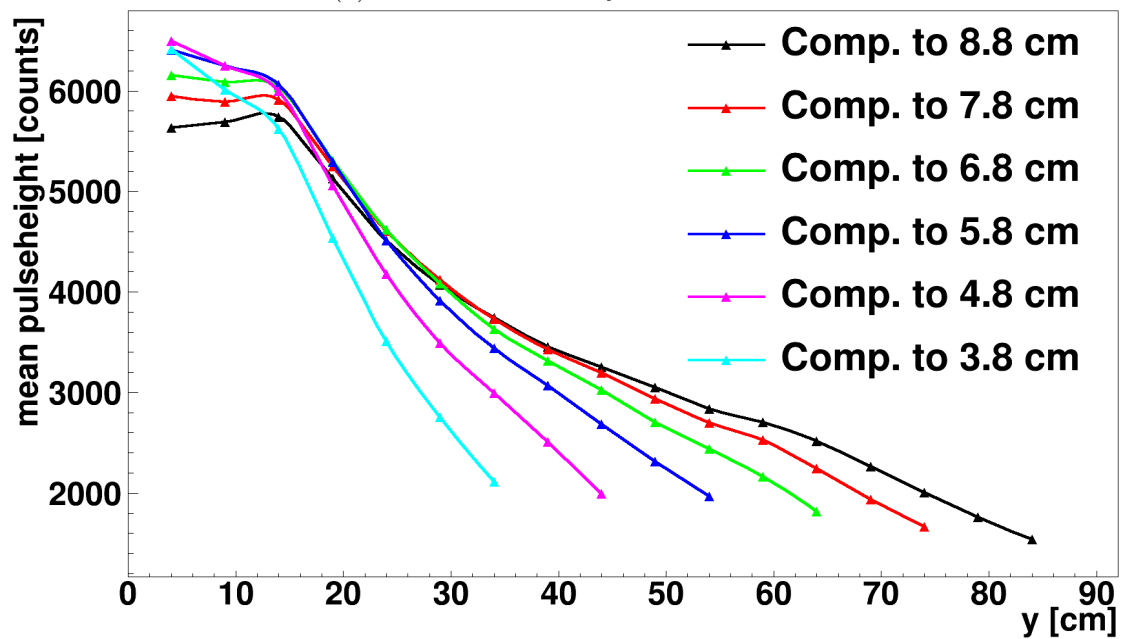
In figure 61 we see peaks for all channels, if the trigger is next to them and conclude, that this behavior is not ideal for a good position resolution. We will now have a look at channel 1 and study the effect of the peak within a smaller trapezoid. The result for the cut and the compression study for channel 1 can be found in figure 66.

In the case of a cut trapezoid, the shape of the peak is visible for every step of the cutting process. The fact that the peak for $Y_{scin} = 3.8\text{ cm}$ is much larger compared to the rest of the shapes in figure 66a can be explained due to a optimized geometry for this channel position. The channel is located approximately in the middle of the detector and the detector is small which results in a high collection of photons reflected by walls. For example as shown in figure 63b the right wall is closer to the channel and according to the explanation of figure 59 the photon density is higher.

For the compressed trapezoid, figure 66b, we see, that the peak vanishes for smaller trapezoids. The peaks are explained by the distance correlation of the trigger position and the readout channel. For the compressed trapezoid the effect of the path length of the muon and the resulting amount of produced photons is more dominant than the effect of the distance correlation, because the path length drops much faster due to the higher inclination of the tilted wall.



(a) Result of cut study for channel 1.



(b) Result of compression study for channel 1.

Figure 66: Results for the studies with both methods to shorten the trapezoid for channel 1.

Consequently we now compare the two methods of making the trapezoid smaller for the smallest simulated trapezoid, $Y_{scin} = 3.8\text{ cm}$. For this purpose we superimpose the graphs for both methods and show the result in figure 67.

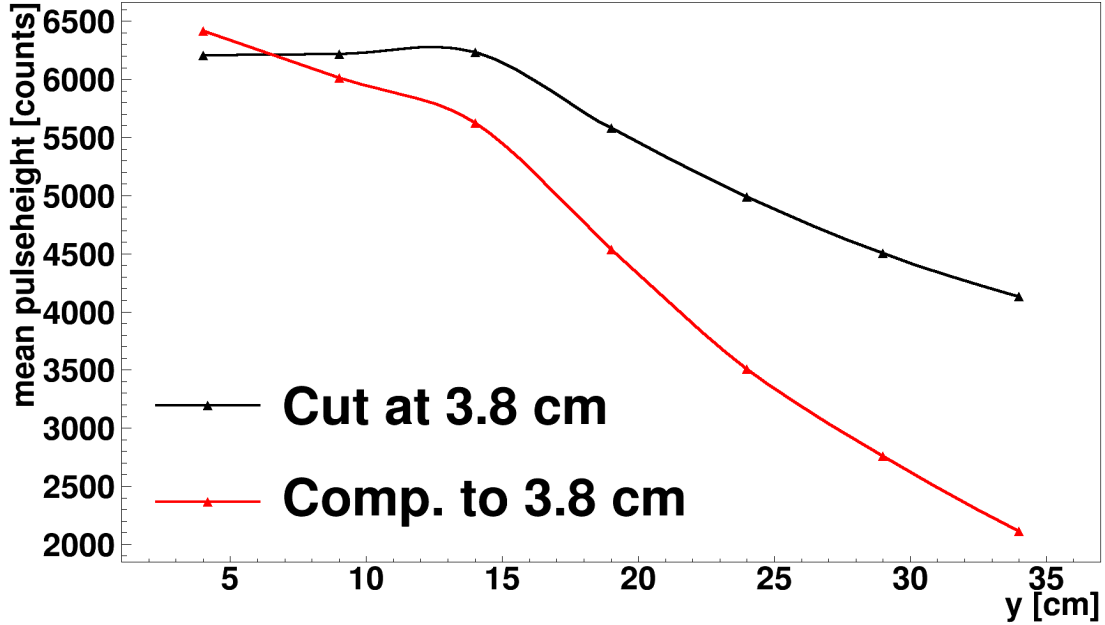


Figure 67: Comparison of the cut and the compression study for channel 1 and $Y_{scin} = 3.8\text{ cm}$.

The result is basically the same as for channel 0, see figure 65. The compressed scintillator provides a steep decrease of photons over the whole detector range, while channel 1 in the case of a cut trapezoid collects more photons, inter alia because more of them are produced. The case which fits best to our requirements finally needs to be determined in an experiment.

There are also arguments against a shorter trapezoid which were not covered by this simulation. In the case of a smaller trapezoid we would increase the number of readout channels compared to the active area of a detector module. Additionally the OPAL scintillators have a width of $Y_{scin} = 8.8\text{ cm}$ and shortening would mean to cut away scintillator material and thus damaging the surface of the scintillator.

Finally we can say that a smaller trapezoid will improve the position resolution of the detector and which method we use to shorten the trapezoid or if we take the original width must be tested experimentally. The simulation suggests to use a

compressed scintillator if the number of detected photons are high enough, which may be the case after using the multi layer of Tyvek cover material, having the readout channel in a corner of the trapezoid and taking care of the fiber routing.

8 Position Determination Techniques

As mentioned in section 7.2, we can also simulate a double layer structure of trapezoids. With this tool we can search for channels or combinations of channels in the upper and lower layer, which provide a suitable position dependency for a use with equation 5.2.5. The simulations before show for example, that channel 6, a fiber at the edge of the thin side, has over a wide range of the scintillator no position resolution at all. Using this channel or a combination of this and other channels in equation 5.2.5 would not make much sense, but Ch 0 provides a promising shape.

For this simulation we use a double layer of scintillators each with dimensions listed in table 10.

X_{scin}	15.0 cm
Y_{scin}	8.8 cm
Z_{scin}	4.6 cm
Z_{thin}	1.0 cm

Table 10: Dimensions of the trapezoid used in the position resolution simulation.

Figure 68 shows a hitmap of this simulation, in which one sees the double layer structure and the distribution of the interactions of photons with a wall of the scintillator.

Each scintillator has seven grooves as displayed and labeled in figure 57. The channels of the lower trapezoid are also labeled from left to right, meaning that Ch 7 is the one on the thin side and Ch 13 is at the broad side. We perform a scan along the y coordinate with a trigger area of $5 \times 5\text{ mm}^2$ moving the trigger in 5 mm steps.

As before we use the channels at the broad sides, Ch 0 and Ch 13, and plug their integrated photons into equation 5.2.5. The result is shown in figure 69.

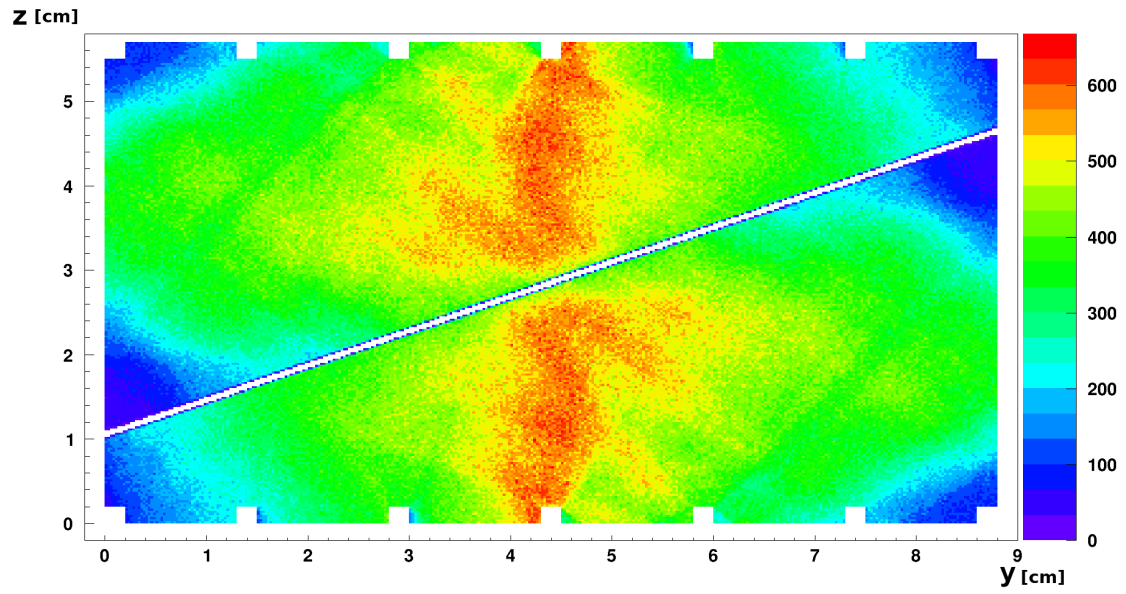


Figure 68: Hitmap of the double layer structure. The trigger is at $y = 4.4 \text{ cm}$ in this case.

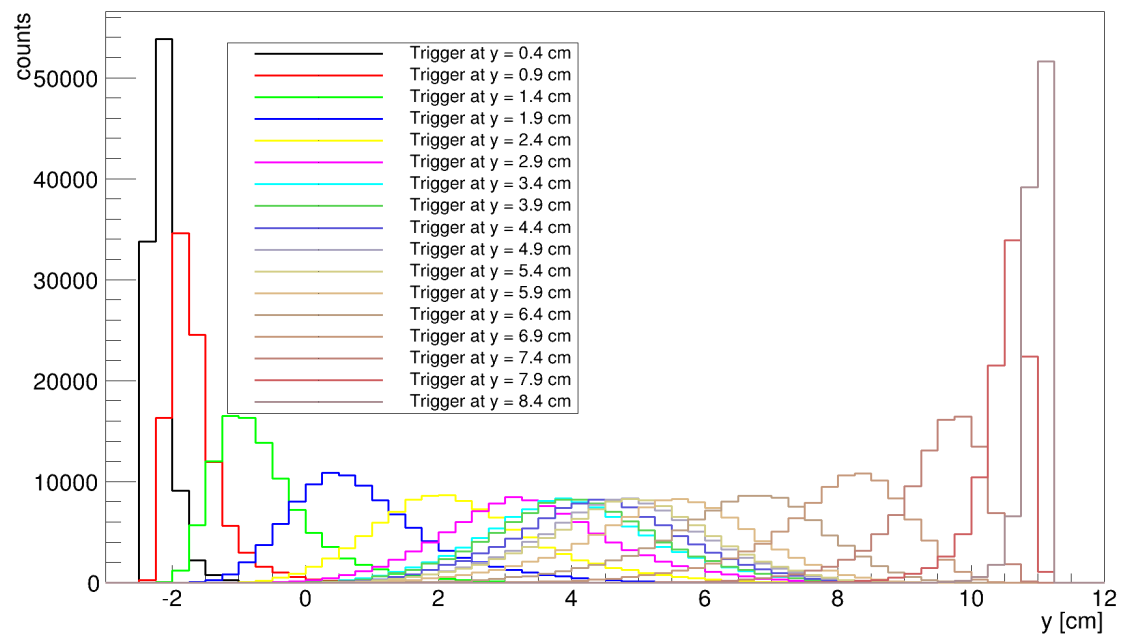


Figure 69: Reconstruction of trigger position in y direction with Ch 0 and Ch 13 according to equation 5.2.5.

This procedure predicts again a muon position outside the detector for certain trigger positions. This effect can be explained again by the correlation between the light yield in a readout channel and the distance from the photon production place to the fiber. The fraction $Q = \frac{q_1}{q_1+q_2}$ in 5.2.5 is proportional to the fraction of the path length of the muon in the scintillator. But what Ch 0 measures is not the total light production in the upper trapezoid, but rather a convolution between the light production of the muon and a distance correlation between the muon track and the fiber. If one, for example, has an equal amount of photons produced at the broad and at the thin side, Ch 0 would see more light, if the beam is at the broad side of the upper scintillator, because then the beam is much closer to the fiber. For our case we insert the ratio $Q = \frac{Ch\ 13}{Ch\ 0 + Ch\ 13}$ in equation 5.2.5. Taking the case of the black curve in figure 69, a trigger at $y = 0.4\text{ cm}$, contains on the one hand a long path of the muon in the scintillator for Ch 0 and as well as a close distance between the fiber and the trajectories, but on the other hand a short path for the muons and a long distance between fiber and trigger for Ch 13. We therefore expect a large amount of photons in Ch 0 and a small amount of photons in Ch 13 resulting in a very small value of Q . This is exactly what we see in figure 69. It is therefore necessary to quantify this effect and include it in the analysis.

Another problematic behavior is the fact, that we see a lot of distributions overlapping in the mid of the detector. This property should also vanish after including the mentioned distance effect in the analysis.

Summarizing we have to say, that we have to further study the mentioned distance correlation, in order to find a corrected analysis method and to look for other suitable channel combinations. We also can use this simulation to find ways to eliminate the dependency of the Landau distributed energy loss.



9 Conclusion and Outlook

Within this work we tested the two dimensional position resolving properties of a scintillating plastic detector for tracking of cosmic muons. The detector consists out of two optical insulated trapezoidal shaped scintillators. A muon passing the detector will produce a light pulse which is proportional to the path length in the scintillator. Comparing the pulseheights of the scintillation light of both layers and the arriving time of the signal at the silicon photomultiplier (SiPM), which are used to detect the light, we get an information where the muon has passed the detector. The detector will be used to determine the angle of deflection of muons due to multiple Coulomb scattering in an iron absorber. The track of the muon is predicted by highly resolving monitored drift tubess (MDT) and after wards compared to the position in the scintillation detector. The spread of deflection will be smaller with an increased muon energy and we can deduce the energy of the muon by calculating the deflection due to the iron absorber.

A test with a prototype detector took place at a beam time at CERN, where we investigated the scintillator with 120 GeV pions. We could show, that the trapezoidal shape of the detector can be used to determine the position of the penetrating radiation. The readout of the SiPMs was realized with a flash analog-to-digital converter (FADC), which recorded the signal shape of the SiPM-response. Therefore one can extract information about the pulseheight and the propagation time of the signal.

To obtain the position of the muon along the scintillator rod, we compared the time when the light pulse arrived at the left side with the time it took the light to arrive at the right side of the scintillator. We found a resolution of roughly 10 cm in this coordinate. We can therefore determine the energy of the muons with a maximum energy of 1 GeV. One possibility to improve this resolution will be the use of a readout device like a time-to-digital converter (TDC), which has a time resolution of 35 ps.

We determined the position of the pion track in the direction perpendicular to the scintillator rod by comparing the light yield of both scintillator halves. We achieved a resolution of 3 cm, which means that we can resolve the energy of muons up to 2 GeV.

To improve the resolution of the detector, we need to increase the light yield per

single muon event.

In a first step we searched for cover materials which result in a higher light yield. For the prototype detector we used aluminium foil. We tested the effect of four diffuse reflective cover materials on the light output of a scintillator wrapped in aluminium foil. The four materials are a single layer of Tyvek, a multilayer of Tyvek, a multilayer of Teflon and a paint based on TiO_2 . The two multilayer covers consist each of at least four layers of the cover. By using a cover consisting out a multilayer of Tyvek, the light yield could be enhanced by a factor of two, compared to aluminium foil. A problem with the TiO_2 paint is the fact that it is based on organic solvents, which reacts with the scintillator and therefore destroys its surface. We can test paints, which are water based, e.g. acrylic paints, and look, if we can further increase the light yield with a cover material, that is directly Attached to the surface. Additionally we have to investigate experiments with longer scintillators, since they may act differently under the use of a diffuse reflective cover [Saint Gobain, 2005].

For further studies we developed a Monte Carlo simulation of light propagation within a trapezoidal shaped scintillator, which was calibrated to the data of the cover measurement study. From this we found the following reflective properties of the cover materials

aluminium	directed reflection	$R_{cover} = 91\%$
$1 \times$ Tyvek	diffuse reflection	$R_{cover} = 93\%$
$4 \times$ Tyvek	diffuse reflection	$R_{cover} = 99\%$
$4 \times$ Teflon	diffuse reflection	$R_{cover} = 97\%$
TiO_2	diffuse reflection	$R_{cover} = 91\%$

Table 11: Parameters for the cover material in simulation, which provide the best agreement with the data.

With these properties we could reconstruct the measured data within the given systematic uncertainties. We then used the simulation to explore new fiber positions and new geometries of the trapezoid.

For the fiber position, we found that each fiber has a peak in its light output if the trigger is close to it. To avoid these peaks we tested fibers at the edges of the scintillator rod. A fiber at the edge of the broad side of the trapezoid showed a decreasing light output over the whole scintillator with a decreasing path length of the muon. But this decrease flattened while the trigger moved to the thin side. Another reason why we chose this position is the increased amount of photons reaching the edges of the trapezoid. For a fiber at the edge of the thin side, we found a constant light yield over a wide range of the scintillator. It just increased as trigger came close to this edge. We assume, that this fiber can be used to determine the correlation of the amount of produced photons to the Landau distributed energy loss of the muon. If it would be possible to cancel this dependency out of the final result, we can further improve the position resolution.

Another result from the fiber position study was the effect, that the amount of photons reaching the readout channel depended on the distance of the place where the photon was created to the readout channel. For large distances we saw a decreasing amount of photons and vice versa. For the readout channel at the broad side we have two constructively interfering effects. When the trigger is moved away from this channel, the scintillator gets thinner and therefore less photons were produced. Also the distance to the trigger increased and therefore even less photons arrived at this channel. For a channel at the thin side both effects interacted destructively. A hint on this effect could have been seen already in the study with the prototype detector at [CERN](#), but there it was less dominant due to the overall low light yield. We are now going to verify this result in an experiment and will further use to simulate other fiber positions like at the inclined wall of the trapezoid.

To decrease this effect we also studied possible new geometries with smaller trapezoids using the simulation. Here the path length for a photon to the readout channel is decreased. We investigated two different ways of making the trapezoid smaller. At first we take the geometry of the prototype detector and cut away step by step scintillator material of the thin side. In the second approach we compressed the scintillator, meaning that the inclined wall of the trapezoid got steeper, while the thickness at the thin side stayed constant.

With both methods we were able to eliminate the part of the light yield curve, where the decrease in light output flattened without any negative effect on the

steep part. For a compressed scintillator we saw a steeper decreasing of this curve than for the cut trapezoid. Such a steep shape was assumed to provide a good position resolution. But it also had the disadvantage of a low light yield for a trigger at the end of the thin side. If all other enhancements of the light yield will provide a sufficient high light yield we can neglect this disadvantage. We will investigate new prototype detectors, where we will see whether we can neglect this lower light yield.

At last we simulated a double layer of trapezoidal scintillators as we had in the prototype detector. With this run we wanted to study fiber position, which perform well for determining the position of the track of the muon perpendicular to the scintillator rod. We figured out, that a usage of both fibers at the broad side provided a good position resolution but since we neglect the mentioned distance dependency in the analysis, we end up with wrong and non physical results for the position of the muon. It is therefore necessary to quantify this effect and correct for it in the analysis to reconstruct the correct muon position. We also have to investigate more detailed studies on finding suitable combinations of readout channels and also methods, which can be used to calculate the effect of the Landau distributed energy loss.

Conclusively one can say that the basic concept behind this detector was proven and there are possibilities to further improve the position resolving properties.

List of Abbreviations

APD	avalanche photo diodes
BOS	barrel outer small
CERN	European Organization for Nuclear Research
CRF	Cosmic Ray Facility
DCR	dark count rate
$\varepsilon_{\text{Geiger}}$	efficiency to trigger an avalanche
$\varepsilon_{\text{geom}}$	geometrical efficiency
QE	quantum efficiency
FFunc	"Fermi function"-method
FADC	flash analog-to-digital converter
FPBT	"First-Point-Below-Threshold"-method
LHC	Large Hadron Collider
MIP	minimum ionizing particle
MDT	monitored drift tubes
NIM	Nuclear Instrumentation Standard
QDC	charge-to-digital converter
P_{cross}	crosstalk probability
PDE	photon detection efficiency
PMT	photomultiplier tube
Pos 0	Position 0
Pos 1	Position 1
Pos 2	Position 2

PSD	Pulse Shape Discrimination
SWFunc	"section-wise defined function"-method
SiPM	silicon photomultiplier
SPS	Super Proton Synchrotron
TDC	time-to-digital converter
V_{BD}	breakdown voltage
V_{bias}	bias voltage
V_{crit}	critical voltage
V_{over}	over voltage
WLSF	wavelength shifting fiber

1	Photograph of CRF	1
2	Scheme of CRF with new energy selector	2
3	Scintillation Light: one exponential	6
4	Scintillation Light: two exponentials	7
5	Polyvinyltoluene	8
6	Energy level	8
7	Scheme of wavelength shifting progress	10
8	Franck-Condon-Principle	11
9	Spectrum of BC 400	12
10	Bethe-Bloch	14
11	Landau Distribution	14
12	Scheme of a PMT	15
13	Scheme of a SiPM	16
14	PN junction	17
15	Pixel response curve	19
16	1x1 SiPM	21
17	3x3 SiPM zoom	21
18	3x3 SiPM zoom	22
19	Spectra for BCF 92	23
20	PDE for three SiPM types	24
21	Crosstalk probabilities	26
22	Scheme of a WLSF	30
23	SiPM on an amplification board	31
24	SiPM with FC-connector	32
25	SiPM signal	33
26	FADC Readout	34
27	QDC Readout	36
28	Oscilloscope Display	37
29	Schematic draft of the detector	39
30	Geometry for y -direction	43
31	Schematic sketch of the energy selector	45
32	Setup at CERN	47

33	Dimensions of prototype	48
34	Fitted Fermi function	50
35	Fitted section wise defined function	51
36	different VS same FADC	53
37	Run time difference FPBT	54
38	Run time difference FFunc	54
39	Run time difference SWFunc	55
40	x coordinate; way 1	56
41	x coordinate; way 2	56
42	x coordinate; way 3	57
43	Analyzed beam position of the y scan	59
44	Light output per channel	60
45	CERN Prototype - resolution in y direction	61
46	Cover measurement setup	64
47	Calibration curves of PMT	65
48	Ch0 fitted with Landau	67
49	Ch0 fitted with Landau zoomed	67
50	Result for cover materials by measurement	69
51	Light output of all channels for all trigger positions and multi Tyvek coating	70
52	Result of y scan measurement	71
53	Comparison of simulation and measurement by comparing light yields of Ch 0 and Ch 2	80
54	Relative light yield of different cover materials for channel 0	81
55	Light yields for an aluminium and a multi Tyvek cover compared to the corresponding simulation	84
56	Light yields for an aluminium and cover compared to multi Tyvek measurement and vice versa	85
57	Fiber positions in simulations	87
58	Hitmap of scintillator wall	88
59	Scheme of photon density	88
60	Distribution of collected photons during a simulation	89
61	Fiber response	90
62	Cut study with simulation	93

List of Figures

63	Compression study with simulation	94
64	Results for channel 0 with a shorter trapezoid	95
65	Cut and the compression study for channel 0 and $Y_{scin} = 3.8 \text{ cm}$. . .	96
66	Results for channel 1 with a shorter trapezoid	98
67	Comparison of the cut and the compression study for channel 1 and $Y_{scin} = 3.8 \text{ cm}$	99
68	Double layer in simulation	102
69	Trigger reconstruction in simulation	102
70	Orientation of simulation	XIV



1	Gaussian width of scatter for eight muon energies.	46
2	Offset values	52
3	Time differences	53
4	X coordinate	57
5	Dimensions of trapezoid for cover measurement	63
6	Coordinates in the $x - y$ plane of trigger center.	64
7	Parameters for cover measurement	66
8	Maxima of light output	68
9	Result for the identification of the correct reflection parameters in simulation.	79
10	Dimensions of trapezoid for position resolution Simulation	101
11	Result for the identification of the correct reflection parameters in simulation.	106
12	Simulation parameters	XIII
13	Result for the identification of the correct reflection parameters in simulation.	XIX
14	List of relative light yields for Aluminium and the simulation with a directed reflection and $R_{cover} = 91\%$	XIX
15	List of relative light yields for $1 \times$ Tyvek and the simulation with a diffuse reflection and $R_{cover} = 93\%$. As mentioned in section 7.1 channel 1 of the measurement with a trigger in the middle position shows a light yield which is roughly a factor 2 too low, hence the large discrepancy for values containing this measurement.	XX
16	List of relative light yields for $4 \times$ Tyvek and the simulation with a diffuse reflection and $R_{cover} = 99\%$	XX
17	List of relative light yields for $4 \times$ Teflon and the simulation with a diffuse reflection and $R_{cover} = 97\%$	XX
18	List of relative light yields for TiO_2 paint and the simulation with a diffuse reflection and $R_{cover} = 91\%$	XXI

19	List of relative light yields for Aluminium and $1 \times$ Tyvek compared with the corresponding simulations. The value 0.96 for channel 1 in the measurement with a trigger in the mid is again a factor of 0.5 away from the other data points, because of the low light yield for this configuration in the single Tyvek measurement.	XXI
20	List of relative light yields for Aluminium and $4 \times$ Tyvek compared with the corresponding simulations.	XXII
21	List of relative light yields for Aluminium and $4 \times$ Teflon compared with the corresponding simulations.	XXII
22	List of relative light yields for Aluminium and TiO_2 compared with the corresponding simulations.	XXII

- [Abramowitz and Davidson, 2006] Abramowitz, M. and Davidson, M. W. (2006). Photomultiplier Tubes, <http://learn.hamamatsu.com/articles/photomultipliers.html>, 17.06.2013.
- [Adomeit, 2010] Adomeit, S. (2010). *Konstruktion , Bau und Einsatz eines Szintillator-Trigger-Hodoskops*. Diploma thesis, LMU Munich.
- [Biebel, 2009] Biebel, O. (2009). Prinzipien von Szintillations Detektoren, <http://homepages.physik.uni-muenchen.de/~Otmar.Biebel/detektor/detektor06.pdf>.
- [Biebel et al., 2003] Biebel, O., Binder, M., Boutemeur, M., Brandt, A., Dubbert, J., and Duckeck, G. (2003). A Cosmic Ray Measurement Facility for ATLAS Muon Chambers.
- [Buzhan et al., 2001] Buzhan, P., Dolgoshein, B., Ilyin, A., Kantserov, V., Kaplin, V., Karakash, A., Pleshko, A., Popova, E., Smirnov, S., Filatov, L., Klemin, S., and Kayumov, F. (2001). AN ADVANCED STUDY OF SILICON SiPM.
- [CAEN, 2011a] CAEN (2011a). FADC Data Sheet, <http://www.caen.it/csite/CaenProd.jsp?parent=11&idmod=465>, 08.09.2013.
- [CAEN, 2011b] CAEN (2011b). QDC Data Sheet, <http://www.caen.it/csite/CaenProd.jsp?parent=11&idmod=286>, 08.09.2013.
- [CAEN, 2011c] CAEN (2011c). SiPM KIT SP5600A, <http://www.caen.it/csite/CaenProd.jsp?idmod=719>, 10.09.2013.
- [Cova et al., 2004] Cova, S., Ghioni, M., Lotito, a., Rech, I., and Zappa, F. (2004). Evolution and prospects for single-photon avalanche diodes and quenching circuits. *Journal of Modern Optics*, 51(9-10):1267–1288.
- [DuPont, 2012] DuPont (2012). Tyvek, http://www2.dupont.com/Tyvek/en_US/index.html, 15.08.2013.
- [Gomi et al., 2006] Gomi, S., Taguchi, M., Hano, H., Itoh, S., Kubota, T., Maeda, T., Mazuka, Y., Otono, H., Sano, E., Sudo, Y., Tsubokawa, T., Yamaoka, M., Yamazaki, H., Uozumi, S., Yoshioka, T., Iijima, T., Kawagoe, K., Kim, S. H.,

-
- Matsumura, T., Miyabayashi, K., Murakami, T., Nakadaira, T., Nakaya, T., Shinkawa, T., Takeshita, T., Yokoyama, M., and Yoshimura, K. (2006). Development of Multi-Pixel Photon Counters.
- [Groom et al., 2001] Groom, D. E., Mokhov, N. V., and Striganov, S. I. (2001). Muon Stopping Power and Range Tables 10 MeV - 100 TeV. 76(2):37.
- [Grossmann, 2012] Grossmann, J. (2012). *Charakterisierung von Silizium-Photomultipliern*. Bachelor thesis, LMU Munich.
- [Gundacker et al., 2012] Gundacker, S., Auffray, E., Di Vara, N., Frisch, B., Hillemanns, H., Jarron, P., Meyer, T., Pauwels, K., and Lecoq, P. (2012). SiPM Photodetectors for Highest Time Resolution in PET. Technical report, Cern/PH Lab27 TOF-PET Group, LAL Orsay, France.
- [Hamamatsu Electronics, 2008] Hamamatsu Electronics (2008). MPPC Techinfo, http://www.hamamatsu.com/resources/pdf/ssd/mppc_techinfo_e.pdf, 23.04.2013.
- [Herzberg, 1991] Herzberg, G. (1991). *Molecular Spectra and Molecular Structure*. Krieger Publishing Company, 2 edition.
- [Honsberg and Bowden, 2013] Honsberg, C. and Bowden, S. (2013). Absorption Coefficient, <http://pveducation.org/pvcdrom/pn-junction/absorption-coefficient>, 14.08.2013.
- [Iseg, 2006] Iseg (2006). SHQ 224M, <http://www.iseg-hv.com/en/products/product-details/product/16/>, 10.09.2013.
- [Kohlrausch, 1996] Kohlrausch, F. (1996). *Praktische Physik*. Teubner-Verlag, 24 edition.
- [Landau, 1944] Landau, L. D. (1944). On the energy loss of fast particles by ionization. *Journal of Experimental and Theoretical Physics (USSR)*, 8(201).
- [Leo, 1994] Leo, W. R. (1994). *Techniques for Nuclear and Particle Physics Experiments*. Springer-Verlag, second edition.

- [Lutz, 2007] Lutz, G. (2007). *Semiconductor radiation detectors*, volume 40. Springer-Verlag, Munich, 2nd edition.
- [PDG, 2012] PDG (2012). Particle Data Group, <http://pdg.lbl.gov/>, 18.09.2013.
- [Ramilli et al., 2010] Ramilli, M., Allevi, A., Chmill, V., Bondani, M., Caccia, M., and Andreoni, A. (2010). Photon-number statistics with Silicon photomultipliers. *Journal of the optical Soc*, pages 1–29.
- [Rennefeld, 2010] Rennefeld, J. (2010). *Studien zur Eignung von Silizium Photomultipliern für den Einsatz im erweiterten CMS Detektor am SLHC*. PhD thesis.
- [Ruschke, 2010] Ruschke, A. (2010). *Erzeugung von hochenergetischen Neutronen und Protonenbestrahlungen an ATLAS Driftrohren*. Diploma thesis, LMU Munich.
- [Ruschke, 2014] Ruschke, A. (2014). *Development of a Scintillating Muon Detector with two Dimension Spatial Resolution*. Phd thesis in preperation, LMU Munich, Munich.
- [Saint Gobain, 2005] Saint Gobain (2005). Premium Plastic Scintillators, http://www.detectors.saint-gobain.com/uploadedFiles/SGdetectors/Documents/Product_Data_Sheets/BC400-404-408-412-416-Data-Sheet.pdf, 08.08.2013.
- [Saint Gobain, 2011a] Saint Gobain (2011a). Organic Scintillation Materials, <http://www.detectors.saint-gobain.com/uploadedFiles/SGdetectors/Documents/Brochures/Organics-Brochure.pdf>, 09.07.2013.
- [Saint Gobain, 2011b] Saint Gobain (2011b). Scintillating Optical Fibers and Plastic Scintillating Fibers, <http://www.detectors.saint-gobain.com/uploadedFiles/SGdetectors/Documents/Brochures/Scintillating-Optical-Fibers-Brochure.pdf>.
- [Saint Gobain, 2012] Saint Gobain (2012). Detector Assembly Materials, <http://www.detectors.saint-gobain.com/uploadedFiles/SGdetectors/>

Documents/Product_Data_Sheets/SGC_Detector_Assembly_Materials_Data_Sheet.pdf, 10.09.2013.

[Sigma-Aldrich, 2013] Sigma-Aldrich (2013). Polyvinyltoluene, <http://www.sigmaaldrich.com/catalog/product/fluka/464945?lang=de®ion=DE>, 07.08.2013.

[Tapan et al., 1997] Tapan, I., a.R Duell, Gilmore, R., Llewellyn, T., Nash, S., and Tapper, R. (1997). Avalanche photodiodes as proportional particle detectors. *Nuclear Instruments and Methods in Physics Research Section A: Accelerators, Spectrometers, Detectors and Associated Equipment*, 388(1-2):79–90.

[White, 1988] White, T. O. (1988). Scintillating fibres t.o. white. *Nuclear Instruments and Methods in Physics Research*, 273:820–825.

[Wikipedia, 2013] Wikipedia (2013). Franck Condon Principle, http://en.wikipedia.org/wiki/Frank-Condon_principle, 08.08.2013.

[Ziering, 2010] Ziering, M. (2010). Franck Condon principle, http://chemwiki.ucdavis.edu/Physical_Chemistry/Spectroscopy/Electronic_Spectroscopy/Franck-Condon_Principle, 06.08.2013.

Appendix A Instruction Sheet for the Simulation

Here we describe the usage of the self written simulation for light production and propagation in a trapezoidal shaped scintillator.

Starting the program, one has to pass 18 parameters explained in table 12.

number	name	type	description
1	N_{muon}	int	Number of muons
2	X_{Scin} [cm]	double	x -range of scintillator
3	Y_{Scin} [cm]	double	y -range of scintillator
4	Z_{Scin} [cm]	double	z -range of scintillator
5	$Z_{Scin} - Z_{thin}$ [cm]	double	lowest z -coordinate of the detector for $y = Y_{Scin}$
6	Δz_{groove} [cm]	double	Height of a groove
7	$\Delta y_{groove,0.5}$ [cm]	double	Half diameter of a groove
8	$x_{trigger}$ [cm]	double	Center of upper trigger in x
9	$\Delta x_{trigger,0.5}$ [cm]	double	Half diameter of upper trigger in x
10	$y_{trigger}$ [cm]	double	Center of upper trigger in y
11	$\Delta y_{trigger,0.5}$ [cm]	double	Half diameter of upper trigger in y
12	$z_{trigger}$ [cm]	double	Center of upper trigger in z
13	$\Delta z_{trigger,0.5}$ [cm]	double	Half diameter of upper trigger in z
14	Reflection case	int	Reflection case of cover
15	Absorption mode	int	Photon absorption at detection
16	Detection mode	int	Tube or fiber detection
17	L_{mfp} [cm]	double	Mean Free Path of a photon
18	R_{cover}	double	Reflectivity of cover material

Table 12: A list of all parameters one has to pass to the simulation. The possible cases for parameter 14 to 16 are explained in the text.

The simulation has implemented some basic settings how these parameters are handled, which must be changed in the code to simulate alternative situations:

- We have implemented a few basic geometries like a cuboid, a trapezoid and the possibility to have a double layer of trapezoids as foreseen in the final detector. A fine tuning of these geometries is then done with parameter 2 to 5.

A trapezoid is orientated by the simulation as displayed in figure 70. The x -coordinate runs from 0 to X_{Scin} [cm], while the y -coordinate runs from 0 to Y_{Scin} [cm] with the broad side of the scintillator being at $y = 0$. Parameter 4, Z_{Scin} , refers always to the z -range of one scintillator and, in case of two simulated trapezoids, not to the length of the whole structure. In the case of two trapezoids above each other, the upper scintillator is orientated like in the single trapezoid case just shifted to higher values of z . The lower trapezoid is then orientated such, that the whole double layer structure looks like the "CERN prototype".

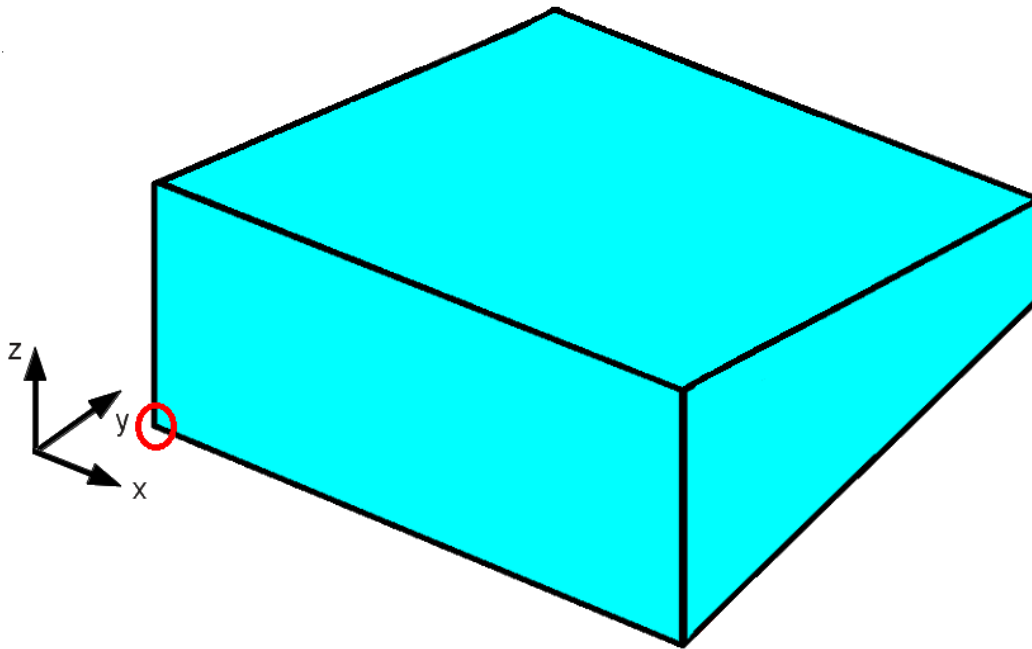


Figure 70: Sketch of the orientation of a trapezoid in a simulation. The origin of the coordinate system is in the corner surrounded by the red circle.

- Also the position and number of grooves or **PMTs** has to be set within the code. Just the height and the width can be adjusted globally for all grooves with parameter 6 and 7.
- The lower trigger plane is currently fixed at $z = 0$ and has an adjustable area by parameter 8 to 11. The upper trigger covers exactly the same area in the $x - y$ plane as the lower one, but has in addition a certain height in z -direction, which is set with parameter 12. Parameter 13 is currently not used by the program at all, but is already implemented to have in future more flexibility for both trigger planes.

If the angle with which a photon hits a wall of the scintillator is smaller than the angle of total reflection, the photon will be reflected by a cover material. With parameter 14 we can set the reflective behavior of this material. In the following list one can see the possible values for this parameter:

0	Directed reflection with a reflectivity of $R = 0.91$
1	Diffuse reflection with a reflectivity of $R = 0.91$
2	Diffuse reflection with a reflectivity of $R = 0.91$ Additionally no total reflection at the tilted wall of the trapezoid.
3	Diffuse reflection with a reflectivity of $R = 0.91$ Additionally no total reflection at all.
4	Same as reflection case 2 Additionally no total reflection at the grooves.
5	Diffuse reflection with a reflectivity of $R = R_{cover}$

To get a trapezoid with grooves, we always cut it out of a cuboid. The cases 2 and 4 are based on the assumption, that cut surfaces are rough and a photon will not be able to perform a total reflection there. The motivation for case 3 comes from the fact, that we use the scintillators from the OPAL experiment, which may have a bad surface.

With Parameter 15 and 16 one can switch between a detection of the photons with fibers or a detection with **PMTs**. Parameter 16 can therefore be zero, which corresponds to a tube detection or one, which simulates a fiber detection. The detection of a photon in the simulation happens by counting it, if it hits a sensitive area. This means for a fiber readout, that all photons hitting a wall of a groove are

counted and analogous a photon must hit a defined area on a wall to be counted in the case of a tube detection. In reality a photon, which is detected by a [WLSF](#) or a [PMT](#) will not be in the scintillator any more. Still the simulation provides a possibility, that photons are counted and still perform a random walk and may be counted once more. Parameter 15 defines the way in which photons are absorbed after they have been counted:

0	No absorption
1	Absorption of the photon, if it hits an area, which is defined to have a tube.
2	Absorption of the photon, if it hits a groove.

The construction of parameter 15 and 16 allows a cross combinations like a fiber detection and a tube absorption of the photons and one has to take care always to select a proper combination. Such a combination would be a tube-detection with a tube absorption.

All values, which are calculated during a simulation, are stored in histograms which themselves are stored in a *root* file. The name of this *root* file contains some of the parameters passed to the simulation in the following order 1-8, 10, 12, 17, 18, 14, 16. An example would be:

Simulation_10000_15_8.8_4.6_3.6_0.2_0.075_10_7_4.6_80_0.99_5_0.root.

In addition to the *root* file, the program also produces three *txt* files. The first one contains information of the simulated parameters. It is used to finally gather parameters varied in a particular run of several simulation in a single file. In a first step each simulation produces its own file and one can after wards combine them to one file. It's name contains the same parameters as the *root* file. A possible name could be

fileNames_10000_15_8.8_4.6_3.6_0.2_0.075_10_7_4.6_80_0.99_5_0.txt.

This file contains a line of text with important information of this single simulation:

parameter 10	$(y_{trigger} [cm])$
parameter 5	$(Z_{Scin} - \Delta z_{thin} [cm])$
parameter 14	(reflection case)
parameter 18	(R_{cover})
name of the <i>root</i> file	

The second file contains a line of numbers listing how much photons each readout channel has counted during the simulation. Its name is also filled with the parameters from the *root* file:

```
logfileTubeAngleSelected_10000_15_8.8_4.6_3.6_0.2_0.075_10_7_4.6_80_0.99_5_0.txt,
```

with the phrase *TubeAngleSelected* refers to the detection mode. The first entry this file is parameter 10, the middle of the trigger in *y*-direction followed by the number of photons produced in total and the numbers of collected photons in each readout channel.

When the simulation is finished, the file produce the last *txt* file, containing just the information, that the simulation is finished. This is useful if one processes a lot of simulations in parallel at the LRZ as described below. If such a file can be found in the folder, one knows that the simulation is finished. A name of this file is for example

```
THIS_RUN_IS_READY_10000_15_8.8_4.6_3.6_0.2_0.075_10_7_4.6_80_0.99_5_0.txt,
```

again with the parameters explained above.

As already mentioned one often wants to process a few simulations in parallel, which can be done using the LRZ. In the following we want to describe the basic steps for such a procedure at an example with two simulations where we change the length of the scintillator in *x* direction. At first one has to log in at the LRZ with the own LRZ-ID. This is well described at https://wiki.physik.uni-muenchen.de/etp/index.php/Howto_login. Once this is done, we have to copy the simulation program to the LRZ. This can be done for example in the origin folder of the simulation by the bash command:

```
scp *.cpp *.h Makefile ri32bow@klogin3.lrz.de
```

In order to compile the program on the LRZ, we have to first load a *root* version. The following command will do the job:

```
source /home/grid/lcg/sw/root_setup_sles11.sh-v5.34
```

We can than write a first script to start a simulation. We label this script *runSimulation.sh* and write in there the two following lines:

```
source /home/grid/lcg/sw/root_setup_sles11.sh-v5.34
./Simulation $@
```

We then write a second script, which calls the first one as often as we have different simulations to perform. In our case with the 2 simulations we write a script called *performSimulations* as follows:

```
qsub ./runSimulation.sh 10000 15.0 8.8 4.6 3.6 0.2 0.075 10.0 5.0 7.0 1.0 4.6 0 5  
1 0 80 0.99
```

```
qsub ./runSimulation.sh 10000 30.0 8.8 4.6 3.6 0.2 0.075 10.0 5.0 7.0 1.0 4.6 0 5  
1 0 80 0.99
```

where we simulate a 15 cm long and a 30 cm long trapezoid.

After making this script executable we can run the simulations with *./performSimulations*. After each simulation is ready, we find the corresponding *THIS_RUN_IS_READY* in the folder.

Each simulation will get an ID and we find file in the folder containing this ID. One of them may be of interest since it contains the command line outputs of the simulation. This file is called *runSimulation.sh.o** where the * stands for the job ID.

One can also display all of the simulations, which are currently running by typing:

```
qstat
```

In the now displayed table one sees for example the state of each job. If there stands a *r*, the job is still in progress. If a job is finished, it will vanish from this list.

The last of the important commands on the LRZ is *qdel*. With this we can remove jobs. One can either remove a particular job by inserting

```
qdel *
```

where * is again the job ID. If one wants to remove all jobs at once, one has to type:

```
qdel -u 'ri32bow'
```

Appendix B Comparison of Measurement and Simulation

In this chapter we give an overview of all values, which are used to compare the simulation with the measurement, as described in section 7.2.1. Table 13 lists the parameters of the simulations fitting best to the corresponding measurements.

Aluminium	directed reflection	$R_{cover} = 91\%$
1 × Tyvek	diffuse reflection	$R_{cover} = 93\%$
4 × Tyvek	diffuse reflection	$R_{cover} = 99\%$
4 × Teflon	diffuse reflection	$R_{cover} = 97\%$
TiO_2	diffuse reflection	$R_{cover} = 91\%$

Table 13: Parameters for the cover material in simulation, which provide the best agreement with the data.

The following tables 14 - 18 list the relative light outputs of the four different readout channels for all covers and the corresponding simulations.

	$\frac{Ch0}{Ch1}$	$\frac{Ch0}{Ch2}$	$\frac{Ch0}{Ch3}$	$\frac{Ch1}{Ch2}$	$\frac{Ch1}{Ch3}$	$\frac{Ch2}{Ch3}$
Measurement trigger left	1.026	1.232	1.110	1.201	1.082	0.901
Simulation trigger left	1.114	1.584	1.692	1.422	1.519	1.068
Measurement trigger mid	0.986	0.796	0.777	0.807	0.787	0.975
Simulation trigger mid	1.054	0.842	0.930	0.798	0.882	1.104
Measurement trigger right	0.850	0.543	0.513	0.628	0.603	0.960
Simulation trigger right	1.039	0.353	0.428	0.339	0.412	1.215

Table 14: List of relative light yields for Aluminium and the simulation with a directed reflection and $R_{cover} = 91\%$.

	$\frac{Ch0}{Ch1}$	$\frac{Ch0}{Ch2}$	$\frac{Ch0}{Ch3}$	$\frac{Ch1}{Ch2}$	$\frac{Ch1}{Ch3}$	$\frac{Ch2}{Ch3}$
Measurement trigger left	1.048	1.075	1.021	1.026	0.974	0.950
Simulation trigger left	0.951	1.175	1.133	1.236	1.191	0.964
Measurement trigger mid	1.766	0.864	0.845	0.489	0.478	0.977
Simulation trigger mid	0.935	0.903	0.892	0.965	0.953	0.988
Measurement trigger right	1.022	0.722	0.706	0.706	0.690	0.978
Simulation trigger right	0.932	0.579	0.619	0.621	0.664	1.069

Table 15: List of relative light yields for $1 \times$ Tyvek and the simulation with a diffuse reflection and $R_{cover} = 93\%$. As mentioned in section 7.1 channel 1 of the measurement with a trigger in the middle position shows a light yield which is roughly a factor 2 too low, hence the large discrepancy for values containing this measurement.

	$\frac{Ch0}{Ch1}$	$\frac{Ch0}{Ch2}$	$\frac{Ch0}{Ch3}$	$\frac{Ch1}{Ch2}$	$\frac{Ch1}{Ch3}$	$\frac{Ch2}{Ch3}$
Measurement trigger left	1.083	1.072	1.039	0.989	0.959	0.970
Simulation trigger left	0.941	1.149	1.100	1.221	1.170	0.958
Measurement trigger mid	1.106	0.842	0.860	0.761	0.777	1.022
Simulation trigger mid	0.929	0.915	0.893	0.985	0.962	0.976
Measurement trigger right	1.104	0.725	0.725	0.657	0.657	1.000
Simulation trigger right	0.926	0.626	0.653	0.676	0.705	1.043

Table 16: List of relative light yields for $4 \times$ Tyvek and the simulation with a diffuse reflection and $R_{cover} = 99\%$.

	$\frac{Ch0}{Ch1}$	$\frac{Ch0}{Ch2}$	$\frac{Ch0}{Ch3}$	$\frac{Ch1}{Ch2}$	$\frac{Ch1}{Ch3}$	$\frac{Ch2}{Ch3}$
Measurement trigger left	1.107	1.068	1.099	0.965	0.993	1.028
Simulation trigger left	0.946	1.160	1.114	1.226	1.178	0.961
Measurement trigger mid	1.074	0.923	0.936	0.859	0.871	1.014
Simulation trigger mid	0.931	0.911	0.893	0.978	0.958	0.980
Measurement trigger right	1.070	0.788	0.811	0.736	0.758	1.030
Simulation trigger right	0.929	0.602	0.638	0.649	0.687	1.059

Table 17: List of relative light yields for $4 \times$ Teflon and the simulation with a diffuse reflection and $R_{cover} = 97\%$.

Appendix B: Comparison of Measurement and Simulation

Measurement trigger left	1.133	1.194	1.144	1.054	1.009	0.958
Simulation trigger left	0.953	1.186	1.146	1.244	1.202	0.966
Measurement trigger mid	1.079	1.113	1.057	1.032	0.980	0.950
Simulation trigger mid	0.938	0.901	0.890	0.960	0.949	0.988
Measurement trigger right	1.050	1.071	0.977	1.019	0.930	0.912
Simulation trigger right	0.935	0.570	0.614	0.610	0.656	1.076

Table 18: List of relative light yields for TiO_2 paint and the simulation with a diffuse reflection and $R_{cover} = 91\%$.

Tables 19 - 22 show the relative light yields for different reflective covers per channel. We use always the Aluminium cover as a reference because this is used in the first prototype detector.

	<i>Ch0</i>	<i>Ch1</i>	<i>Ch2</i>	<i>Ch3</i>
Measurement trigger left	0.64	0.64	0.55	0.58
Simulation trigger left	0.70	0.70	0.60	0.55
Measurement trigger mid	0.54	0.96	0.58	0.58
Simulation trigger mid	0.54	0.54	0.66	0.59
Measurement trigger right	0.45	0.54	0.60	0.62
Simulation trigger right	0.42	0.42	0.76	0.67

Table 19: List of relative light yields for Aluminium and $1 \times$ Tyvek compared with the corresponding simulations. The value 0.96 for channel 1 in the measurement with a trigger in the mid is again a factor of 0.5 away from the other data points, because of the low light yield for this configuration in the single Tyvek measurement.

	<i>Ch 0</i>	<i>Ch 1</i>	<i>Ch 2</i>	<i>Ch 3</i>
Measurement trigger left	0.50	0.52	0.45	0.46
Simulation trigger left	0.68	0.60	0.49	0.46
Measurement trigger mid	0.43	0.48	0.45	0.48
Simulation trigger mid	0.51	0.45	0.55	0.49
Measurement trigger right	0.36	0.48	0.50	0.52
Simulation trigger right	0.35	0.31	0.62	0.53

Table 20: List of relative light yields for Aluminium and $4 \times$ Tyvek compared with the corresponding simulations.

	<i>Ch 0</i>	<i>Ch 1</i>	<i>Ch 2</i>	<i>Ch 3</i>
Measurement trigger left	0.54	0.58	0.46	0.53
Simulation trigger left	0.70	0.60	0.51	0.46
Measurement trigger mid	0.47	0.51	0.55	0.57
Simulation trigger mid	0.52	0.46	0.56	0.50
Measurement trigger right	0.42	0.52	0.61	0.66
Simulation trigger right	0.39	0.35	0.68	0.59

Table 21: List of relative light yields for Aluminium and $4 \times$ Teflon compared with the corresponding simulations.

	<i>Ch 0</i>	<i>Ch 1</i>	<i>Ch 2</i>	<i>Ch 3</i>
Measurement trigger left	0.81	0.89	0.78	0.83
Simulation trigger left	0.83	0.71	0.62	0.56
Measurement trigger mid	0.70	0.76	0.97	0.95
Simulation trigger mid	0.63	0.56	0.67	0.60
Measurement trigger right	0.61	0.75	1.22	1.16
Simulation trigger right	0.50	0.44	0.80	0.71

Table 22: List of relative light yields for Aluminium and TiO_2 compared with the corresponding simulations.

Acknowledgement

At this point, I would like to give thanks to all those who supported me during my work on this thesis.

I would like to thank Prof. Dr. Otmar Biebel for giving me the opportunity to write this thesis. His advices were always helpful and profound, and his door was always open for questions.

My thanks go also to Dr. Ralf Hertenberger for continuously pushing my research in a fruitful direction and for tons of sweets during the beam time.

This thesis contributes to the PhD thesis of Alexander Ruschke, whom I want to thank a lot for his advices on the readout electronics, for lots of discussion concerning the improvement of the detector and finally for the hours he spent reading my thesis.

Thanks to my girlfriend Annabel Säurig enduring myself, even when I was stressed a lot.

I have to thank my entire family for making the study at the LMU possible. Thanks also to my grand father and my cousin, who were not able to witness the ending of this thesis. God bless them!

Thanks a lot to all my friends supporting this thesis in any way, especially to Alexander Arth teaching me C++ with great patience and reading this thesis together with Marco Häuser. Also I have to thank Friedrich Hönig telling me how to run simulations on the LRZ at the last minute.

Declaration of academic integrity

I hereby declare, that this thesis is my own work and that I have not used any sources and aids other than those stated in the thesis.

Munich, September 27, 2013

Ralph Müller